University College London

Thesis

Doctor of Philosophy in Electronic Engineering

Microwave Oscillator Ultrasound Receivers

Author:
Tom Robbins

Supervisor:
Professor Cyril Renaud

September 25, 2020

I hereby declare that, except where specifically indicated, the work submitted herein is my own original work.
Tom Robbins, 04/03/2020

Technical Abstract

Title: Microwave Oscillator Ultrasound Receivers
Author: Tom Robbins

Ultrasound refers simply to those sound waves which are above the range of human hearing. Since the discovery of the piezoelectric effect in the late 19th Century, the generation and reception of ultrasound has become an integral (though understated) part of modern life in fields as diverse as cardiac imaging and automotive range-finding. For the vast majority of applications, high-frequency ultrasound is generated and received by means of some piezoelectric material, most often derived from lead zirconate titanate (PZT), a technology which has changed little since the 1970s. In recent decades, there has been a push to overcome some limitations posed by PZT and related technologies. Two prominent technologies which have emerged as alternatives are micro-electromechanical systems (MEMS) such as capacivie micromachined ultrasound transducers (CMUT), and optical Fabry-Perot hydrophones.

We examined the possibility of creating a purely electronic analogue of the optical Fabry-Perot hydrophone. The device we invented is called a *microwave oscillator ultrasound receiver* (MOUR). It is implemented by a compact electromagnetic resonator on a piece of high-permittivity circuit board covered by a thin superstrate layer. When the superstrate layer deforms (as a result of incoming ultrasound), the transfer function of the resonator shifts, and that shift can be detected by reading out the IQ modulation of a carrier transmitted through the resonator at or near its resonant frequency. To multiplex the device, an array of resonators, each with a different resonant frequency, can be produced. Each element is thereby associated with its own microwave

channel, since each element will modulate only the carrier near its electromagnetic resonance. In this way, frequency division multiplexing (FDM) is implemented, allowing fast readout of each element by tuning the receiver circuitry to the relevant microwave frequency. This has the potential to greatly simplify the design of ultrasound receiver arrays, as a single electrical pathway can be used to read out multiple elements, without the need for digitisation or analogue switching.

We designed, manufactured and tested a proof-of-concept device comprising a single electromagnetic resonator implemented as a defected microstrip structure (DMS) in the shape of a hairpin on a piece of high-permittivity circuit board. The board was covered with a layer of black latex paint to form a low-Young's modulus superstrate layer and characterised with a conventional ultrasound source. We present these results, along with a detailed description of the device's operating principle, its applications, and design considerations.

Impact Statement

The work carried out has led to numerous examples of impact, in both academia and industry. The main content of the thesis revolves around Microwave Oscillator Ultrasound Receivers (MOUR), an concept invented by the author. This has lead to a talk at the IEEE International Ultrasound Symposium 2018[1], and a patent application (title: 'Microwave Oscillator Ultrasound Receivers', application number 16/656,998). The patent has been assigned to a new UK-registered spin-out company, Pinfold Technologies Ltd (company number 12017058), which is in the process of commercialising the invention, and of which the author is Managing Director. The author participated in the Conception X programme, which culminated in a presentation to a variety of investors and corporate representitives, and a £5000 award.

As a result of the invention, the author won a Cohen Award from the Worshipful Company of Scientific Instrument Makers, and was shortlisted for the 2019 IET Young Innovator Award.

It is hoped that the published work, combined with the patent, will lead to the development of a new technique for building ultrasound imaging devices. This new technique could potentially lower the cost of ultrasound probes, increasing their availability at more levels of medicine and in the developing world.

The thesis also contains some preliminary unpublished work which could be incorporated into future research programmes. This includes a set of symmetric equations for transmit and receive ultrasound beamforming, a derivation of the characteristics of lossy acoustic cavities, and work on designing ultrasound receiver systems which

[1] T. S. Robbins et al. "Microwave Oscillator Ultrasound Receivers". In: *2018 IEEE International Ultrasonics Symposium (IUS)*. 2018 IEEE International Ultrasonics Symposium (IUS). Oct. 2018, pp. 1–4. doi: 10.1109/ULTSYM.2018.8580205.

combine transducers featuring low electroacoustic Q with modern digital signal processing techniques.

Acknowledgements

I would like to first and foremost thank Professor Cyril Renaud for taking me on when I was a failing PhD student with nothing but a vague idea that ran orthogonal to my original PhD proposal. He helped me obtain some lab space, bits of equipment and set the initial direction of the project by suggesting I try making the device on readily available circuit board material, rather than working on top of a more complicated terahertz platform as I initially suggested.

My colleague James Seddon, without whom I would never have had the idea for MOURs (and would have probably ended up dropping out), also deserves a special mention. His work on lab-on-chip terahertz sensors was the starting point of my investigations, and he has on innumerable occasions stepped in to help with setting up experiments and simulations, taught me how to use equipment, given sage advice and, through his creativity and willingness to tinker with something until it works, set an example for me. I am lucky to have worked with someone who is as talented as he is generous with his time.

Erwin Alles similarly offered ample guidance, both before and after starting the MOUR project, and his comments and help around the finicky details of ultrasound, time spent in the lab, and thoughtful insights were indispensable to me. Others in the medical physics department, including Paul Beard, James Guggenheim, Richard Colchester, Edward Zhang, Efthymios Maneas, and Sacha Noimark, were always on had to help with a question or hunt down a piece of equipment.

Paul Reynolds from Siemens gave me much encouragement to pursue my ideas, and helped me understand where MOURs could offer comparative advantage to existing technologies.

The creative and skilled members of the departmental workshop, in particular John Langdon and Tom Hamer, were able to turn my handwaving and rambling descriptions of device holders I needed made into workable CAD designs and functional objects, as well as carry out the inevitable adjustments when I realised I hadn't got my specifications quite right in the first place. I am also indebted to Martin Scott, who fabricated the boards and taught me how to source raw materials for free as samples from suppliers.

Although I will probably never meet her in person, I would like to thank Alexandra Elbakyan, who, at great personal sacrifice, created Sci Hub. Sci Hub was an indispensable tool in my research: it was thanks to it that I was able to dig up some old but important references which would have otherwise been behind a pay wall.

Special thanks go to my family: my parents Danny and Philippa, my sister Charlotte, and my brothers Hugo and Cameron. Each have in their own way supported me throughout my PhD and been selflessly invested in my success. In particular, my parents, whose love and support has been unwavering since the day I was born, continue to set an example for me and show me how much I still have to learn.

Lastly, I would like to thank my partner Alex, whose kindness and good nature is more than I ever thought I'd be able to find in a person. To her, I dedicate my thesis.

Contents

List of Figures

Chapter 1

Introduction

This work is concerned with the problem of mapping sound waves defined over a region of space into electronic signals whilst preserving, as much as possible, the dimensionality of the original sound distribution. Viewed in this way, the history of ultrasound is one of trade-offs reflected in the choices of projection for the various dimensions of the original sound distribution. We note that, unlike the history of photography, where phase information is considered lost by default, phase recovery of sound waves has always been possible, if not trivial. Another way of stating this is that nature has provided us with square-law detectors for light and linear detectors for sound [1]. In fact, if the reader is not inside an anechoic chamber, he is taking advantage of linear acoustic measurement information right now, since to determine the direction of incoming sound waves, our brains measure the phase difference between sounds received by the left and right ears [2].

Continuing with this theme, although human eyes do not capture phase information from light[1], we can recognise the source of light much more accurately than sound (provided we're looking in the right direction), and even distinguish multiple light sources with very small angular separations [4]. And despite this loss of phase information, we can even approximate depth by exploiting the parallax between each

[1] From an evolutionary perspective, it wouldn't have made much difference if we could, somehow, coherently detect light, since the coherence length of sunlight is about 600 nm [3]

eye.

Mathematically, we may summarise these differences with the assertion that human vision is good at capturing the direction and magnitude of k-vectors but totally discards the complex phase information, whereas human hearing preserves complex phase and magnitude but (largely) discards the direction of the vector. Ie, for a wavefunction ϕ defined over an aperture, its representation after capture, Φ, is given by

$$\begin{aligned} \Phi &= \phi\phi* && \text{for light,} \\ \Phi &= \int_{\text{aperture}} \phi(\mathbf{r}) \cdot \mathrm{d}\mathbf{r} && \text{for sound.} \end{aligned} \tag{1.1}$$

For this reason, most people experience the world in a way that is intensely visual.[2] Conversely, bats use echolocation (also known as sonar) to determine their surroundings and locate prey. Bats (which mainly eat insects and other small animals) are under evolutionary pressure to be able to detect small objects at long distances. In practice, physics works against them: higher frequencies of sound, which would be capable of resolving smaller objects in the far-field, suffer greater attenuation through air, and bats cannot detect small objects at distance as well as human vision can [6]. Where light is abundant and not scattered or absorbed by the medium, sonar is a poor substitute.

There are, however, many situations where visible light is so highly scattered or absorbed that optical imaging is impossible. For instance, car parking sensors which use ultrasound can detect nearby obstructions even in darkness or fog [7]. And, significantly, it was known even to Leonardo da Vinci that certain sounds can travel far

[2] In his famous treatise *The Theory of Sound* [5], Lord Rayleigh considers how trained musicians are able to distinguish two or more notes played simultaneously. He dismisses the possibility that the human ear has areas sensitive to different tones, in analogy to the way we perceive colour, and instead argues that humans are somehow able to analyse sounds in terms of their Fourier components.

greater distances through water than they can through air,[3] and his suggestion that this principle be used to detect ships by means of long underwater listening tubes was taken up four hundred years later during World War I, forming the basis for early military sonar [8]. The role it played in submarine warfare of World War I would be soon echoed by the role of radar for aerial warfare during World War II, and the two trades share a great deal of common jargon, such as 'phased array', 'synthetic aperture' and 'frequency chirps'. Their histories are further entwined through the development of crystal oscillators and ultrasonic delay lines, vital to advanced radar systems [9].

After WWI, there emerged two somewhat separate disciplines involving ultrasound: ultrasound imaging and sonar [10]. Sonar grew out of ultrasound inspection, where either a single ultrasound transducer in echo mode or two transducers in transmission mode allowed abrupt changes in some acoustic medium to be detected by means of an oscilloscope. The straight-line distance between the face of the transducer and the acoustic discontinuity could be inferred by the x-position of the pulse on the oscilloscope trace. Today this is referred to as 'A-Mode' (Amplitude-Mode) ultrasound, and is still used in non-destructive testing (NDT) and certain medical contexts [11].

In the 1930s, the term ultrasound imaging was used in a more literal sense than it is today. Early techniques worked in direct analogy to photography and television. A variety of thermal, photographic and chemical techniques were used to form X-ray-style images on thermal, photo or pressure-sensitive paper [14]. The invention of the Sokolov tube in 1949 offered a different approach. Inspired by television, it comprises a vacuum tube coated on one end with a piezoelectric ma-

[3] For media with low shear viscosity, the thermal conductivity of the medium becomes the dominant attenuation mechanism, and the local thermal conductivity has an f^2 dependence on the ultrasound frequency f.

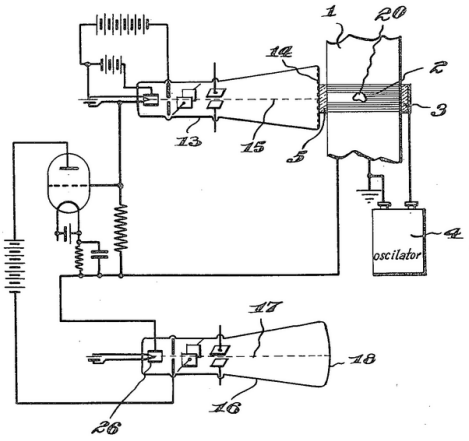

(a) Schematic of a Sokolov tube taken from the original patent application [12].

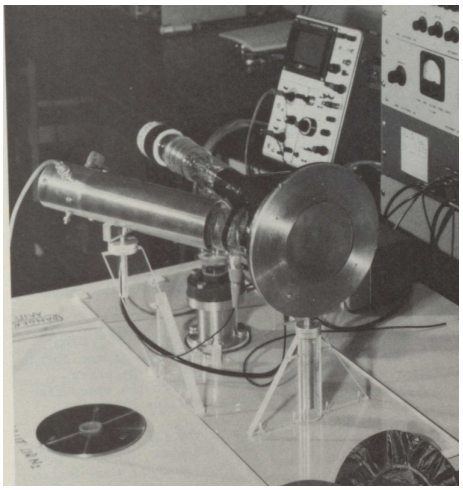

(b) Photo of an assembled Sokolov tube, reproduced from [13]

Figure 1.1: Sokolov tube

terial, forming the anode. When ultrasound impinges on the anode, the instantaneous pressure can be recorded at that point by a scanning electron beam. The velocity of the secondary electrons emitted at each point on the piezoelectric plate is a function of the local electric potential, which is in turn a function of the local pressure. The secondary electron current can then be measured by the current through a biased collection plate [15, 16].

The imaging techniques described suffer the drawback that they record only the amplitude, not the phase, of the impinging ultrasound field. With the exception of Sokolov tube, the image contrast follows a square-law, corresponding to the first expression in (1.1). In the 1960s, attention turned to ultrasound holography, which in this context means preserving phase information in images which are formed by square-law-sensitive processes. The rich body of work which emerged on this theme [17] owed itself to the availability of highly coherent acoustic sources, at a time when laser science was in its infancy and coherent light sources were still scarce.

Meanwhile, advances in sonar were mirroring those in radar.

Again, it should be emphasised that this approach was seen as quite distinct from imaging [18]. Image formation using pulse-echo A-Mode acquisition, when it was done at all, involved mechanical translation of the transducer. It was known that arrays of ultrasound transducers could be configured to direct an ultrasound pulse or continuous wave (CW) in various directions by setting phase delays to each element. However, limitations in transducer miniaturisation at the time meant that MHz ultrasound wavefronts produced in this way typically suffered from grating lobes, degrading the signal-to-noise ratio (SNR) of the reflected signals [19]. For this reason, phased ultrasound arrays were best suited for detecting and ranging discrete objects with good angular separation [20], rather than forming the type of detailed images we now associate with B-Mode (Brightness-Mode) ultrasound.

Nonetheless, some attempts at B-Mode ultrasound imaging were made in the early 1950s [21]. Though still requiring mechanical translation of a single transducer, the main innovation here was the modulation of the brightness, rather than y-deflection, of the oscilloscope trace, and as such these experiments are considered to be the birth of 2D cross-sectional ultrasound imaging [11]. As techniques for miniaturisation became known, phased arrays of ultrasound transducers became capable of forming images without need for mechanical translation [22, 23]. Here the analogy with sonar and radar breaks down: military radar typically uses wavelengths of the order of centimetres, making far-field 'imaging' in a terrestrial sense impossible. Ultrasound, despite operating at similar frequencies, exhibits much shorter wavelengths,[4] making diffraction-limited imaging possible at length-scales familiar to us from conventional photography and even microscopy [24]. At some stage, it was noticed that phased-array ultrasound and ultrasound holography were essentially analogous, differing only in

[4]The implications of this are discussed in detail in §3.1

whether beamforming is carried out before or after transmission [25]. Shortly after, arrays of discrete piezotransducers began to displace all other ultrasound imaging methods (of which there had been a rich variety [14]) for almost all practical purposes. The reasons for this are the high SNR of the transducers, their versatility as shown by the wide variety of pulse-echo configurations possible [26], and the compactness afforded by not needing separate ultrasound transmitters and receivers (known as duplexing).

This roughly describes the state of ultrasound imaging today. As previously mentioned, it was noticed early on that ultrasound could travel relatively unimpeded through media which exhibit high absorption or scattering of light [9]. This made it ideal for biomedical imaging, and the safety of low ultrasound doses is now firmly established [27]. Virtually all commercial ultrasound imaging systems used in a clinical context use piezo-transducer arrays differing little from those described in the preceding paragraph. Most advances in clinical ultrasound have resulted from innovations in manufacture, allowing new, highly compact form-factors for intravascular imaging and constrained environments [28], and Moore's Law-conferred advances in digital signal processing (DSP) [11, 29].

* * *

Despite the wide variety of ideas which were explored in the 1960s, commercial ultrasound imaging systems, with few exceptions, rely on a 1D array of piezotransducers, usually made from a ferrous piezoceramic such as lead zirconate titanate (PZT) (single crystals are used for high-end systems [30]), and some sort of imaging procedure which involves beamforming, either in transmission, reception or both. Considerable effort and ingenuity has been deployed to increase element count, reduce element size and power requirements, and improve SNR, all whilst keeping costs low. These iterations have mostly taken place

within the leading large multinational medical imaging companies: Philips, Siemens, GE, etc. Nonetheless, there are two potentially disruptive developments which have grown out of university labs which are now seeing clinical application: capacitive or piezoelectric micromachined ultrasound transducers (CMUT/PMUT), and optical ultrasound. We will review each of these briefly, before introducing a third solution which forms the subject of the thesis, and was first presented by the author in 2018 [31]. However, before going into specifics, it will be useful to survey some historical background which will help put each of these developments in their proper context.

In its most general sense, a *transducer* is simply a device which converts one form of energy into another. Since for this work we are interested in only electroacoustic transducers, we will take 'transducer' to be synonymous. This definition has a wider scope than we might initially expect. For example, a car door slamming is a transducer, as is a solution which undergoes a chemical reaction upon ultrasound insonation (the conversion is between acoustic and chemical energy). We can exclude these spurious examples by specifying that a useful transducer should convert (mostly) linearly between sound and either electromagnetic or electrical energy. The first such devices emerged in the latter half of the nineteenth century and formed the basis of the telephone (confusingly, the terminology for transmitters and receivers is in the reverse sense for early telephony than it is for sonar—the part of the telephone that converts sound waves into electrical energy is the transmitter, and the part which converts back into sound is the receiver). The first ever radio broadcasts of intelligible speech were made in a series of experiments between 1901 and 1906, proving that radio waves could too be made to carry sound.

In the years 1870 - 1890, the so-called "golden age of transduction" [32], virtually every type of electroacoustic transducer taken

for granted today was invented. At that time, there was only one application—telephony of human speech—against which these inventions were measured. Over time, the dominant transducer type for telephony changed according to refinements in transducer design and the wider technological landscape. But, as we will see shortly, some transducers which were made obsolete for telephony due to the superior performance of inductive, linear-motion-based transducers, later found use in other applications, such as for sonar, phonograph recording, or silicon microphones for mobile phones [33]. A systematic theoretical framework for dealing with such a wide range of transduction techniques and understanding what makes them work better for some applications than others was worked on from the early 1900s, but only rigorously completed in the 1950s. We will outline the important aspects of this theory later on.

One such transducer to emerge from the "golden age" is the piezoelectric transducer (whose invention actually predates by a couple of years the formal discovery of the piezoelectric effect by the Curie brothers [32]). Piezoelectric transducers feature a piece of material which exhibits a strong piezoelectric effect sandwiched between two conducting parallel plates. Modern transducers feature matching layers, acoustic lenses, and electrical impedance matching circuits to improve their efficiency and sensitivity. They can both send and receive ultrasound, and as such are most commonly used in a duplexed pulse-echo configuration. Early transducers used single quartz crystals or Rochelle salt, but the discovery of ferroelectric ceramics which could be polled to induce a strong piezoelectric susceptibility in the 1950s paved the way for cheap, mass-produced transducers. Later developments saw the discovery of yet another class of piezoelectric material, the piezoelectric polymer, which, when processed correctly, could be induced into a phase which exhibits an extremely high piezoelectric

susceptibility [34]. However, the best known piezoelectric polymers, such as polyvinylidene fluoride (PVDF), have a lower electrostatic permittivity and piezoelectric coupling coefficient than PZT, limiting their usefulness in duplexed sandwich transducers: low permittivity means that very large voltages are required to generate strong pulses, and conventional voltage amplifiers and transmission lines are difficult to impedance match. For these reasons, duplexed ultrasound transducer arrays are most commonly constructed using a diced PZT sandwich configuration.

When VLSI (Very Large Scale Integration), CMOS (Complimentary Metal Oxide and Semiconductor) and lithography began to revolutionise the manufacture of electronics from the 1970s onwards, the piezoelectric ultrasound transducer was left relatively untouched [35]. A device which could deliver duplexed ultrasound transducer arrays whilst benefiting from the cost reduction and yield increase afforded by these techniques was sought [36]; the result was CMUT [37]. CMUT is a micromachined capacitor with an air or vacuum gap instead of a dedicated dielectric separating the two plates [38]. It can trace its origins to the condenser (capacitor) microphone, one of the earliest types of microphone, which exploits the variation of the capacitance of two parallel plates (or some similar configuration) as the distance between those plates changes. Efficient electroacoustic conversion for this category of transducer depends on the electric field strength between the two plates, so CMUT elements generally comprise a plurality of micrometre-scale cavities connected in series. This requirement introduces several manufacturing challenges: each CMUT membrane must be suspended above a vacuum-sealed cavity to reduce damping, and typically tens or hundreds of such cavities are required to form a single element. Modern piezoceramic ultrasound systems rely on $\sim 10^2 - 10^3$ elements to form high resolution images

with wide fields of view, so developing micro-electromechanical system (MEMS) manufacture processes with sufficiently high yields to make this approach economically viable remains challenging. Under these circumstances, widespread adoption of CMUT rests on the untested claim that the high wafer cost can be offset by selling ultrasound as a mass-market medical device (as opposed to a specialist medical device, with a variety of transducer array designs depending on application). PMUTs, on the other hand, can be made by growing a single crystal of a piezoelectric material—for instance, aluminium nitride—on top of silicon, and etching microcavities behind the crystal layer to enhance sensitivity [39]. Efforts to commercialise CMUTs and PMUTs are ongoing and intensifying [38].

Another fairly recent development has been that of the ultrasonic camera [40]. Alongside recent academic work [41, 42], various designs for ultrasound imaging devices which are more in the tradition of digital photography than sonar have appeared and been commercialised [43–46]. These involve a 2D array of piezo elements bonded to CMOS multiplexing and addressing circuitry as a receiver sensor (similar in construction to an infra-red camera sensor [43]), and a separate transmitting source. In this way, the need for duplexed transceivers is avoided, considerably simplifying the circuitry. The receiver and source must be arranged such that there is a low-loss acoustic path between each and the sample [44]. These devices offer C-Mode ultrasound imaging at a fairly low cost. They have been deployed in the field non-destructive testing, and, more recently, as ultrasonic fingerprint sensors found in some smartphones [47, 48], where the cost is further lowered by using a directly deposited piezo-poylmer such as PVDF as the pressure-sensitive layer. This approach has limited use for more general imaging, since, due to the instantaneous charges produced by the compression of the PVDF film being too small to de-

tect directly, it relies on measuring the charge accumulation between sample and hold cycles [49, 50]—in other words, the readout voltage of each element is the time-integrated ultrasound signal at that point, resulting in very coarse axial resolution. Nonetheless, it allows materials with a low DC dielectric constant—such as PVDF—to be used, despite their unsuitability for true RF ultrasound imaging in the configurations outlined in [41, 42].

The final component which forms the backdrop for the present work is the wide-ranging field of optical ultrasound. Broadly speaking, this may refer to any of the following three things: the control of light by acoustics (acousto-optic modulation [51]); acoustic metrology using optics [52]; and using high-power lasers to generate ultrasound [53]. Recently, the downward trajectory of laser costs, alongside a push to overcome some of the inherent limitations of PZT-based ultrasound imaging, have led to laser-based ultrasound systems being seen as serious candidates for clinical ultrasound imaging [54, 55]. Some of the advantages over electronic systems include the very high sensitivity of optical detectors [56], their inherent wideband nature [57], MRI compatibility, and the cost advantage over piezoceramic transducers in certain applications where the ultrasound transducer needs to be disposable for *in vivo* applications [54].

However, such devices are extremely difficult to multiplex. One approach is to switch the optical path between the laser source, pressure-sensitive mirror or micro-resonator, and photodiode, so that multiple elements in a receiver array can be addressed in turn. High-quality images have been obtained in this way using a galvo mirror to deflect an interrogation beam across a 2D array of pressure-sensitive optical micro-resonators [55], a technique which is highly reminiscent of the Sokolov tube, only using photons instead of electrons [16]. Such bench-top systems work well in a research environment, but lack the

portability of modern clinical ultrasound probes. They are also expensive to build and maintain, and very sensitive to environmental factors (such as dust, temperature and vibration). Instead of using free-space optics, there have been successful attempts at using optical fibre-based systems which employ multiplexing by a synthetic aperture approach [58–60]. In these examples, an ultrasound point-source is formed by the pulsed optical illumination of a small area of optically-opaque elastomer [57]. Using a fibre bundle, deflection of the laser beam at one end of the bundle corresponds to the movement of the ultrasound point source at the distal end. An image can then be constructed using successive ultrasound point sources and receiving using a single optical fibre with a pressure-sensitive Fabry-Perot cavity [61]. Although the optical fibres for transmitting and receiving the ultrasound could be made fairly cheaply (notwithstanding the cost of coherent fibre bundles), and free-space optical components could be replaced by acousto-optic lenses (AOLs), the system still requires two expensive lasers (in particular a high-power pulsed laser [60]), is non-portable, and would occupy significant real-estate in already crowded operating theatres [62].

There are some applications which only require a single ultrasound imaging element, and therefore do not require any multiplexing. For instance, a single side-viewing ultrasound element can be used to detect plaques on arterial walls. To this end, video-rate images have been obtained using an all-optical mechanically rotating system, delivering improvements over comparable piezo-based systems owing to the high SNR and broadband nature of all-optical ultrasound [63]. It remains to be seen whether or not there is a sufficient per-procedure cost advantage over piezo-based intra-vascular ultrasound (IVUS) to justify the overall cost including the lasers.

* * *

The present work attempts to bridge the gap between the simplicity of piezo arrays, the wideband (ie, mechanically non-resonant) nature of optical detectors,[5] and the wide-area lithographic compatibility of CMUT. We propose a system comprising an array of sub-millimetre-scale metallic electromagnetic resonators printed on a high acoustic impedance dielectric substrate, and a low acoustic impedance superstrate. The resonances can be excited by signals generated from monolithic microwave integrated circuit (MMIC) frequency synthesisers, which have recently become available at the necessary frequencies (ie, millimetre wave frequencies above 30 GHz) for full spatial sampling of megahertz ultrasound signals. Such a system would naturally implement frequency division multiplexing (FDM), as each resonator could be assigned a different resonance and 'addressed' by tuning the microwave source. In this manner, electrical cross-talk between adjacent elements is eliminated, and the device can employ a single electrical readout pathway for multiple elements, reducing the need for RF switching and its associated costs and losses. Additionally, the device can be produced by conventional printed circuit board (PCB) patterning and assembly, making the manufacture process fully compatible with existing consumer electronic fabrication infrastructure.

Future embodiments of the technology could involve a mixed-signal application-specific integrated circuit (ASIC) produced by standard CMOS or MMIC processes, and do so without the need for a custom MEMS process. This would provide an alternative route toward the long-standing goal of ultrasound-on-a-chip for mass-market consumer products, such as personal health monitoring and novel

[5] Any device may be considered "wideband" if operated far enough below its resonant frequency, where its transfer function is flat. However, our devices operate as $\lambda/4$ acoustic cavities, which are known to have relatively flat frequency response and high coupling efficiency. In other words, a wide range of acoustic frequencies couple efficiently into the mechanical vibration modes of the device. We build on previous work on optical hydrophones to derive a theoretical treatment of this phenomenon in §4.2.2

user interaction modalities. Finally, by using chirped radar signals as the high-frequency carrier, the ultrasound signal can be near-instantaneously captured across a wide aperture, whilst fully preserving the spatial information of the ultrasound pressure field. This would enable the capture of high-speed ultrasound events without the need for large numbers of independent digitisation channels. Such devices could find use in focused ultrasound therapy (FUS), allowing ultrafast nonlinear ultrasound events to be monitored in real-time with just a few digitisation channels (see in particular Figures 3.12 and 3.13 for a comparison between conventional systems and our proposed microwave FDM system).

The work carried out, as laid out in the thesis, involves the development and theoretical analysis of such a device, termed microwave oscillator ultrasound receiver (MOUR) [31]. We describe the implementation of a proof-of-concept device operating in the sub-3 GHz band and measure its performance. Finally, we address the challenges of developing the concept from a lab experiment into a fully-fledged multiplexed device, including careful analysis of design considerations and potential applications.

Details of Significant Contributions Presented in this Work

We wish to draw the reader's attention to the aspects of the thesis which we believe to be entirely novel. Firstly, the concept of MOUR—the use of an electromagnetic resonator to detect ultrasound—we believe to have no precedent in the literature. We presented some of this work at an international conference [31], omitting some details, and have filed a United States patent covering the idea. The resonator design developed in §4.1 which combines a defected microstrip structure with tapered impedance matching sections was partly inspired by the work

of colleague James Seddon, but is otherwise original.

In §2.2.3, we present the author's own mathematical representation of beamforming, which in particular has the attractive property of using the same basic equation for both focusing during transmission and focusing during reception/holographic reconstruction. The purpose of this section is not to suggest a new technique for beamforming, but rather to illustrate the necessary tradeoffs in resolution, power, and contrast in a compact mathematical formalism. Generally we found that the literature either considers beamforming as a way of distinguishing the different directions of arrival (DOA) of plane waves to image dense structures [64], or localising point-sources [65–67]. In our work, we instead consider the way in which the practice of beamforming in ultrasound imaging unifies the concepts of imaging resolution, focal point size, and performance of a spatial filter.

In §3.1, we prove a lemma which states that it is impossible to encode spatial information held by one field of travelling waves with another if the speed of the waves in the second field is faster than the speed of the waves in the first. We believe this to be an original, although uncontroversial, insight.

In §4.2.2, we developed a new model for the acoustic structures considered in [68]. Whereas in [68] up to five reflections are counted, in our model an infinite number of reflections are accounted for, and there turns out to be a single analytic expression which can describe almost all combinations of acoustic impedance.

Finally, in §6.1.4, we introduce the concept of software defined transducers (SDTs), a way of combining low-Q/wideband ultrasound transducers with RF signal processing to create a dynamically re-configurable ultrasound transducer. Although it is inspired by software-defined radio, we are not aware of any application of this principle for ultrasound imaging systems.

References

[1] A. F Metherell, H. M. A El-Sum, and Lewis Larmore. *Acoustical Holography: Volume 1 Proceedings of the First International Symposium on Acoustical Holography, Held at the Douglas Advanced Research Laboratories, Huntington Beach, California December 14-15, 1967*. Boston, MA: Springer US, 1995. isbn: 978-1-4615-8204-5. url: http://dx.doi.org/10.1007/978-1-4615-8204-5 (visited on 03/26/2019).

[2] Henrik Møller. "Fundamentals of Binaural Technology". In: *Applied Acoustics* 36.3 (Jan. 1, 1992), pp. 171–218. issn: 0003-682X. doi: 10.1016/0003-682X(92)90046-U. url: http://www.sciencedirect.com/science/article/pii/0003682X9290046U (visited on 03/22/2019).

[3] Axel Donges. "The Coherence Length of Black-Body Radiation". In: *European Journal of Physics* 19.3 (May 1998), pp. 245–249. issn: 0143-0807. doi: 10.1088/0143-0807/19/3/006. url: https://doi.org/10.1088%2F0143-0807%2F19%2F3%2F006 (visited on 03/22/2019).

[4] Michael F. Deering. "The Limits of Human Vision". In: *2nd International Immersive Projection Technology Workshop*. Vol. 2. 1998.

[5] J. W. S. Rayleigh. "Theory of Sound, Volume 1 (2nd Edition Revised and Enlarged)". In: (1877). issn: 978-0-486-60292-9. url: https://app.knovel.com/hotlink/toc/id:kpTSVERE04/theory-sound-volume-1/theory-sound-volume-1.

[6] Beatrice D. Lawrence and James A. Simmons. "Measurements of Atmospheric Attenuation at Ultrasonic Frequencies and the Significance for Echolocation by Bats". In: *The Journal of the Acoustical Society of America* 71.3 (Mar. 1, 1982), pp. 585–590. issn: 0001-4966. doi: 10.1121/1.387529. url: https://asa.scitation.org/doi/abs/10.1121/1.387529 (visited on 03/25/2019).

[7] Tae Soo Park. "Automotive Rear Safety Detection System". U.S. pat. 5650765A. Park; Tae Soo. July 22, 1997. url: https://patents.google.com/patent/US5650765A/en (visited on 03/25/2019).

[8] R. J. Vaccaro. "The Past, Present, and the Future of Underwater Acoustic Signal Processing". In: *IEEE Signal Processing Magazine* 15.4 (July 1998), pp. 21–51. issn: 1053-5888. doi: 10.1109/79.689583.

[9] K. F. Graff. “Ultrasonics: Historical Aspects”. In: *1977 Ultrasonics Symposium*. 1977 Ultrasonics Symposium. Oct. 1977, pp. 1–10. doi: 10.1109/ULTSYM.1977.196782.

[10] Harold Berger. “A Survey of Ultrasonic Image Detection Methods”. In: *Acoustical Holography*. Ed. by A. F. Metherell, H. M. A. El-Sum, and Lewis Larmore. Springer US, 1969, pp. 27–48. isbn: 978-1-4615-8204-5.

[11] Richard S. C. Cobbold. *Foundations of Biomedical Ultrasound*. Oxford University Press, Sept. 7, 2006. 844 pp. isbn: 978-0-19-977512-5. Google Books: Hwb5D60vb5IC.

[12] Sokoloff Sergey. “Means for Indicating Flaws in Materials”. U.S. pat. 2164125A. Sokoloff Sergey. June 27, 1939. url: https://patents.google.com/patent/US2164125A/en?inventor=Sokoloff+Sergey (visited on 11/13/2019).

[13] Anant K. Nigam and J. C. French. “Modified Sokolov Camera Utilizing Condenser-Microphone Arrays of the Foil-Electret Type”. In: *Acoustical Holography: Volume 5*. Ed. by Philip S. Green. Boston, MA: Springer US, 1974, pp. 685–700. isbn: 978-1-4757-0827-1. doi: 10.1007/978-1-4757-0827-1_41. url: https://doi.org/10.1007/978-1-4757-0827-1_41 (visited on 11/13/2019).

[14] H. Berger and R. E. Dickens. *A Review of Ultrasonic Imaging Methods*. ANL-6680. Argonne National Lab., Ill., July 1, 1963. doi: 10.2172/4659542. url: https://www.osti.gov/biblio/4659542 (visited on 03/29/2019).

[15] R. T. Beyer. “Recent Research in Ultrasonics and Physical Acoustics in the USSR”. In: *Il Nuovo Cimento* 4.S1 (May 1956), pp. 31–64. issn: 0029-6341, 1827-6121. doi: 10.1007/BF02743688. url: http://link.springer.com/10.1007/BF02743688 (visited on 04/01/2019).

[16] Gunter Radig. “An Electronic to Ultrasonic Image Converter Tube”. In: *Ultrasonics* 5.4 (Oct. 1, 1967), pp. 235–238. issn: 0041-624X. doi: 10.1016/0041-624X(67)90069-8. url: http://www.sciencedirect.com/science/article/pii/0041624X67900698 (visited on 04/01/2019).

[17] Philip Green. *Acoustical Holography*. Springer Science & Business Media, 1974. 732 pp. isbn: 978-1-4757-0827-1. Google Books: fgnkBwAAQBAJ.

[18] R.K. Mueller. “Acoustic Holography”. In: *Proceedings of the IEEE* 59.9 (Sept. 1971), pp. 1319–1335. issn: 1558-2256. doi: 10.1109/PROC.1971.8407.

[19] P. T. Gough and D. W. Hawkins. “A Short History of Synthetic Aperture Sonar”. In: *IGARSS ’98. Sensing and Managing the Environment. 1998 IEEE International Geoscience and Remote Sensing. Symposium Proceedings. (Cat. No.98CH36174)*. IGARSS ’98. Sensing and Managing the Environment. 1998 IEEE International Geoscience and Remote Sensing. Symposium Proceedings. (Cat. No.98CH36174). Vol. 2. July 1998, 618–620 vol.2. doi: 10.1109/IGARSS.1998.699529.

[20] D.G. Tucker, V.G. Welsby, and R. Kendell. “Electronic Sector Scanning”. In: *Journal of the British Institution of Radio Engineers* 18.8 (Aug. 1958), pp. 465–482. issn: 2054-054X. doi: 10.1049/jbire.1958.0053. url: https://digital-library.theiet.org/content/journals/10.1049/jbire.1958.0053 (visited on 04/03/2019).

[21] J. J. Wild and J. M. Reid. “Application of Echo-Ranging Techniques to the Determination of Structure of Biological Tissues”. In: *Science* 115.2983 (Feb. 29, 1952), pp. 226–230. issn: 0036-8075, 1095-9203. doi: 10.1126/science.115.2983.226. url: http://www.sciencemag.org/cgi/doi/10.1126/science.115.2983.226 (visited on 04/03/2019).

[22] W. Buschmann. “New Equipment and Transducers for Ophthalmic Diagnosis”. In: *Ultrasonics* 3.1 (Jan. 1965), pp. 18–21. issn: 0041624X. doi: 10.1016/0041-624X(65)90234-9. url: http://linkinghub.elsevier.com/retrieve/pii/0041624X65902349 (visited on 04/03/2019).

[23] J. C. Somer. “Electronic Sector Scanning for Ultrasonic Diagnosis”. In: *Ultrasonics* 6.3 (July 1, 1968), pp. 153–159. issn: 0041-624X. doi: 10.1016/0041-624X(68)90277-1. url: http://www.sciencedirect.com/science/article/pii/0041624X68902771 (visited on 04/02/2019).

[24] O. Couture et al. “Ultrasound Localization Microscopy and Super-Resolution: A State of the Art”. In: *IEEE Transactions on Ultrasonics, Ferroelectrics, and Frequency Control* 65.8 (Aug. 2018), pp. 1304–1320. issn: 0885-3010. doi: 10.1109/TUFFC.2018.2850811.

[25] P. N. Keating. “Acoustical Holography — A Comparison with Phased Array Sonar”. In: *Acoustical Holography: Volume 5*. Ed. by Philip S. Green. Boston, MA: Springer US, 1974, pp. 231–237. isbn: 978-1-4757-0827-1. doi: 10.1007/978-1-4757-0827-1_14. url: https://doi.org/10.1007/978-1-4757-0827-1_14 (visited on 04/01/2019).

[26] K. E. Thomenius. “Evolution of Ultrasound Beamformers”. In: *1996 IEEE Ultrasonics Symposium. Proceedings*. 1996 IEEE Ultrasonics Symposium. Proceedings. Vol. 2. Nov. 1996, 1615–1622 vol.2. doi: 10.1109/ULTSYM.1996.584398.

[27] Douglas Miller et al. “Overview of Therapeutic Ultrasound Applications and Safety Considerations”. In: *Journal of ultrasound in medicine : official journal of the American Institute of Ultrasound in Medicine* 31.4 (Apr. 2012), pp. 623–634. issn: 0278-4297. pmid: 22441920. url: http://www.ncbi.nlm.nih.gov/pmc/articles/PMC3810427/ (visited on 10/21/2016).

[28] Michael J. Eberle, Gary P. Rizzuti, and Horst F. Kiepen. “Ultrasound Transducer Assembly”. U.S. pat. 6962567B2. Volcano Corp. Nov. 8, 2005. url: https://patents.google.com/patent/US6962567B2/en?q=ultrasound&assignee=Volcano+Corporation&oq=assignee:(Volcano+Corporation)+ultrasound (visited on 04/03/2019).

[29] Jørgen Arendt Jensen et al. “Synthetic Aperture Ultrasound Imaging”. In: *Ultrasonics* 44 (Dec. 2006), e5–e15. issn: 0041624X. doi: 10.1016/j.ultras.2006.07.017. url: http://linkinghub.elsevier.com/retrieve/pii/S0041624X06003374 (visited on 06/19/2017).

[30] Seung-Eek Eagle Park and Wesley Hackenberger. “High Performance Single Crystal Piezoelectrics: Applications and Issues”. In: *Current Opinion in Solid State and Materials Science* 6.1 (Feb. 1, 2002), pp. 11–18. issn: 1359-0286. doi: 10.1016/S1359-0286(02)00023-2. url: http://www.sciencedirect.com/science/article/pii/S1359028602000232 (visited on 09/25/2019).

[31] T. S. Robbins et al. “Microwave Oscillator Ultrasound Receivers”. In: *2018 IEEE International Ultrasonics Symposium (IUS)*. 2018 IEEE International Ultrasonics Symposium (IUS). Oct. 2018, pp. 1–4. doi: 10.1109/ULTSYM.2018.8580205.

[32] Frederick V. Hunt. *Electroacoustics: The Analysis of Transduction, and Its Historical Background*. 5. Acoustical Society of America, 1954.

[33] P. R. Scheeper et al. “A Review of Silicon Microphones”. In: *Sensors and Actuators A: Physical* 44.1 (July 1, 1994), pp. 1–11. issn: 0924-4247. doi: 10.1016/0924-4247(94)00790-X. url: http://www.sciencedirect.com/science/article/pii/092442479400790X (visited on 02/21/2018).

[34] Warren P. Mason. “Piezoelectricity, Its History and Applications”. In: *The Journal of the Acoustical Society of America* 70.6 (Dec. 1, 1981), pp. 1561–1566. issn: 0001-4966. doi: 10.1121/1.387221. url: http://scitation.aip.org/content/asa/journal/jasa/70/6/10.1121/1.387221 (visited on 05/10/2016).

[35] X. Cheng et al. “CMUT-in-CMOS Ultrasonic Transducer Arrays with on-Chip Electronics”. In: *TRANSDUCERS 2009 - 2009 International Solid-State Sensors, Actuators and Microsystems Conference*. TRANSDUCERS 2009 - 2009 International Solid-State Sensors, Actuators and Microsystems Conference. June 2009, pp. 1222–1225. doi: 10.1109/SENSOR.2009.5285878.

[36] M. I. Haller and B. T. Khuri-Yakub. “A Surface Micromachined Electrostatic Ultrasonic Air Transducer”. In: *IEEE Transactions on Ultrasonics, Ferroelectrics, and Frequency Control* 43.1 (Jan. 1996), pp. 1–6. issn: 0885-3010. doi: 10.1109/58.484456.

[37] J. M. Baran and J. G. Webster. “Design of Low-Cost Portable Ultrasound Systems: Review”. In: *2009 Annual International Conference of the IEEE Engineering in Medicine and Biology Society*. 2009 Annual International Conference of the IEEE Engineering in Medicine and Biology Society. Sept. 2009, pp. 792–795. doi: 10.1109/IEMBS.2009.5332754.

[38] Kevin Brenner et al. “Advances in Capacitive Micromachined Ultrasonic Transducers”. In: *Micromachines* 10.2 (Feb. 2019), p. 152. doi: 10.3390/mi10020152. url: https://www.mdpi.com/2072-666X/10/2/152 (visited on 03/12/2019).

[39] J. Mufioz et al. “Monolithical AlN PMUT on Pre-Processed CMOS Substrate”. In: *2018 IEEE International Frequency Control Symposium (IFCS)*. 2018 IEEE International Frequency Control Symposium (IFCS). May 2018, pp. 1–3. doi: 10.1109/FCS.2018.8597560.

[40] Philip S. Green et al. “Ultrasonic Camera System and Method”. U.S. pat. 3937066A. SRI International. Feb. 10, 1976. url: https://patents.google.com/patent/US3937066A/en (visited on 03/27/2019).

[41] C. Chen et al. “A Front-End ASIC With Receive Sub-Array Beamforming Integrated With a 32×32 PZT Matrix Transducer for 3-D Transesophageal Echocardiography”. In: *IEEE Journal of Solid-State Circuits* 52.4 (Apr. 2017), pp. 994–1006. issn: 0018-9200. doi: 10.1109/JSSC.2016.2638433.

[42] B. Savord and R. Solomon. “Fully Sampled Matrix Transducer for Real Time 3D Ultrasonic Imaging”. In: *IEEE Symposium on Ultrasonics, 2003.* IEEE Symposium on Ultrasonics, 2003. Vol. 1. Oct. 2003, 945–953 Vol.1. doi: 10.1109/ULTSYM.2003.1293556.

[43] Neal R. Butler and Marvin E. Lasser. “Two Dimensional Transducer Integrated Circuit”. U.S. pat. 5483963A. Lockheed Martin IR Imaging Systems Inc. Jan. 16, 1996. url: https://patents.google.com/patent/US5483963A/en?assignee=Imperium%2c+Inc. (visited on 06/18/2019).

[44] Robert S. Lasser and David C. Rich. “Image Sensor for Large Area Ultrasound Mapping”. U.S. pat. 20150369909A1. Imperium Inc. Dec. 24, 2015. url: https://patents.google.com/patent/US20150369909A1/en?assignee=Imperium%2c+Inc.&page=2 (visited on 06/18/2019).

[45] Dipen N. Sinha and John F. Brady. “Acoustic Camera”. Pat. WO2013165569A1 (WO). Los Alamos National Security, Llc. Nov. 7, 2013. url: https://patents.google.com/patent/WO2013165569A1/en (visited on 06/19/2019).

[46] Dipen N. Sinha and John F. Brady. “Acoustic Camera”. U.S. pat. 10054676B2. Los Alamos National Security LLC. Aug. 21, 2018. url: https://patents.google.com/patent/US10054676B2/en (visited on 06/19/2019).

[47] Il Kwon CHUNG and Joo Hyun Kim. “Fingerprint Sensor and Electronic Device Including the Same”. U.S. pat. 9465972B2. Samsung Electro Mechanics Co Ltd. Oct. 11, 2016. url: https://patents.google.com/patent/US9465972B2/en?q=ultrasonic+fingerprint&assignee=samsung (visited on 07/10/2019).

[48] John K. Schneider, Jack C. Kitchens, and James T. Baker. “Ultrasonic Fingerprint Scanning Utilizing a Plane Wave”. U.S. pat. 7739912B2. Ultra-Scan Corp. June 22, 2010. url: https://patents.google.com/patent/US7739912B2/en (visited on 07/10/2019).

[49] John K. Schneider and Jack C. Kitchens. “Hydrophone Array Module”. U.S. pat. 7436736B2. Ultra-Scan Corp. Oct. 14, 2008. url: https://patents.google.com/patent/US7436736B2/en?q=tft&assignee=Ultra-Scan+Corporation&oq=assignee:(Ultra-Scan+Corporation)+tft (visited on 07/10/2019).

[50] W. Spence. “Stored Charge Transducer”. U.S. pat. 3786495A. NCR. Jan. 15, 1974. url: https://patents.google.com/patent/US3786495A/en (visited on 07/10/2019).

[51] D. J. McCarron. *A Guide to Acousto-Optic Modulators*. Technical report, Durham University, 2007. url: http://jila1.nickersonm.com/papers/A%20Guide%20to%20Acousto-Optic%20Modulators.pdf (visited on 06/16/2017).

[52] D. R. Bacon. “Primary Calibration of Ultrasonic Hydrophone Using Optical Interferometry”. In: *IEEE Transactions on Ultrasonics, Ferroelectrics, and Frequency Control* 35.2 (Mar. 1988), pp. 152–161. issn: 0885-3010. doi: 10.1109/58.4165.

[53] A. D. W. McKie et al. “Laser Generation of Narrow-Band and Directed Ultrasound”. In: *Ultrasonics* 27.6 (Nov. 1, 1989), pp. 323–330. issn: 0041-624X. doi: 10.1016/0041-624X(89)90030-9. url: http://www.sciencedirect.com/science/article/pii/0041624X89900309 (visited on 11/10/2016).

[54] Malcolm C. Finlay et al. “Through-Needle All-Optical Ultrasound Imaging in Vivo: A Preclinical Swine Study”. In: *Light: Science & Applications* 6.12 (Dec. 2017), e17103. issn: 2047-7538. doi: 10.1038/lsa.2017.103. url: https://www.nature.com/articles/lsa2017103 (visited on 03/14/2018).

[55] James A. Guggenheim et al. “Ultrasensitive Plano-Concave Optical Microresonators for Ultrasound Sensing”. In: *Nature Photonics* 11.11 (Oct. 31, 2017), p. 714. issn: 1749-4893. doi: 10.1038/s41566-017-0027-x. url: https://www.nature.com/articles/s41566-017-0027-x (visited on 11/03/2017).

[56] P. C. Beard et al. “Comparison of a Miniature, Ultrasonic, Optical Fibre Hydrophone with PVDF Hydrophone Technology”. In: *1998 IEEE Ultrasonics Symposium. Proceedings (Cat. No. 98CH36102)*. 1998 IEEE Ultrasonics Symposium. Proceedings (Cat. No. 98CH36102). Vol. 2. 1998, 1881–1884 vol.2. doi: 10.1109/ULTSYM.1998.765319.

[57] Richard J. Colchester et al. “Laser-Generated Ultrasound with Optical Fibres Using Functionalised Carbon Nanotube Composite Coatings”. In: *Applied Physics Letters* 104.17 (2014), p. 173502. url: http://scitation.aip.

org/content/aip/journal/apl/104/17/10.1063/1.4873678 (visited on 11/12/2015).

[58] Erwin J. Alles and Adrien E. Desjardins. "Real-Time 2D All-Optical Ultrasound Imaging with a Dynamically Reconfigurable Imaging Aperture (Conference Presentation)". In: *Photons Plus Ultrasound: Imaging and Sensing 2019*. Photons Plus Ultrasound: Imaging and Sensing 2019. Vol. 10878. International Society for Optics and Photonics, Mar. 4, 2019, p. 108780I. doi: 10.1117/12.2507792. url: https://www.spiedigitallibrary.org/conference-proceedings-of-spie/10878/108780I/Real-time-2D-all-optical-ultrasound-imaging-with-a-dynamically/10.1117/12.2507792.short (visited on 05/23/2019).

[59] Erwin J Alles et al. "Reconfigurable 1.5D Source Arrays for Improved Elevational Focussing in All-Optical Ultrasound Imaging". In: *2018 IEEE International Ultrasonics Symposium (IUS)*. 2018 IEEE International Ultrasonics Symposium (IUS). Kobe: IEEE, Oct. 2018, pp. 1–9. isbn: 978-1-5386-3425-7. doi: 10.1109/ULTSYM.2018.8580210. url: https://ieeexplore.ieee.org/document/8580210/ (visited on 05/23/2019).

[60] Erwin J. Alles et al. "A Reconfigurable All-Optical Ultrasound Transducer Array for 3D Endoscopic Imaging". In: *Scientific Reports* 7 (Apr. 26, 2017), p. 1208. issn: 2045-2322. doi: 10.1038/s41598-017-01375-2.

[61] P. C. Beard and T. N. Mills. "Miniature Optical Fibre Ultrasonic Hydrophone Using a Fabry-Perot Polymer Film Interferometer". In: *Electronics Letters* 33.9 (Apr. 1997), pp. 801–803. issn: 0013-5194. doi: 10.1049/el:19970545.

[62] Henrick Gille et al. "Component-Based Catheter Lab Intravascular Ultrasound System". U.S. pat. 20070232933A1. Volcano Corp. Oct. 4, 2007. url: https://patents.google.com/patent/US20070232933A1/en (visited on 05/23/2019).

[63] Richard J. Colchester et al. "All-Optical Rotational Ultrasound Imaging". In: *Scientific Reports* 9.1 (Apr. 3, 2019), p. 5576. issn: 2045-2322. doi: 10.1038/s41598-019-41970-z. url: https://www.nature.com/articles/s41598-019-41970-z (visited on 05/23/2019).

[64] B.D. Van Veen and K.M. Buckley. "Beamforming: A Versatile Approach to Spatial Filtering". In: *IEEE ASSP Magazine* 5.2 (Apr. 1988), pp. 4–24. issn:

0740-7467. doi: 10.1109/53.665. url: http://ieeexplore.ieee.org/document/665/ (visited on 09/17/2020).

[65] J.C. Chen, Kung Yao, and R.E. Hudson. "Source Localization and Beamforming". In: *IEEE Signal Processing Magazine* 19.2 (Mar. 2002), pp. 30–39. issn: 1558-0792. doi: 10.1109/79.985676.

[66] Kung Yao et al. "Blind Beamforming on a Randomly Distributed Sensor Array System". In: *IEEE Journal on Selected Areas in Communications* 16.8 (Oct. 1998), pp. 1555–1567. issn: 1558-0008. doi: 10.1109/49.730461.

[67] D. Malioutov, M. Cetin, and A.S. Willsky. "A Sparse Signal Reconstruction Perspective for Source Localization with Sensor Arrays". In: *IEEE Transactions on Signal Processing* 53.8 (Aug. 2005), pp. 3010–3022. issn: 1941-0476. doi: 10.1109/TSP.2005.850882.

[68] P. C. Beard and T. N. Mills. "Extrinsic Optical-Fiber Ultrasound Sensor Using a Thin Polymer Film as a Low-Finesse Fabry–Perot Interferometer". In: *Applied Optics* 35.4 (Feb. 1, 1996), pp. 663–675. issn: 2155-3165. doi: 10.1364/AO.35.000663. url: https://www.osapublishing.org/abstract.cfm?uri=ao-35-4-663 (visited on 12/15/2017).

Chapter 2

Ultrasound

Ultrasound is a branch of acoustics, a well-established science whose main equations were assembled by Rayleigh in 1877 [1], in a similar manner to (and four years after) Maxwell's more famous treatise on electromagnetism [2]. Whereas Maxwell's equations had empirical origins, the equations for sound propagation may be derived from—and are a consequence of—thermodynamics and classical mechanics. We will outline the theory of acoustic propagation in §2.2, and also examine the consequences of non-linear ultrasound for imaging.

Before outlining acoustic theory, we will summarise some current and emerging applications of ultrasound in §2.1. We broadly divide these into two categories: ultrasound imaging (§2.2.3); and therapeutic ultrasound (§2.1.2), the use of ultrasound to treat disease.

The chapter concludes with a more thorough explanation and evaluation of current ultrasound devices in §2.3. As in the previous chapter, we focus on three main forerunners to the present work: piezoelectric transducers, CMUTs, and optical hydrophones. These three established ultrasound transducer mechanisms will be contrasted in Chapter 3 with the mechanism of MOUR, which has trade-offs with each, but ultimately offers a unique combination of features which make it well-suited to some of the emerging applications discussed in §2.1.

2.1 Current and Emerging Applications of Ultrasound

In this section we review some of the current and emerging applications of ultrasound in the clinical context. We divide these applications into two subsections, the first concerning imaging and elastography (using ultrasound to form an image or make a measurement), and the second concerning ultrasound therapy, where ultrasound is used to modify tissue.

2.1.1 Ultrasound Imaging and Elastography

Ultrasound is one of the most widely-used medical imaging modalities (second only to X-ray) [3]. It is used routinely for high-resolution subcutaneous imaging in a variety of medical contexts, from cancer screening [4] to emergency medicine [5]. We restrict ourselves to two types of ultrasound imaging geometries: 1D-array B-mode ultrasound, and 2D-array C-mode ultrasound (see Figure 2.1).

The designations 'B-mode' and 'C-mode' have historical origins. 'B-mode' stands for 'Brightness-mode', so-named to distinguish it from 'Amplitude-mode' (A-mode) ultrasound, whereby the distance between the face of the transducer and some defect is measured by the x-axis distance between the initial ultrasound pulse and its echo, where each pulse and echo is represented by a sharp y-deflection on the oscilloscope trace. In B-mode ultrasound, the transducer voltage instead modulates the brightness of the oscilloscope trace. Each 1D line (of varying brightness) now represents a single ultrasound channel, so by adding channels (which may simply be multiplexed into the time-domain), a 2D picture can be built up with brightness representing acoustic contrast (measured by the strength of the received echo), the y-position representing the time-delay between the initial pulse transmission and its echo—which maps to the z-position of the defect—and

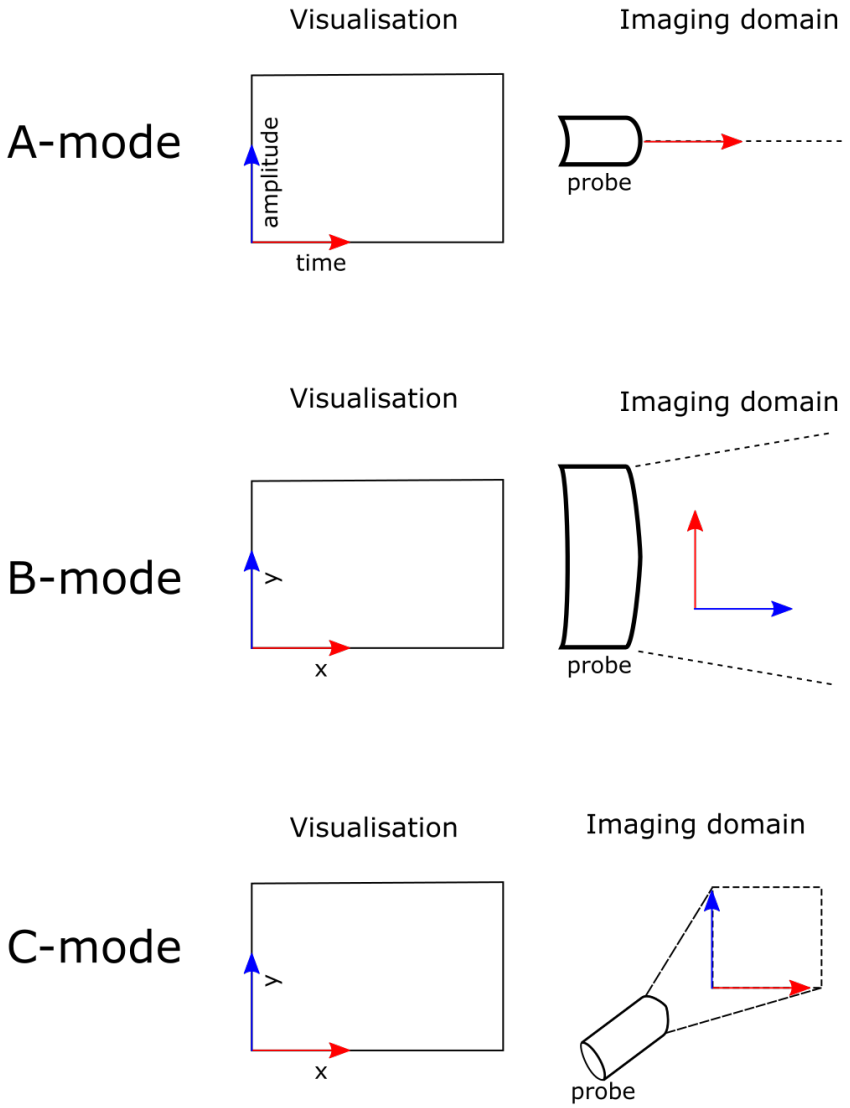

Figure 2.1: Summary of the three main ultrasound imaging modes

the x-position corresponding to the angle of the defect measured from the normal of the transducer array face. [6].

In C-mode ultrasound ('C' doesn't stand for anything, rather it is simply the next letter in the sequence A-mode, B-mode, C-mode), we instead focus to a plane normal to the z-axis. Building a 2D image in this instance requires a 2D array of individually addressable ultrasound elements, each with a narrow focus depth. This can be achieved in one

of two ways: dynamically or physically. Physical focusing relies on an arrangement of acoustic lenses and apertures to select waves being reflected from a certain depth. In dynamic focusing (also known as synthetic aperture imaging), the image is holographically reconstructed using the full phase and amplitude information captured by the array, or uses one or more ultrasound illumination patterns, which can involve activating/deactivating certain elements or introducing phase delays. Some systems use a combination of all these focusing methods.

2.1.1.1 Pulse-Echo Imaging

In all of the above examples, we have assumed that the ultrasound receivers and transmitters are coincident - ie, duplexed. This is (vastly) the most common form of ultrasound imaging. It relies on the reflection of short ultrasound pulses back towards the transducer. The transducers are rapidly switched between transmit and receive circuitry, the former of which must be able to drive the transducers at high voltages in order to generate strong pulses, and the latter of which needs to be able to detect microvolt signals coming from the transducers due to the reflected pulses. At the boundaries between different types of tissue, the difference in acoustic impedance causes a partial reflection of the ultrasound pulse. Sub-wavelength features cause acoustic backscatter, and due to the high coherence of ultrasound this appears in images as a speckle pattern. The strength of that reflection is encoded into the brightness of that spot in the image, and the time it took for that reflection to arrive is encoded into its z-position.

For B-mode 2D ultrasound images, there are several possible probe configurations. Linear array probes comprise a straight-line array of duplexed piezo elements which each send a collimated pulse of ultrasound along the z-axis, and detect its echoes. This gives a field of view no greater than the width of the device. Curved arrays over-

come this limitation by arranging the elements such that each transmits and receives radially, increasing the field of view. Finally, phased arrays use all elements (or groups of them) simultaneously with relative phase delays to transmit each pulse, allowing the beam to be steered through a wide angle. Alternatively, all (or groups of) elements can be used in reception and delays can be added in receive to achieve the same effect.

Pulse-echo imaging need not imply the use of duplexed or even co-located transmit-and-receive transducers. It is possible to arrange a plane-wave acoustic source and a multiplexed receiver array such that they each have a normal line-of-sight to the imaging target [7]. This configuration makes use of geometric acoustics which bears a strong resemblance to free-space optical devices such as spectrometers. These devices are used in non-destructive testing (NDT), and to the best of the author's knowledge are yet to find use in biomedical contexts.

2.1.1.2 Elastography

As well as using ultrasound to visualise anatomical structure, ultrasound may also be used to infer quantitative or qualitative information about the mechanical properties of tissue. The extent to which these mechanical properties relate to clinical endpoints is the subject of ongoing research [8]. For instance, a recent meta-study concluded that shear wave elastography (SWE) could have comparable false-negative rates to biopsy for diagnosing prostate cancer [9], and other clinical studies have found similarly promising results (see review [10] and references therein). Mechanical tissue properties can be inferred in a variety of ways, such as manually compressing tissue and recording its deformation properties using standard B-mode ultrasound [11], but in the present work we are most interested in techniques which can infer

the mechanical properties of tissue using only a stationary ultrasound probe [12]. This ties in more broadly with non-linear ultrasound (discussed in §2.2.2), where the assumptions of linearity (see §2.2.1) no longer hold. In general, this breaks the symmetry of the ultrasound equations under time reversal, making true image reconstruction impossible. From a transducer design perspective, this changes the performance goals, and we discuss this in §2.3.

We outline here one prominent all-ultrasound elastographic technique, known as acoustic radiation force impulse (ARFI) elastography. In soft tissue, the predominant mechanism for ultrasound attenuation is through absorption. Therefore, an ultrasound pulse with intensity I will impart a force F given by

$$F = 2\alpha I/c, \tag{2.1}$$

where α and c are the medium absorption and sound speed respectively.

This force, when applied to small regions of tissue in short pulses, has two effects: firstly, it creates a deformation within that region, and secondly, it generates a shear wave which propagates away from the region. The deformation of the small region can be detected by a subsequent lower-power pulse (known as a tracking beam), and from this the (shear) stiffness of that region of tissue inferred. In general, most ultrasound energy in soft tissue is carried by longitudinal (compression) waves. What is notable about this technique is that it allows the inference of shear elasticity using longitudinal ultrasound waves. This is important because tissues vary significantly more in their shear elasticities than their bulk elasticities—shear elasticity is more determined by higher-level inter-cellular forces, as opposed to shorter-range (and more homogeneous) molecular forces [13]—making shear elasticity

far more useful as a tissue classification parameter [14]. Due to the small deformations encountered, Doppler techniques, or more generally digital RF analysis, may be need to be used [6, 14].

As might be expected, ultrasound elastography poses some significant signal processing challenges. The motion of the tissue within the region of excitation (ROE) must be extracted from among various motion artefacts such as movement of the probe or physiological movements [12]. Furthermore, in order to deliver a force F large enough to create detectable tissue motion, a greater pulse intensity I is needed than would be in standard B-mode ultrasound imaging. Thus, for a given intensity limit (safe limits for ultrasound exposure given in [15]) the maximum imaging depth for ARFI is lower than for standard B-mode imaging. Since attenuation in soft tissue is generally frequency dependent, one way to improve the depth of penetration is to use a lower ultrasound frequency for the excitation beam and a higher frequency for the tracking beam, where high resolution is necessary.

We will discuss later how the above considerations may necessitate a rethink in transducer and imaging array design, particularly with regard to frequency response and acquisition speed.

2.1.2 Active Ultrasound

Active ultrasound refers to the use of ultrasound energy to effect changes to tissue. There are generally two mechanisms by which this happens: thermal and non-thermal/mechanical [16]. We present in the following paragraphs some historical background, before outlining the physical basis of these mechanisms.

In the original experiments on underwater ultrasonics by Paul Langevin around 1917, it was noticed that fish were killed by exposure to intense beams of ultrasound. The work was observed by American physicist R. W. Wood, who went so far as to place his hand in the beam

and recorded feeling "an almost insupportable pain, which gave one the impression that bones were being heated". Further experiments were carried out by Wood in collaboration with Alfred Loomis around 1928. Loomis was a self-financed scholar who funded many physics experiments in his personal laboratory, thanks to a highly successful former career on Wall Street [17]. Along with the heating effects of intense beams of sound, they noted the formation of tiny bubbles, leading to the systematic study of acoustic cavitation [18]. Serious work on using active ultrasound in medicine (beyond spurious claims of ultrasonic panaceas which were common in the 1940s) came in 1953 with work by W. J. Fry and colleagues on the use of focused beams of ultrasound as an alternative to neurosurgery. One of the limitations of this work was that it required the removal of part of the skull in order to be effective. Early applications were on treatment of Parkinson's, and although initial clinical trials in the 1960s showed promising results, the work coincided with the development of the drug *L-dopa*, which provided adequate treatment of the disease. Similarly, efforts to bring therapeutic ultrasound to the realm of ophthalmology were superseded by the now widespread practice of laser eye surgery [19].

A note on nomenclature: the literature refers variously to active ultrasound, therapeutic ultrasound, focused ultrasound therapy (FUS) and high-intensity focused ultrasound therapy (HIFU). Confusingly, these terms each address a slightly different but highly overlapping field of research. Additionally, these ideas are not to be confused with lithotripsy, which involves the use of low-frequency shock-waves to break up objects such as kidney stones. In this section we are generally interested in the use of high ultrasound intensities—in other words, intensities above the clinically safe limits proscribed for ultrasound imaging—to treat disease.

2.1.2.1 Ultrasonic Heating

The heating effects of ultrasound (or sound waves generally) result mainly from the viscous energy losses of acoustic transmission. The general theory of acoustic absorption is complicated [20], but it can be approximated by the equation

$$A_z = A_0 e^{-(\mu_s+\mu_a)z}, \tag{2.2}$$

where A_0 and A_z are the amplitude of the sound wave at 0 and z respectively, and μ_s, μ_a are the attenuation coefficients for scattering and absorption respectively, empirically determined depending on the medium. In general, μ_s and μ_a are frequency-dependent.

Differentiating the above, the energy E absorbed and scattered by an ultrasound beam per unit volume is

$$E = 2(\mu_s + \mu_a)I, \tag{2.3}$$

where I is the ultrasound intensity. The energy absorbed alone is given by $2\mu_a I$. The temperature increase due to ultrasound of intensity I (neglecting conduction and convection of heat) is therefore given by

$$dT/dt = (2\mu_a/\rho C_p)I, \tag{2.4}$$

where T is the tissue temperature, ρ is the tissue density, C_p is the tissue specific heat capacity at constant pressure, and t is time [21].

For ultrasound imaging, I is kept low enough such that the heat flow away from the insonated region balances the increase in temperature due to ultrasound absorption. If I is sufficiently high, then rapid temperature increase is possible. Because the effect is proportional to intensity, and ultrasound waves obey the principle of linear superposition (at least within the low-intensity linear regime), it is possible to

focus a beam of ultrasound through tissue and deliver significant temperature increases to a small region far from the transducer interface, whilst leaving the intermediate tissue unaffected.

2.1.2.2 Ultrasound Cavitation

Further increasing the acoustic intensity results in cavitation. There are two possible mechanisms for this: one is the increase of temperature boiling fluid in a small volume, resulting in a vapour-filled bubble; the other is the creation of a region of intense negative pressure [22]. The cavities can grow further by diffusion of gas from the surrounding fluid [21].

These bubbles can be detected by ultrasound due to their nonlinear dynamics, which cause sound waves scattered off them to contain harmonic overtones. When the bubbles collapse, local temperatures can exceed 200 °C [21].

2.1.2.3 Focused Ultrasound Therapy

In many branches of medicine, the successful application of treatment requires the modification of tissue deep inside the body. Reaching these areas whilst minimising irreversible damage to the intervening tissue is the goal of the surgeon. As such, the ability to impart energy on tissue deep inside the body without having to resort to invasive surgery would represent a major improvement to patient safety and make possible treatment of tissue previously deemed inoperable. In recent years, several factors have come together which have caused a revival in interest in HIFU, culminating in several approved therapies [19].

One such factor is improved availability of magnetic resonance imaging (MRI) and computational tomography (CT), which allows the planning and targeting of treatment. This, combined with large phased arrays, makes possible the customisation of acoustic wavefronts ac-

cording to anatomical detail [23]. This enables HIFU to be focused through highly scattering structures, such as the human skull (early therapies required direct physical coupling of the transducer to the brain, necessitating surgical removal of a portion of the skull [24]).

Monitoring the progress of HIFU remains challenging [25]. Thermal therapies can be monitored using certain MRI modes, however MRI alone is generally unable to detect cavitation events. For these, some form of passive acoustic mapping (PAM) is needed. PAM would ideally involve a 2D array of ultrasound sensors, which would allow cavitation events to be mapped in 3D space in real-time [26]. To do this would require each element of the 2D array to have its own readout channel [27].

The present work suggests a way of creating such 2D arrays and overcomes the challenges of constructing them from conventional PZT transducers.

2.2 Ultrasound Theory

In this section we derive the acoustic wave equation starting from basic concepts from thermodynamics and classical mechanics. There are several types of acoustic wave depending on the properties of the media and the boundary conditions, but for our purposes we will concentrate on longitudinal waves, since this is the primary mode of propagation in biological tissue. Shear waves are also present and play an important role in elastography (see §2.1.1.2), but the important points relating to imaging and transducers can be illustrated with longitudinal waves alone.

We then show how, under certain conditions, these equations can be treated as linear, and discuss the consequences of both linear propagation and linear detection for holographic imaging.

Finally, we briefly discuss non-linear ultrasound, where it occurs,

and its relevance to the present work.

2.2.1 Linear Propagation of Ultrasound

The simplest scenario in which to examine linear acoustic propagation is in a homogeneous, isotropic fluid under adiabatic conditions.[1] Within this fluid, consider a 'particle' of fluid—or, in other words, an arbitrarily defined region within the fluid. The net force vector acting on the particle is equal to the integral of the pressure acting normal to the surface which defines the particle boundary:

$$\begin{aligned} \mathbf{F} &= -\iint_S p\hat{\mathbf{n}}\mathrm{d}S, \\ &= -\iiint_V \nabla p \mathrm{d}V, \end{aligned} \tag{2.5}$$

where $\mathbf{F}$ is the force vector acting on the particle, S is the surface enclosing the particle, p is the pressure at a given point and $\hat{\mathbf{n}}$ is the unit vector normal to the surface element $\mathrm{d}S$. In the second line, we have applied Gauss' theorem to relate the integral over the surface S to an integral over the particle volume V.

According to Netwon's second law, a net force on the particle will result in a change of particle velocity. In the reference frame of the particle, this can be expressed as

$$\rho \frac{\mathrm{d}\mathbf{v}}{\mathrm{d}t} = -\nabla p, \tag{2.6}$$

where ρ is the density of the medium and $\mathbf{v}$ is the particle velocity. The integral signs are dropped as we consider the infinitesimal particle.

The expression given by (2.6) is valid only in the inertial frame of the infinitesimal particle. More useful would be an equation which is valid for a fixed coordinate system (defined, say, by the container of some liquid). To transform (2.6) into one which describes a fixed

[1] Much of the content of this and the following section is adapted from [6].

point in space relative to the walls of some container (as opposed to one relative to a particular moving particle within it), it is necessary to consider how any property of that particle would change as it moves. The expression which gives the change in velocity due to change in position d$\mathbf{r}$ over time dt is given by

$$\frac{\partial \mathbf{v}}{\partial x}\mathrm{d}x + \frac{\partial \mathbf{v}}{\partial y}\mathrm{d}y + \frac{\partial \mathbf{v}}{\partial z}\mathrm{d}z \equiv (d\mathbf{r}\cdot\nabla)\mathbf{v}, \tag{2.7}$$

which is known as the *convective part*. Therefore, to transform (2.6) into the frame of the container, we substitute the time derivative on the left-hand-side of (2.6) for

$$\frac{\mathrm{d}\mathbf{v}}{\mathrm{d}t} \longrightarrow \frac{\partial \mathbf{v}}{\partial t} + (\mathbf{v}\cdot\nabla)\mathbf{v}, \tag{2.8}$$

therefore arriving at Euler's equation of motion for an ideal fluid:

$$\rho\left[\frac{\partial \mathbf{v}}{\partial t} + (\mathbf{v}\cdot\nabla)\mathbf{v}\right] = -\nabla p. \tag{2.9}$$

Euler's equation of motion is essentially just Newton's second law generalised to work for fluids. It omits the terms needed to describe viscous forces. These can be added in to (2.6) using a second-rank viscosity stress tensor τ, yielding

$$\rho\frac{\mathrm{d}\mathbf{v}}{\mathrm{d}t} = -\nabla p - \nabla\cdot\tau. \tag{2.10}$$

Transforming back into the container frame, and accounting for the symmetries in τ, we arrive at the Navier-Stokes equation:

$$\rho\left[\frac{\partial \mathbf{v}}{\partial t} + (\mathbf{v}\cdot\nabla)\mathbf{v}\right] = -\nabla p + \left(\mu_B + \frac{1}{3}\mu\right)\nabla(\nabla\cdot\mathbf{v}) + \mu\nabla^2\mathbf{v}, \tag{2.11}$$

where μ and μ_B are the shear and bulk viscosities of the fluid respec-

tively. Like any vector field, we can decompose the velocity vector $\mathbf{v}$ into two parts: one with zero divergence $\mathbf{v_T}$, and one with zero curl $\mathbf{v_L} = 0$. This allows us to split the Navier Stokes equation (2.11) into two parts, one which describes longitudinal waves:

$$\rho_0 \frac{\partial \mathbf{v_L}}{\partial t} = -\nabla p + \left(\mu_B + \frac{4}{3}\mu\right) \nabla^2 \mathbf{v_L}, \tag{2.12}$$

and another which describes shear waves:

$$\rho_0 \frac{\partial \mathbf{v_T}}{\partial t} = -\mu \nabla \times \nabla \times \mathbf{v_T}. \tag{2.13}$$

Since sound propagation in fluids and human tissue is dominated by longitudinal waves, these are used in general-purpose imaging. Therefore we will concentrate our attention on the longitudinal part of the Navier-Stokes equation, (2.12).

To obtain a second-order partial differential equation which is homogeneous in the small-signal regime with zero viscosity (the sort which yields wave-like solutions), we need two further equations: one for conservation of matter—the continuity equation; and another which relates pressure and density thermodynamically—the equation of state.

The continuity equation can be derived by considering the change in density of a specified volume V of fluid and relating it to the flow of matter through the surface S that encloses it. Hence we can write down:

$$\frac{\partial}{\partial t}\left[\iiint_V \rho \mathrm{d}V\right] = -\left[\iint_S \rho \mathbf{v} \cdot \hat{\mathbf{n}} \mathrm{d}S\right]. \tag{2.14}$$

Applying Gauss's theorem and considering an arbitrarily small volume, we arrive at

$$\frac{\partial \rho}{\partial t} + \nabla \cdot (\rho \mathbf{v}), \tag{2.15}$$

which is the continuity equation in the frame of the fluid container.

The last equation relates the thermodynamic quantities of pressure and density (though these quantities are present in (2.9), it relates the spatial derivative of pressure and includes velocity terms), knowns as the equation of state. In the particle frame, this can be written as

$$\kappa \rho_0 \frac{\mathrm{d}p}{\mathrm{d}t} = \frac{\mathrm{d}\rho}{\mathrm{d}t}, \tag{2.16}$$

where κ is the adiabatic compressibility. Transforming into the frame of the container, we obtain

$$\frac{\partial \rho}{\partial t} + \mathbf{v} \cdot (\nabla \rho) = \kappa \rho_0 \left[\frac{\partial p}{\partial t} + \mathbf{v} \cdot (\nabla p) \right]. \tag{2.17}$$

To obtain a linear wave equation, we consider small perturbations of the equilibrium fluid pressure p_0 and density ρ_0, with those perturbations denoted p_1 and ρ_1 respectively. It can be shown [6] that linearity holds as long as $|p_1| \ll \rho_0 c_0^2$ where c_0 is the fluid speed of sound. For water, this means that $|p_1| \ll 1.5\,\mathrm{MPa}$. By substituting $\rho = \rho_0 + \rho_1$ into the continuity equation (2.15) and ignoring higher-order terms, we obtain

$$\frac{\partial \rho_1}{\partial t} + \rho_0 \nabla \cdot \mathbf{v} \simeq 0. \tag{2.18}$$

Likewise, for the equation of state (2.17), substituting $\rho = \rho_0 + \rho_1$ and $p = p_0 + p_1$, removing higher-order terms and substituting (2.18), we obtain

$$\kappa \frac{\partial p_1}{\partial t} + \nabla \cdot \mathbf{v} \simeq 0. \tag{2.19}$$

Now, by taking the time derivative of the longitudinal Navier-

Stokes equation (2.12) and substituting the pressure term for $-\nabla \cdot \mathbf{v}/\kappa$ from (2.19) and simplifying (using the fact that $\nabla \times \mathbf{v_L} = 0$), we obtain

$$\kappa\rho_0 \frac{\partial^2 \mathbf{v_L}}{\partial t^2} = \nabla^2 \mathbf{v_L} + \kappa \left(\mu_B + \frac{4}{3}\mu\right) \frac{\partial}{\partial t}\left(\nabla^2 \mathbf{v_L}\right). \tag{2.20}$$

Finally, by defining a velocity potential ϕ such that $\nabla\phi = -\mathbf{v_L}$, we obtain a scalar wave equation:

$$\kappa\rho_0 \frac{\partial^2 \phi}{\partial t^2} = \nabla^2 \phi + \kappa \left(\mu_B + \frac{4}{3}\mu\right) \frac{\partial}{\partial t}\left(\nabla^2 \phi\right). \tag{2.21}$$

For an inviscid fluid ($\mu = \mu_B = 0$), the wave equation simplifies to

$$\nabla^2 \phi - \frac{1}{c_0^2} \frac{\partial^2 \phi}{\partial t^2} = 0, \tag{2.22}$$

where $c_0 = 1/\sqrt{\kappa\rho_0}$ is the speed of sound.

2.2.2 Non-linear Ultrasound

We noted in the previous section that for pressures above around 1.5 MPa in water, the assumption of linearity no longer holds. This is evident from the non-linearised Navier-Stokes equation (2.11). A model which can account for non-linear effects but which is still amenable to computation can be found by Taylor-expanding a generalised equation of state $p(\rho, s)$ where s is entropy up to second-order terms in ρ and first-order term in s [28]:

$$\mathrm{d}p = \left(\frac{\partial p}{\partial \rho}\right)_s \mathrm{d}\rho + \frac{1}{2}\left(\frac{\partial^2 p}{\partial \rho^2}\right)_s (\mathrm{d}\rho)^2 + \left(\frac{\partial p}{\partial s}\right)_\rho \mathrm{d}s. \tag{2.23}$$

From our earlier first-order equation of state (2.17), which excluded any entropy terms due to the assumptions of small perturba-

tions being adiabatic and reversible, we can integrate with respect to t over a small time interval over which the spatial gradients of ρ and p are assumed to be constant:

$$\rho + \mathbf{r} \cdot (\nabla \rho) = \kappa \rho_0 (p + \mathbf{r} \cdot (\nabla p)), \tag{2.24}$$

where $\mathbf{r}$ is the particle displacement vector. Assuming that the medium starts off in thermodynamic equilibrium such that $\nabla p = \nabla \rho = 0$ and taking the partial derivative with respect to ρ at constant s, we find that

$$\left(\frac{\partial p}{\partial \rho}\right)_s = \frac{1}{\kappa \rho_0} = c_0^2, \tag{2.25}$$

where we note that c_0 is the linear speed of sound.

This allows us to parameterise (2.23) using constants A, and B, given by

$$\begin{aligned} A &\equiv \rho_0 \left(\frac{\partial p}{\partial \rho}\right)_s = \rho_0 c_0^2 \\ B &\equiv \rho_0 \left(\frac{\partial^2 p}{\partial \rho^2}\right)_s, \end{aligned} \tag{2.26}$$

leading to a form of the equation of state (2.23) in the container frame with parameterised non-linear terms:

$$p = c_0^2(\rho + \mathbf{r} \cdot \nabla \rho_0) + \frac{B}{2A}\frac{c_0^2}{\rho_0}\left(\rho^2 + (\mathbf{r} \cdot \nabla \rho_0)\right)^2 + 2\rho \mathbf{r} \cdot \nabla \rho_0 - c_0 L \rho, \tag{2.27}$$

where we have substituted the entropy term for a generalised operator L defined as

$$-c_0^2 L\rho \equiv \left(\frac{\partial p}{\partial s}\right)_\rho s. \tag{2.28}$$

In this equation, the first term is the usual linear relationship be-

tween pressure and density. The second term, parametirised by the ratio B/A, effects a change in sound speed depending on amplitude. The final term, which must be treated as an arbitrarily-defined operator which acts on ρ, represents the energy loss. Both the ratio A/B and the loss operator are generally determined phenomenologically. The loss operator can be defined as a fractional Laplacian to have solutions which obey power-law absorption of the form

$$\alpha = \alpha_0 \omega^y, \tag{2.29}$$

where α is the attenuation constant and α_0, ω and y are absorption parameters which can be related to the operator L.

2.2.3 Imaging: Holography, Sonar and Synthetic Apertures

An ideal ultrasound image would be one which perfectly maps the acoustic impedance of each point within a 2D plane with infinite resolution. This gives the clinician information about the structure of tissue and outlines of organs, as different tissue have different bulk acoustic properties, allowing the boundaries between them to be seen. In fact, a truly ideal system would reveal not only the relative acoustic impedances for longitudinal acoustic waves at a single frequency, but the bulk and shear moduli measured over a wide range of frequencies, allowing highly detailed tissue categorisation.

The simplest way to form an image is to successively measure the reflected ultrasound power from all points over the plane of interest. To do this, we can either deposit ultrasound energy to each single point and measure the reflected power, or deposit energy over the whole plane and filter out the energy which is reflected from regions other than the point of interest. As we have seen in the previous section, an ultrasound pulse can be represented by

$$A(t-\Delta t)\exp\left[i(\omega t+\phi)\right], \tag{2.30}$$

where A is the pulse envelope function, Δt is the pulse time offset, $\omega = 2\pi\nu$ is the ultrasound frequency and ϕ is the phase offset.

In general, Δt and ϕ can be controlled for both pulse transmission and in reception (ie, using post-processing). A and ω tend to be characteristics of the transducer used (see §2.3.2). In our ideal imaging system, we want to measure the proportion of ultrasound power reflected from each point $\{(x',y')\}$ within the plane. To do this, we can set up an array of ultrasound sources such that[2]

$$\sum_i P_i(x,y)A(t-\Delta t_i)\exp\left[i(kr_i+\phi_i)\right] \simeq \delta(x-x',y-y')A'(t)e^{i\phi_0}+h(x,y,z;t), \tag{2.31}$$

where we are summing over sources i and P_i is the spatial apodisation of each source (element), δ is the Dirac delta function, ϕ_0 is an overall constant phase term, $A'(t)$ is the time-delayed pulse at the focal point, $k = 2\pi\nu/c$ where ν is the sound frequency and c is the speed of sound, $h(x,y,z;t)$ is the residual energy not at the focal point and

$$r_i = \sqrt{(x-x_i')^2+(y-y_i')^2}, \tag{2.32}$$

where $\{x_i', y_i'\}$ are the centres of each element. In the above we have assumed that each source or receiver element $P(x,y)$ is small in extent compared to the wavelength, which allows us to treat them as point sources.

The practice of finding the set of times $\{\Delta t_i\}$ and phase delays $\{\phi_i\}$ to satisfy (2.31) whilst minimising $h(x,y,z;t)$ is known as beam-

[2]For simplicity we have neglected diffraction effects of the elements themselves and treated them as point-source-like.

forming. We can simplify this problem somewhat by observing that the time delay Δt can be represented instead by virtually moving each ultrasound element in the direction towards the target—ie $P_{i'}(x,y) = P_i(x-\Delta x, y-\Delta y)$ where

$$\begin{aligned} \Delta x &= \frac{(x'-x_i)}{(y'-y_i)} \cdot c\Delta t_i, \\ \Delta y &= \frac{(y'-y_i)}{(x'-x_i)} \cdot c\Delta t_i, \end{aligned} \tag{2.33}$$

x_i and y_i are the centres of element i (in other words, the point at which $P(x,y)$ is maximum) and c is the speed of sound.[3] Therefore we can rewrite (2.31) as

$$\sum_{i'} P_{i'}(x,y)A(t)e^{ikr_{i'}} \simeq \delta(x-x', y-y')A'(t)e^{i\phi_0} + h(x,y,z;t). \tag{2.34}$$

The problem of beamforming is now reduced to finding the set of complex functions $P_{i'}(x,y)$ which minimise $\int |h(x,y,z)| \mathrm{d}x\mathrm{d}y\mathrm{d}z$.

In the way we originally formulated this problem, $A'(t)$ is already known (or rather, we didn't care much what it was), and we wanted to find the set of functions $P_{i'}(x,y)$ which satisfy (2.34). We were concentrating the energy emitted from the transducers to a point $\{x', y'\}$—in other words, focusing. However, there is nothing in (2.34) which implies we cannot view the problem in reverse: say we measure the values of Δt_i, ϕ_i and $A(t)$. Since we already know the fixed element positions $\{x_i', y_i'\}$ and their apodisation $\{P_i(x,y)\}$, we therefore know $P_{i'}(x,y)A(t)$ of (2.34). However, instead of there being a single point $\delta(x-x', y-y')$ of concentrated ultrasound energy, we now imagine that the scene has been 'flooded' with ultrasound waves of frequency

[3] There should also be a small correction to account for the r^2 change in wave amplitude as sources move towards/away from the point (x_i, y_i), but we omit this for the sake of simplicity.

v. In this scenario, (2.34) becomes

$$\sum_{i'} T_{i'}[P_{i'}](x,y)A(t)e^{ikr_{i'}} \simeq \delta(x-x',y-y')A'(t)e^{i\phi_0} + H(x,y,z;t), \tag{2.35}$$

where $H(x,y,z;t)$ is some arbitrary complex-valued function. Now our goal is to come up with a set of transformations $\{T_{i'}\}$ which can act on $P_{i'}$ to minimise $\int |H(x,y,z)|\mathrm{d}x\mathrm{d}y\mathrm{d}z$.

Both (2.34) and (2.35) express optimisation problems related to forming ultrasound images. In (2.34), we are focusing ultrasound energy to a point (x',y'). In (2.35), we are filtering all signals except for those which originate from the point (x',y'). Both of these operations are now termed beamforming, with the only difference between them being whether the ultrasound is focused in emission or reception [29]. Equation (2.35) corresponds to what used to be termed 'acoustic holography', as it involves the capture of the amplitude and phase of a wavefront over an aperture and subsequent filtering to reconstruct an image. Instead of an optical aperture, which diffracts the incoming light and thereby forms an image from the Fourier transform of the wavefront, this aperture instead captures the wavefront intact and does the image reconstruction computationally (or using analogue delay and sum circuitry)—hence the name, 'synthetic aperture'. Equation (2.34) corresponds to a practice which has its roots in phased-array radar and sonar: it was discovered that a beam could be deflected using fixed equally-spaced transmitters by simply modifying the phase of the excitation of each transmitter. When it became possible to make ultrasound transducer arrays with small enough pitch such that it approached the wavelength of high-frequency ultrasound, these arrays started being used for B-mode imaging. This is often referred to in the literature to as 'phased-array' ultrasound.

As we discussed in §2.1.2, high ultrasound intensities can lead to tissue heating and mechanical ablation. Safe ultrasound imaging depends on keeping the peak ultrasound intensities to safe levels. Where these safe levels lie is specified by two quantities: the thermal index (TI) and mechanical index, which are calculated dynamically based on acoustic power, tissue type and ultrasound frequency [30]. For the case of transmission beamforming, the total energy deposited into the tissue is simply the sum of the energy at the focal point $\int |A'(t)|^2 \mathrm{d}t$ and the energy deposited into the image background $\int |h(x,y,z)|^2 \mathrm{d}x\mathrm{d}y\mathrm{d}z$. On the other hand, for receive beamforming, the total energy deposited into the system is the sum of the un-transformed excitation from each transducer: $\sum_{i'} |P_{i'}(x,y)A(t)e^{ikr_{i'}}|^2$. This means that, assuming maximally-optimised beamforming, increasing the signal to noise ratio (SNR) in the transmission beamforming case requires an increase in the peak intensity, and increasing the SNR in the receive beamforming case requires an increase in the total energy deposited into the system.

It is possible to form ultrasound images without having to pay any attention to beamforming. This can be done when the imaging depth is less than d^2/λ, where d is the element pitch (or for a single element system the element size) and λ is the wavelength. As the distance or wavelength increases, the propagated pulse becomes too diffracted, so beamforming must be used [31]. This is a particular issue in deep tissue imaging, as along with an increase in d, lower frequencies (and therefore longer wavelength λ) are used since they are less attenuated.

One of the most important parameters for an imaging system is resolution. In B-mode ultrasound systems this comes in two flavours: axial and transverse. Transverse resolution is the more familiar type from optical imaging. Axial refers to the ability to resolve the difference in depth between two objects. It is straightforward to see that

axial resolution must depend on the length of the transmitted pulses: two objects which lie on the same axis can only be distinguished if the pulses reflected from them arrive back at the transducer can be distinguished in the time domain. The longer the pulses (and therefore the narrower the bandwidth), the further apart the two points have to be to allow them to be distinguished.

The transverse resolution can be derived by considering the steady-state ($A(t) \to 1$) focusing problem in either (2.34) or (2.35). If we replace the summation over the transducers with an integral, and consider instead of discrete transducers at $x = 0$ with a continuum of variable phase represented by the complex phasor $\Phi(y)$ and constant amplitude, the left-hand side of (2.34) becomes

$$\int \Phi(y) e^{ikr} \mathrm{d}y, \tag{2.36}$$

which is the Fourier transform of the phasor $\Phi(y)$. Therefore to find the phase function over the transducer continuum, we need to inverse Fourier-transform our target, which we take as a perfect reflector positioned at $y = 0, x = x'$ with a width of D (2.34):

$$\Phi(y) = \frac{1}{2\pi} \int_{\infty}^{\infty} \mathrm{rect}[(x - x')/D] \mathrm{rect}[y/D] e^{-ikr} \mathrm{d}k. \tag{2.37}$$

To simplify, we assume that $x' \gg y'$, therefore $r \simeq x'$, and $k \simeq k_x$ (ie, the transverse-propagating wave components are lost, which is the far-field approximation). And since we only care about lateral resolution, we can drop the requirement for axial focusing and replace $\mathrm{rect}[(x - x')/d]$ with 1. Therefore our 'optimal' phase function is given by

$$\Phi(y) = 2\pi \,\mathrm{sinc}\left(\frac{Dy}{\lambda r}\right). \tag{2.38}$$

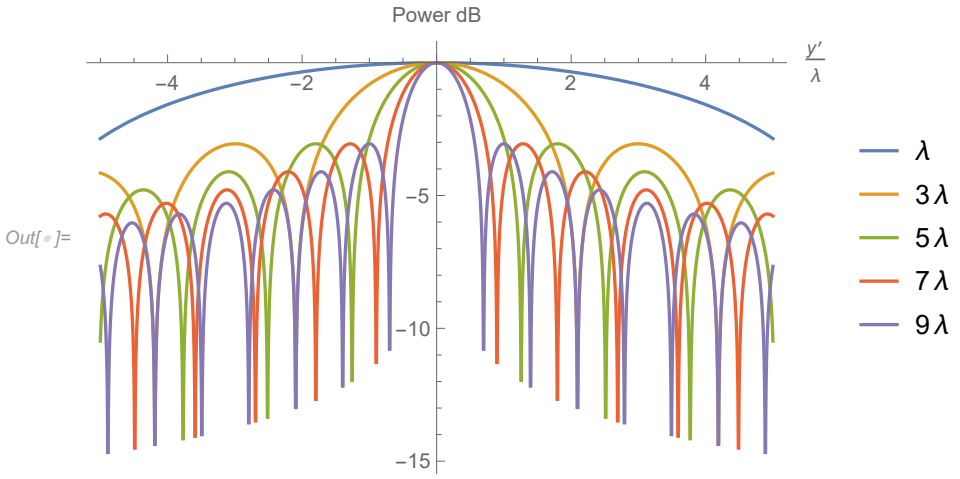

Figure 2.2: Plot of the lateral focal regions for set of apertures of length $L = n\lambda$.

This phase function can either represent the phase of the elements in transmission to focus the ultrasound energy to a spot, or the phase delays required to filter out signals originating from outside the focal zone.

In reality, the integral in (2.36) ought to have had limits, since our transducer array (or aperture) will always be finite in extent. If our array has length L, then the *actual* focal region at the plane of interest at infinity (in other words, $r \gg D$, the far-field approximation) will be given by

$$\lim_{r\to\infty} \int_{-L/2}^{+L/2} \operatorname{sinc}\left(\frac{Dy}{\lambda r}\right) e^{iy\cdot y'} \mathrm{d}y = L \operatorname{sinc}\left(\frac{y'L}{2}\right). \tag{2.39}$$

Figure 2.2 shows the normalised focal regions for various values of L given in multiples of λ. We observe that, in the far-field, increasing L makes it possible to make the focal spot arbitrarily small, but that this requires an impractically large aperture. Given a fixed geometry, the simplest way to increase resolution is to decrease λ.

2.2.3.1 Inhomogeneities

So far we have set up our problem assuming a homogeneous medium. Of course, if the medium really were acoustically homogeneous, we would not gain much by imaging it with ultrasound. The inhomogeneity, or turbidity, of the medium can cause the assumptions of (2.34) and (2.35) to break down: implicit in these formulations is the assumption that the phase velocity of the sound is constant. In particular, focusing through dense media such as bone means that the propagator e^{ikr} must be broken up into multiple propagators $e^{ik_1r_1}, e^{ik_2r_2}, \ldots, e^{ik_nr_n}$ to derive the correct expression [32].

2.3 Ultrasound Materials and Devices

As we saw in Chapter 1, there is a wide variety of ways for linearly converting an acoustic signal into an electrical one. For ultrasound, the best technique to date has been the use of piezoelectric materials, particularly piezo-ceramics such as lead zirconate titanate (PZT), as transducers made from these exhibit remarkably efficient conversion between acoustic and electrical energy. The downside of these materials is their lead content (leading to issues with disposal), their high acoustic impedance (meaning they require one or more carefully-tuned matching layers to couple to low-acoustic impedance media such as water of human tissue), and difficulty of integrating them into foundry processes such as CMOS.

Nonetheless, the performance advantage of piezo-ceramics has meant that they have remained dominant since their discovery in the 1950s [33]. In this section we examine the mechanism of the piezoelectric effect, issues around transducer design, and look at the emerging technologies which are starting to displace piezo-ceramics in certain contexts. This lays the groundwork for the following chapter, in which we introduce MOUR, a concept which allows us to build low-

cost ultrasound sensor with a flat frequency response in the MHz range from off-the-shelf components. This, coupled with a single ultrasound source and synthetic aperture beamforming discussed in §2.2.3, could herald a new way of building ultrasound imaging probes, one which does not rely on lead-based materials and which can be made using processes compatible with existing consumer electronics production capacity.

2.3.1 The Piezoelectric Effect

The piezoelectric effect is the means by which, in certain materials, an electric field can induce a strain and vice versa. There are four quantities—two mechanical, two electric—which can be related to each other: stress $[T]$, strain $[S]$, electric field $[E]$ and electric displacement $[D]$. To fully describe the piezoelectric effect, it is only necessary to relate either two of the mechanical quantities to either two of the electric quantities, in addition to the conventional relationships between stress-strain and electric field-displacement field. Therefore, four equivalent equations can be written down describing each of the piezoelectric and inverse piezoelectric effects, giving eight equations in total. To describe an arbitrary effect it is necessary to parameterise these equations with second-rank tensors. In all, this leads to 12 second-rank tensors, from which only four are needed to fully characterise the transducer material. The full list of equations and relationships between the tensors can be found in [6, pp. 340-341]. Here we reproduce two of these equations (sufficient to fully characterise ultrasound transducer material excluding mechanical and resistive losses):

$$[T] = [c^E][S] - [e]^t[E],$$
$$[D] = [e][S] + [\varepsilon^S][E],$$

where $[c]$ is the stiffness matrix (ie, a tensor representation of Young's modulus), $[e]$ is the piezoelectric stress matrix, and $[\varepsilon]$ is the electric permittivity of the material. The superscripts on $[c^E]$ and $[\varepsilon^S]$ respectively denote that these are quantities measured at constant electric field and strain respectively. The t superscript denotes the transpose operation.

A useful scalar and dimensionless quantity can be derived from the various tensors. This quantity is defined by the square root of the ratio between the electrical/mechanical work done and the mechanical/electrical energy stored for an ideal transducer under certain boundary conditions. This quantity is termed k, and is by convention defined as pertaining to a transducer aligned along the 33 axis of the material (ie, the electrical contacts and forces are made over the planes defined by the 3-axis). In later sections, we will make use of the constant k_t, where the subscript t indicates that the coupling factor is measured whilst clamped (constant lateral strain):[4]

$$k_t = \frac{e_{33}}{\sqrt{c_{33}^D \varepsilon_{33}^S}}. \tag{2.41}$$

2.3.2 Transducer Design

Choice of material is just one aspect of ultrasound transducer design. Like any device, each transducer is designed with a set of design goals which must be reached via trade-offs in performance in various dimensions. Transducers have three main dimensions by which performance is measured: bandwidth, sensitivity and operating frequency. Disregarding system noise, all three of these performance dimensions can be expressed by a single matrix: the transfer matrix. A transfer matrix

[4] Unlike the notation in (2.40), t does not indicate constant stress but the set of boundary conditions whereby the lateral (1- and 2-axis) strain, as opposed to the lateral stress, is zero. This is generally easier to measure directly.

simply relates the energy flows for a multi-port system to one another, usually as a function of frequency. Since MOURs, the subject of the present work, are purely ultrasound receivers (hydrophones), we are only interested in comparing their performance to conventional transducers operating in receive-mode. This means that much of the literature, which tends to characterise transducer performance in terms of pulse-echo performance, for which insertion loss S_{11} is the most important parameter, does not lend itself to direct comparison with the present work. Fortunately, it is just as simple to calculate receiver performance as it is to calculate pulse-echo performance, since the model used is identical.[5]

A general transducer system has two ports, one electrical and one mechanical/acoustic. The relationship between energy flowing in and out of each port can be described by a 2×2 matrix given by

$$\begin{pmatrix} V_{\text{out}} \\ V_{\text{in}} \end{pmatrix} = \begin{pmatrix} T_{11} & T_{12} \\ T_{21} & T_{22} \end{pmatrix} \begin{pmatrix} F_{\text{in}} \\ F_{\text{out}} \end{pmatrix}, \tag{2.42}$$

where V and F represent electrical and mechanical power flows in and out of the system respectively and T_{ij} are the components of the transfer matrix. In SI units, the transfer matrix is in units of volts-per-newton. T_{11} divided by the surface area of the transducer gives the receiver sensitivity in units of volts-per-pascal.

T_{11} can be calculated in the frequency domain using a linear circuit model. These calculations were used in a paper under review [34] on the subject of software-defined transducers (SDTs), to which we

[5] In fact, the correct figure of merit (FOM) for an ultrasound receiver is the noise equivalent pressure (NEP), which we define and estimate in the experimental section. Although NEP is generally quoted for hydrophones and ultrasound calibration equipment, it is not generally used to characterise pulse-echo transducers. The assertion that the FOM for a pulse-echo transducer is its insertion loss S_{11} relies on the assumption that the transducer and imaging domain can be treated as a linear system, which is generally not the case. This was one of the major difficulties I faced when attempting to benchmark MOURs against comparable devices.

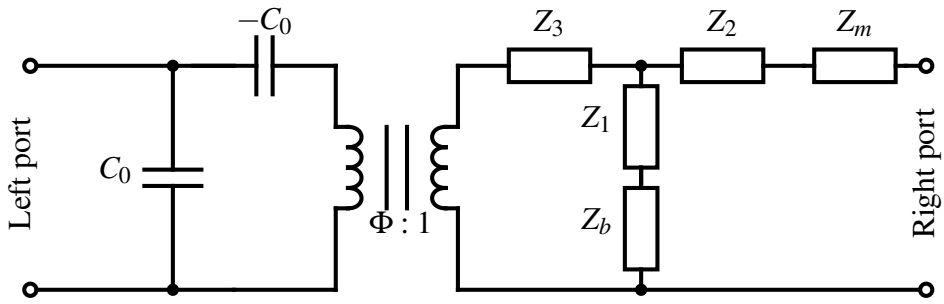

Figure 2.3: Mason's 1D model of an electroacoustic transducer

dedicate a later chapter of the thesis.

Figure 2.3 shows Mason's 1D model of a simple transducer assembly in receive mode [36]. Acoustic energy is incident on the right-hand port, transformed into electrical energy by the transformer, and emitted from the left-hand port. The T-junction of acoustic impedances Z_1, Z_2 and Z_3 represent an acoustic transmission line made of the transducer material. Z_b and Z_m represent the acoustic impedances of the transducer backing and the medium respectively, both assumed to be infinite in extent [37]. The values of all the variables are given in Table 2.1.

Figure 2.4 shows the transfer functions T_{21} of three types of transducer in receive mode, found by computing the cascade matrix for the linear circuit in Figure 2.3 [38]. The computation was performed by symbolically multiplying the cascading matrices whose parameters were found using the KLM model as described in [6] and [38][7]. Since the matrix multiplications were done symbolically, the final numerical

[6]For the hard-backed PVDF transducer, the resonance occurs at $l = \lambda/4$ [35], therefore for the calculation which yielded Figure 2.4, the thickness of the PVDF device is set to half that of the two PZT devices.

[7]I discovered in the process of doing these calculations that there are quite a few errors, typos and contradictions in the literature regarding the linear transducer model. A paper by Whitworth et al. [39] discusses this in depth, but even this paper I found to be self-contradictory. In the end, the equations from Oakley et al. [38] gave the expected results.

Table 2.1: Variables for Mason's Model [6]

Variable	Description	Value
Z_1, Z_2	Transmission line acoustic impedances	$iAZ_t \tan(l/2\lambda)$
Z_3		$-iAZ_t \csc(l/\lambda)$
Z_t	Transducer material acoustic impedance	PZT: 33.7 MRayl
		PVDF: 3.9 MRayl
Z_m	Medium acoustic impedance	Water: 1.479 MRayl
Z_b	Backing acoustic impedance	Hard: ∞MRayl
		Matched: Z_t
		Air: $\sim$0 MRayl
A	Transducer area	5 cm^2
l	Transducer thickness[6]	$\pi c/\omega_0$
λ	Wavelength	$2\pi c/\omega$
ω	Frequency	—
ω_0	Unloaded resonant frequency	10 MHz
Φ	Transformer turns ratio	$\sqrt{\varepsilon^s/\rho_0}/(C_0 k_t c)$
C_0	Transducer capacitance	$A\varepsilon^s/l$
c	Speed of sound	PZT: 4350 m/s
		PVDF: 2200 m/s
ρ_0	Density	PZT: 7750 $\mathrm{kg/m}^3$
		PVDF: 1780 $\mathrm{kg/m}^3$
ε^s	Relative electric permittivity (un-clamped)	PZT: 1780
		PVDF: 6
k_t	Piezo coupling factor (clamped)	PZT: 0.49
		PVDF: 0.2

calculation could be made using a single analytic expression, meaning a wide range of frequencies could be calculated very fast. *Mathematica* was used for both of these steps.

The calculations were performed assuming a 50 Ω load at the left-

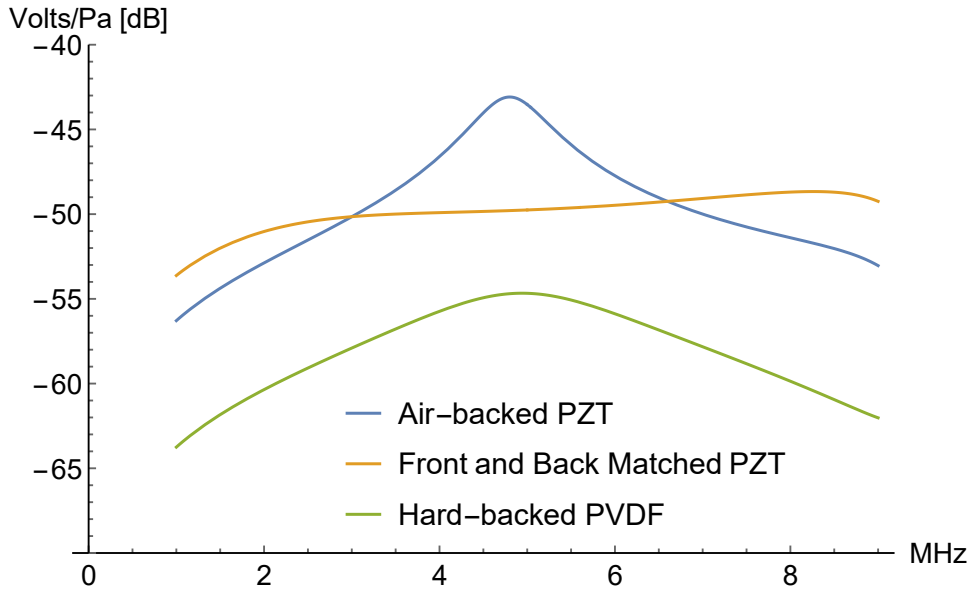

Figure 2.4: Voltage resoponse for three different types of transducer referenced to 1 V/Pa

hand port in Figure 2.3. We observe that the air-backed transducer results in the highest peak sensitivity for all three transducers, but at the expense of bandwidth. On the other hand, the PVDF-based transducer has a flat frequency response across a wide frequency range, but is less sensitive overall. Wideband response whilst retaining high sensitivity can be obtained by adding front and back matching layers to the PZT transducer: the orange line in Figure 2.4 shows the response for a PZT transducer with an effectively infinitely thick PZT backing and a single quarter-wave front matching layer. Multiple matching layers can be added to further widen the response, and the PZT layer can be made thinner, such that ω_0 is far above the frequency range of interest. However, due to the complexity of machining and bonding thin layers of PZT, PVDF hydrophones are generally preferred over PZT for wideband hydrophone applications, the sensitivity of which can be enhanced by electrical impedance matching [35].

This simple comparison demonstrates the fundamental trade-off in using piezoelectric materials for building ultrasound receivers. High

bandwidth and operating frequencies are possible, but require thin slabs of piezoelectric material and, in the case of hard ceramics like PZT, matching layer(s). Alternatively, piezopolymers such as PVDF which can be deposited in thin layers quite trivially (PVDF-TrFE, a block co-polymer of PVDF, cures naturally into a β-like phase which exhibits piezoelectric properties [40]) are well matched to biological media, and closer matching can be achieved using similarly easily deposited matching layers. But PVDF transducers have far worse peak sensitivity compared to PZT transducers, making them generally unsuitable for pulse-echo applications. The difficulties in machining PZT into thin slabs and the incompatibility of lead-based materials with foundry processes such as CMOS have put paid to the possibility of a low-cost integrated PZT-based transducer-on-a-chip—generally, a bonding step is always required [41]. On the other hand, PVDF-based ultrasound-on-a-chip is already commercially mass-produced and used in smartphones as fingerprint sensors [42, 43]. Generally, though, the sensitivity of PVDF is simply not high enough for deep tissue biomedical imaging. This is why there has been interest of late in moving beyond piezoelectrics for ultrasound imaging.

2.3.3 Beyond Piezoelectrics

In §2.1, we outlined several emerging areas of ultrasound applications which will push transducer requirements beyond what is currently possible within current mass-market transducer technology. The simplest way we can summarise this break with conventional thought on transducers is a move away from the insertion loss, the conventional parameter for pulse-echo performance, as being the most important factor in transducer design. For non-linear, harmonic, elastographic, or therapeutic ultrasound, we cannot rely on the assumption that only the frequencies in a narrow band around the transducer resonance will be

of interest.

MOUR, described in the following chapters, fits into this new paradigm. However, before introducing it, we will briefly review two recent technologies which have also challenged the dominance of piezoelectric transducers in certain applications. The first, optical systems, offers unprecedented sensitivity and can have very wide operating bandwidths [44]. The second, MEMS, promises unprecedented integration by allowing transducers and their analogue and digital back-ends to be fabricated on a single integrated platform. This is particularly important for 3D ultrasound, where creating interconnects between a CMOS back-end and a ceramic piezoelectric layer remains challenging. Our invention, MOUR, combines the advantageous features of both optical systems and MEMS.

2.3.3.1 Optical Systems

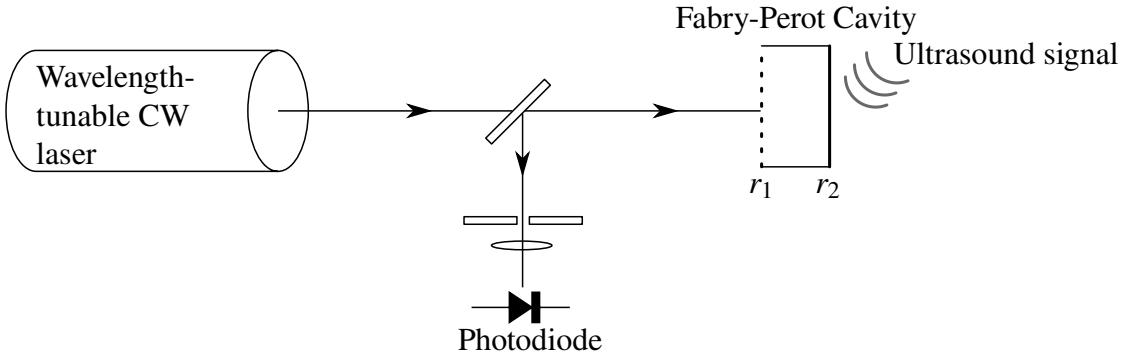

Figure 2.5: Detection scheme for a Fabry-Perot optical hydrophone

Instead of detecting changes in the intrinsic properties of some material, a cavity-based device uses resonance effects which are highly sensitive to changes in the boundary conditions of the system. For an optical system [45–48], the length of Fabry-Perot cavity sandwiched between one full and one half mirror is modulated by an impinging ultrasound wave, and detected by a photodiode. This is shown in Figure 2.5.

The signal detected at the photodiode is given by

$$I_0 = I_1 + I_2 + 2\sqrt{I_1 I_2}\cos\Phi, \tag{2.43}$$

where I_0, I_1 and I_2 are the total intensity, the intensity reflected from the near side and far side of the cavity respectively. Φ is the phase difference due to the different path lengths of the near and far sides of the cavity. When ultrasound impinges on the sensor, Φ comprises a static and small time-varying phase term:

$$\Phi = \phi + d\phi. \tag{2.44}$$

The sensor operates with highest sensitivity and linearity at the quadrature point of (2.43) where $\phi = (2m+1)\pi/2$ (where m is some integer). Regardless, there will always be a dc photocurrent in the photodiode due to the I_1 and I_2 terms in (2.43). The amplitude of the signal term in (2.43) can be increased by increasing the power of the CW laser, but only up until the point where the photodiode is saturated by the dc intensity.

A further source of noise is beam walk-off: the beam which enters the Fabry-Perot cavity has a slight divergence, and this is enough to add spurious out-of-phase signals and degrade the SNR. More sophisticated cavity structures have been explored to counteract this [47, 49].

The ultrasound-induced strain applied to the cavity in Figure 2.5 varies the optical path length in two ways: by changing the length of the cavity, and by changing the refractive index n of the cavity. While it is obvious how strain affects a change in length, the change in n relies on the strain-optic effect, which is generally quite weak [50]. The effect can be enhanced by increasing the field confinement in the sensitive region, hence increasing the Q-factor of the resonator.

We can do this by looking beyond dielectric resonators and in-

stead consider metal nanostructures [51]. At optical frequencies, it is possible to couple p-polarised light in a material with a low, positive dielectric constant ε_1 to oscillations of conduction electrons in a metal with a large, negative ε_2 [52]. These oscillations are termed surface plasmon polaritons (SPP), and non-resonant configurations involving sub-wavelength patterning of gold have already been demonstrated to detect ultrasound [53]. Alternatively, when one or more of the dimensions of the nanostructure approaches the wavelength of the incident light, the SPPs are reflected at either end of the particle and, when on resonance, create a standing wave analogous to those in a dielectric Fabry-Perot cavity [51]. In this way we can create structures which work similarly to RF antennas, but with slightly different resonance conditions [54]. Such an antenna could be fabricated on the tip of an optical fibre, and ultrasound detected by sum and difference signals generated by SPP-enhanced Brillouin light scattering [55].

Finally, a third class of sensor exploits the high n sensitivity of whispering gallery modes (WGM) in dielectric ring resonators. These sensors can be manufactured by direct laser writing (DLW) techniques [56] or standard CMOS lithography [57] and use evanescent coupling from waveguides to excite WGMs.

Some of the benefits of using all-optical devices include avoidance of RF interference with other devices, MRI compatibility, elimination of cross-talk between transducers within an array, robustness and potential low-cost[8] [45, 58–60]. Optics, however, brings with it its own set of complications: while Fabry-Perot transducers make excellent single-pixel ultrasound sensors, building a synthetic aperture to perform imaging requires manual raster scanning of either the interrogation beam [61, 62], or, in the photoacoustic case, the excitation beam

[8]For *in-vivo* clinical applications low cost is especially important, as devices may have to be disposed of after each use for hygene reasons.

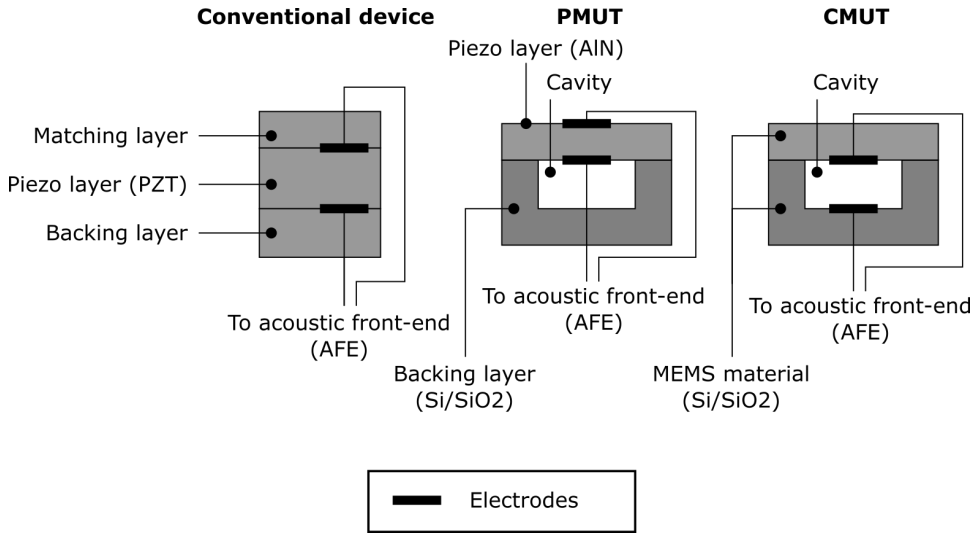

Figure 2.6: Comparison of the structure of conventional PZT transducers, PMUTs, and CMUTs

[47, 63]. The speed at which images can be captured will therefore always be limited, particularly over wide areas, and make video-rate 4D imaging (including time dimension) near impossible. Compressed sensing techniques can speed up acquisition times to some degree, but at the expense of resolution [64, 65]. This issue could be mitigated using multiple simultaneous beams, but the optical powers required make this cost-prohibitive.

2.3.3.2 Micro Electro-Mechanical Systems (MEMS)

The appeal of MEMS, generally, is the ability to fabricate mechanical sensors using techniques which have been refined through the development of CMOS electronics. In doing this, many of the benefits inherent to microelectronics are carried over to the fabrication of accelerometers, gyroscopes, microphones and other devices. In the late 1990s it became natural to ask whether these techniques might be applicable to ultrasound transducers. In accordance with the typical multi-decade development cycle for MEMS devices, we are only now seeing our first examples of mass-produced arrays of MEMS transducers [66].

There are two major category of MEMS transducer: capaci-

tive micromachined ultrasound transducers (CMUT) and piezo micromachined ultrasound transducers (PMUT). In either case, MEMS foundry processes are used to create a 3D structure whose essential feature is a microscopic cavity (typically either air or vacuum filled). For CMUT devices, one side of the cavity is connected to the ground and the other to a voltage. In CMUTs, the transduction effect comes purely from the electrostatic force between the two plates. The cavity can be deformed by biasing one of the plates, and deformation can be measured by detecting the change in voltage between them. The small size of the cavity ensures that the capacitance of the device is high enough to allow a strong coupling between mechanical and electrical modulations.

For PMUTs, the design is slightly different [67]. Instead of the cavity being between the two electrodes, the cavity sits behind a piezoelectric material sandwiched between the electrodes. In this way the device resembles an air-backed PZT device, only a weaker foundry-compatible piezomaterial such as aluminium nitride (AlN) is used instead of PZT. The advantage of this technique is that the piezo layer can be made very thin and act as a membrane rather than a simple compression transducer, increasing the sensitivity. The structure of these different devices can be seen in Figure 2.6.

Because these devices have complex membrane dynamics, they are much more difficult to model and tend to be more non-linear than conventional PZT transducers. They also suffer from yield issues due to the complexity of the process (most MEMS packages feature one or two devices per die. CMUTs and PMUTs contain thousands). In the case of CMUT, the need to bias the plates at all times during operation can cause charge leakage and therefore higher power consumption than PZT transducers, and also result in overheating issues (for a medical device designed to be in direct contact with human skin this can be a

serious problem).

Nonetheless, experience shows that MEMS technology, despite its long development cycles, has a habit of gradually addressing the performance disparity between it and legacy technologies and eventually exceeding them. One handicap we do see as being permanent for MEMS is the large volumes needed to make them economical: unlike for an ASIC, which can be made from building-blocks which have well-understood processes, each MEMS product currently needs to be designed at the package level, meaning that ultrasound systems designers are likely to have only a small number of CMUT or PMUT packages to choose from. This could make it difficult for CMUT and PMUT devices to meet the needs of specialist, low-volume applications.

References

[1] J. W. S. Rayleigh. “Theory of Sound, Volume 1 (2nd Edition Revised and Enlarged)”. In: (1877). issn: 978-0-486-60292-9. url: https://app.knovel.com/hotlink/toc/id:kpTSVERE04/theory-sound-volume-1/theory-sound-volume-1.

[2] James Clerk Maxwell. *A Treatise on Electricity and Magnetism*. Clarendon Press, 1873. 616 pp. Google Books: 92QSAAAAIAAJ.

[3] K. Kirk Shung. “Diagnostic Ultrasound: Imaging and Blood Flow Measurements”. In: (2015).

[4] Nebojsa Duric et al. “Detection of Breast Cancer with Ultrasound Tomography: First Results with the Computed Ultrasound Risk Evaluation (CURE) Prototype: Detection of Breast Cancer with Ultrasound Tomography”. In: *Medical Physics* 34.2 (Jan. 30, 2007), pp. 773–785. issn: 00942405. doi: 10.1118/1.2432161. url: http://doi.wiley.com/10.1118/1.2432161 (visited on 01/06/2019).

[5] Morten Thingemann Bøtker et al. “The Role of Point of Care Ultrasound in Prehospital Critical Care: A Systematic Review”. In: *Scandinavian Journal of Trauma, Resuscitation and Emergency Medicine* 26.1 (June 26, 2018), p. 51. issn: 1757-7241. doi: 10.1186/s13049-018-0518-x. url: https://doi.org/10.1186/s13049-018-0518-x (visited on 01/02/2019).

[6] Richard S. C. Cobbold. *Foundations of Biomedical Ultrasound*. Oxford University Press, Sept. 7, 2006. 844 pp. isbn: 978-0-19-977512-5. Google Books: Hwb5D60vb5IC.

[7] Dipen N. Sinha and John F. Brady. “Acoustic Camera”. U.S. pat. 10054676B2. Los Alamos National Security LLC. Aug. 21, 2018. url: https://patents.google.com/patent/US10054676B2/en (visited on 06/19/2019).

[8] D. Cosgrove et al. “EFSUMB Guidelines and Recommendations on the Clinical Use of Ultrasound Elastography.Part 2: Clinical Applications”. In: *Ultraschall in der Medizin - European Journal of Ultrasound* 34.3 (June 2013), pp. 238–253. issn: 0172-4614, 1438-8782. doi: 10.1055/s-0033-1335375. url: http://www.thieme-connect.de/DOI/DOI?10.1055/s-0033-1335375 (visited on 10/29/2019).

[9] Liang Sang et al. “Accuracy of Shear Wave Elastography for the Diagnosis of Prostate Cancer: A Meta-Analysis”. In: *Scientific Reports* 7.1 (May 16, 2017), pp. 1–8. issn: 2045-2322. doi: 10.1038/s41598-017-02187-0. url: https://www.nature.com/articles/s41598-017-02187-0 (visited on 10/17/2019).

[10] Urszula Zaleska-Dorobisz et al. “Ultrasound Elastography – Review of Techniques and Its Clinical Applications”. In: *Advances in Clinical and Experimental Medicine* 23 (2014), pp. 645–655. issn: 1899-5276. doi: 10.17219/acem/26301. url: http://www.advances.am.wroc.pl/strona.php?id=11&n=1665&lang=en (visited on 10/17/2019).

[11] Kevin J. Parker et al. “A Unified View of Imaging the Elastic Properties of Tissue”. In: *The Journal of the Acoustical Society of America* 117.5 (May 2005), pp. 2705–2712. issn: 0001-4966. doi: 10.1121/1.1880772. url: http://asa.scitation.org/doi/10.1121/1.1880772 (visited on 10/17/2019).

[12] Kathy Nightingale. “Acoustic Radiation Force Impulse (ARFI) Imaging: A Review”. In: *Current Medical Imaging Reviews* 7.4 (Nov. 1, 2011), pp. 328–339. issn: 15734056. doi: 10.2174/157340511798038657. url: http://www.eurekaselect.com/openurl/content.php?genre=article&issn=1573-4056&volume=7&issue=4&spage=328 (visited on 10/01/2019).

[13] Armen Sarvazyan et al. “An Overview of Elastography-An Emerging Branch of Medical Imaging”. In: *Current Medical Imaging Reviews* 7.4 (Nov. 1, 2011), pp. 255–282. issn: 15734056. doi: 10.2174/157340511798038684. url: http://www.eurekaselect.com/openurl/content.php?genre=article&issn=1573-4056&volume=7&issue=4&spage=255 (visited on 10/23/2019).

[14] Armen P Sarvazyan et al. “Shear Wave Elasticity Imaging: A New Ultrasonic Technology of Medical Diagnostics”. In: *Ultrasound in Medicine & Biology* 24.9 (Dec. 1, 1998), pp. 1419–1435. issn: 0301-5629. doi: 10.1016/S0301-5629(98)00110-0. url: http://www.sciencedirect.com/science/article/pii/S0301562998001100 (visited on 10/17/2019).

[15] G. ter Haar. *The Safe Use of Ultrasound in Medical Diagnosis*. London: British Institute of Radiology, 2012. url: http://www.birpublications.

org/pb/assets/raw/Books/SUoU_3rdEd/Safe_Use_of_Ultrasound.pdf (visited on 10/22/2019).

[16] Kerry G. Baker, Valma J. Robertson, and Francis A. Duck. "A Review of Therapeutic Ultrasound: Biophysical Effects". In: *Physical Therapy* 81.7 (July 1, 2001), pp. 1351–1358. issn: 0031-9023, 1538-6724. pmid: 11444998. url: http://ptjournal.apta.org/content/81/7/1351 (visited on 10/04/2016).

[17] Jennet Conant. *Tuxedo Park : A Wall Street Tycoon and the Secret Palace of Science That Changed the Course of World War II*. New York; London: Simon & Schuster, May 6, 2003. 352 pp. isbn: 978-0-684-87288-9.

[18] K. F. Graff. "Ultrasonics: Historical Aspects". In: *1977 Ultrasonics Symposium*. 1977 Ultrasonics Symposium. Oct. 1977, pp. 1–10. doi: 10.1109/ULTSYM.1977.196782.

[19] Dr >Gail ter Haar and Constantin Coussios. "High Intensity Focused Ultrasound: Physical Principles and Devices". In: *International Journal of Hyperthermia* 23.2 (Jan. 1, 2007), pp. 89–104. issn: 0265-6736. doi: 10.1080/02656730601186138. pmid: 17578335. url: https://doi.org/10.1080/02656730601186138 (visited on 10/23/2019).

[20] Jordan J. Markham, Robert T. Beyer, and R. B. Lindsay. "Absorption of Sound in Fluids". In: *Reviews of Modern Physics* 23.4 (Oct. 1, 1951), pp. 353–411. issn: 0034-6861. doi: 10.1103/RevModPhys.23.353. url: https://link.aps.org/doi/10.1103/RevModPhys.23.353 (visited on 03/26/2019).

[21] W. J. Fry et al. "Physical Factors Involved in Ultrasonically Induced Changes in Living Systems: I. Identification of Non-Temperature Effects". In: *The Journal of the Acoustical Society of America* 22.6 (Nov. 1, 1950), pp. 867–876. issn: 0001-4966. doi: 10.1121/1.1906707. url: https://asa.scitation.org/doi/abs/10.1121/1.1906707 (visited on 10/31/2019).

[22] M. R. Bailey et al. "Physical Mechanisms of the Therapeutic Effect of Ultrasound (a Review)". In: *Acoustical Physics* 49.4 (July 2003), pp. 369–388. issn: 1063-7710, 1562-6865. doi: 10.1134/1.1591291. url: http://link.springer.com/10.1134/1.1591291 (visited on 10/30/2019).

[23] Kullervo Hynynen and Ryan M. Jones. "Image-Guided Ultrasound Phased Arrays Are a Disruptive Technology for Non-Invasive Therapy". In: *Physics in Medicine and Biology* 61.17 (Aug. 2016), R206–R248. issn: 0031-9155.

doi: 10.1088/0031-9155/61/17/R206. url: https://doi.org/10.1088%2F0031-9155%2F61%2F17%2Fr206 (visited on 04/02/2019).

[24] William O'Brien and Floyd Dunn. "History of High Intensity Focused Ultrasound, Bill and Frank Fry and the Bioacoustics Research Laboratory". In: *The Journal of the Acoustical Society of America* 136.4 (Oct. 1, 2014), pp. 2219–2220. issn: 0001-4966. doi: 10.1121/1.4900058. url: https://asa.scitation.org/doi/abs/10.1121/1.4900058 (visited on 03/25/2019).

[25] M. Gyöngy and C. Coussios. "Passive Spatial Mapping of Inertial Cavitation During HIFU Exposure". In: *IEEE Transactions on Biomedical Engineering* 57.1 (Jan. 2010), pp. 48–56. issn: 0018-9294. doi: 10.1109/TBME.2009.2026907.

[26] Constantin C. Coussios et al. "Mapping and Characterization of Cavitation Activity". U.S. pat. 9238152B2. Oxford University Innovation Ltd. Jan. 19, 2016. url: https://patents.google.com/patent/US9238152B2/en?inventor=Constantin+Coussios&assignee=oxsonics (visited on 05/09/2019).

[27] Qinghua Huang and Zhaozheng Zeng. "A Review on Real-Time 3D Ultrasound Imaging Technology". In: *BioMed Research International* (2017). doi: 10.1155/2017/6027029. url: https://www.hindawi.com/journals/bmri/2017/6027029/ (visited on 04/04/2018).

[28] Bradley E. Treeby et al. "Modeling Nonlinear Ultrasound Propagation in Heterogeneous Media with Power Law Absorption Using a K-Space Pseudospectral Method". In: *The Journal of the Acoustical Society of America* 131.6 (June 2012), pp. 4324–4336. issn: 1520-8524. doi: 10.1121/1.4712021. pmid: 22712907.

[29] P. N. Keating. "Acoustical Holography — A Comparison with Phased Array Sonar". In: *Acoustical Holography: Volume 5*. Ed. by Philip S. Green. Boston, MA: Springer US, 1974, pp. 231–237. isbn: 978-1-4757-0827-1. doi: 10.1007/978-1-4757-0827-1_14. url: https://doi.org/10.1007/978-1-4757-0827-1_14 (visited on 04/01/2019).

[30] Francis A. Duck. "Medical and Non-Medical Protection Standards for Ultrasound and Infrasound". In: *Progress in Biophysics and Molecular Biology*. Effects of Ultrasound and Infrasound Relevant to Human Health 93.1 (Jan. 1, 2007), pp. 176–191. issn: 0079-6107. doi: 10.1016/j.pbiomolbio.2006.

07.008. url: http://www.sciencedirect.com/science/article/pii/S0079610706000885 (visited on 12/03/2019).

[31] A. Macovski. "Ultrasonic Imaging Using Arrays". In: *Proceedings of the IEEE* 67.4 (Apr. 1979), pp. 484–495. issn: 1558-2256. doi: 10.1109/PROC.1979.11278.

[32] B. T. Cox and P. C. Beard. "Fast Calculation of Pulsed Photoacoustic Fields in Fluids Using K-Space Methods". In: *The Journal of the Acoustical Society of America* 117.6 (June 1, 2005), pp. 3616–3627. issn: 0001-4966. doi: 10.1121/1.1920227. url: http://scitation.aip.org/content/asa/journal/jasa/117/6/10.1121/1.1920227 (visited on 11/20/2015).

[33] D. Fasquelle, M. Mascot, and J. C. Carru. "On the Research of Lead-Free Material Challengers for PZT Replacement". In: *Solid-State Electronics* 75 (Sept. 1, 2012), pp. 6–12. issn: 0038-1101. doi: 10.1016/j.sse.2012.04.031. url: http://www.sciencedirect.com/science/article/pii/S0038110112001098 (visited on 06/10/2019).

[34] Tom S Robbins, Erwin J Alles, and Cyril C Renaud. "Software-Defined Transducers for Low-Cost and Versatile Ultrasound Imaging". In: *submitted* (2019).

[35] L. F. Brown. "Design Considerations for Piezoelectric Polymer Ultrasound Transducers". In: *IEEE Transactions on Ultrasonics, Ferroelectrics, and Frequency Control* 47.6 (Nov. 2000), pp. 1377–1396. issn: 0885-3010. doi: 10.1109/58.883527.

[36] Warren P. Mason. *Physical Acoustics: Principles and Methods*. Academic Press, Oct. 22, 2013. 532 pp. isbn: 978-1-4832-7439-3. Google Books: LtE3BQAAQBAJ.

[37] G. Kossoff. "The Effects of Backing and Matching on the Performance of Piezoelectric Ceramic Transducers". In: *IEEE Transactions on Sonics and Ultrasonics* 13.1 (Mar. 1966), pp. 20–30. issn: 0018-9537. doi: 10.1109/T-SU.1966.29370.

[38] C. G. Oakley. "Calculation of Ultrasonic Transducer Signal-to-Noise Ratios Using the KLM Model". In: *IEEE Transactions on Ultrasonics, Ferroelectrics, and Frequency Control* 44.5 (Sept. 1997), pp. 1018–1026. doi: 10.1109/58.655627.

[39] G. Whitworth. “Discussion of 1-D Piezoelectric Transducer Models with Loss”. In: *IEEE Transactions on Ultrasonics, Ferroelectrics, and Frequency Control* 48.3 (May 2001), pp. 844–846. issn: 0885-3010, 1525-8955. doi: 10.1109/58.920720.

[40] P. E. Bloomfield, Wei-Jung Lo, and P. A. Lewin. “Experimental Study of the Acoustical Properties of Polymers Utilized to Construct PVDF Ultrasonic Transducers and the Acousto-Electric Properties of PVDF and P(VDF/TrFE) Films”. In: *IEEE Transactions on Ultrasonics, Ferroelectrics, and Frequency Control* 47.6 (Nov. 2000), pp. 1397–1405. issn: 0885-3010. doi: 10.1109/58.883528.

[41] Robert S. Lasser and David C. Rich. “Image Sensor for Large Area Ultrasound Mapping”. U.S. pat. 20150369909A1. Imperium Inc. Dec. 24, 2015. url: https://patents.google.com/patent/US20150369909A1/en?assignee=Imperium%2c+Inc.&page=2 (visited on 06/18/2019).

[42] John K. Schneider and Jack C. Kitchens. “Hydrophone Array Module”. U.S. pat. 7436736B2. Ultra-Scan Corp. Oct. 14, 2008. url: https://patents.google.com/patent/US7436736B2/en (visited on 07/10/2019).

[43] John K. Schneider, Jack C. Kitchens, and James T. Baker. “Ultrasonic Fingerprint Scanning Utilizing a Plane Wave”. U.S. pat. 7739912B2. Ultra-Scan Corp. June 22, 2010. url: https://patents.google.com/patent/US7739912B2/en (visited on 07/10/2019).

[44] P. C. Beard, F. Perennes, and T. N. Mills. “Transduction Mechanisms of the Fabry-Perot Polymer Film Sensing Concept for Wideband Ultrasound Detection”. In: *IEEE Transactions on Ultrasonics, Ferroelectrics, and Frequency Control* 46.6 (Nov. 1999), pp. 1575–1582. issn: 0885-3010. doi: 10.1109/58.808883.

[45] P. C. Beard and T. N. Mills. “Miniature Optical Fibre Ultrasonic Hydrophone Using a Fabry-Perot Polymer Film Interferometer”. In: *Electronics Letters* 33.9 (Apr. 1997), pp. 801–803. issn: 0013-5194. doi: 10.1049/el:19970545.

[46] P. C. Beard et al. “Optical Fiber Photoacoustic–Photothermal Probe”. In: *Optics Letters* 23.15 (Aug. 1, 1998), pp. 1235–1237. issn: 1539-4794. doi: 10.1364/OL.23.001235. url: https://www.osapublishing.org/abstract.cfm?uri=ol-23-15-1235 (visited on 12/15/2017).

[47] James A. Guggenheim et al. “Ultrasensitive Plano-Concave Optical Microresonators for Ultrasound Sensing”. In: *Nature Photonics* 11.11 (Oct. 31, 2017), p. 714. issn: 1749-4893. doi: 10.1038/s41566-017-0027-x. url: https://www.nature.com/articles/s41566-017-0027-x (visited on 11/03/2017).

[48] Jing Li et al. “Highly Sensitive Optical Microresonator Sensors for Photoacoustic Imaging”. In: vol. 8943. 2014, pp. 89430C-89430C–10. doi: 10.1117/12.2037015. url: http://dx.doi.org/10.1117/12.2037015 (visited on 12/13/2016).

[49] Supriya V. Thathachary, Cameron Motameni, and Shai Ashkenazi. “An All-Optical Fiber-Optic Photoacoustic Transducer”. In: *Optical Fibers and Sensors for Medical Diagnostics and Treatment Applications XVIII*. Optical Fibers and Sensors for Medical Diagnostics and Treatment Applications XVIII. Vol. 10488. International Society for Optics and Photonics, Feb. 13, 2018, p. 104880M. doi: 10.1117/12.2289198. url: https://www.spiedigitallibrary.org/conference-proceedings-of-spie/10488/104880M/An-all-optical-fiber-optic-photoacoustic-transducer/10.1117/12.2289198.short (visited on 03/05/2018).

[50] T. A. Davis and K. Vedam. “Pressure Dependence of the Refractive Indices of the Tetragonal Crystals: ADP, KDP, CaMoO 4, CaWO 4, and Rutile”. In: *JOSA* 58.11 (1968), pp. 1446–1451.

[51] Jon A. Schuller et al. “Plasmonics for Extreme Light Concentration and Manipulation”. In: *Nature Materials* 9.3 (Mar. 2010), pp. 193–204. issn: 1476-4660. doi: 10.1038/nmat2630. url: https://www.nature.com/articles/nmat2630 (visited on 03/13/2018).

[52] Lukas Novotny and Bert Hecht. *Principles of Nano-Optics*. 2 edition. Cambridge: Cambridge University Press, Sept. 6, 2012. 578 pp. isbn: 978-1-107-00546-4.

[53] Vladislav V. Yakovlev et al. “Ultrasensitive Non-Resonant Detection of Ultrasound with Plasmonic Metamaterials”. In: *Advanced Materials* 25.16 (Apr. 24, 2013), pp. 2351–2356. issn: 1521-4095. doi: 10.1002/adma.201300314. url: http://onlinelibrary.wiley.com/doi/10.1002/adma.201300314/abstract (visited on 11/07/2016).

[54] Lukas Novotny and Niek van Hulst. “Antennas for Light”. In: *Nature Photonics* 5.2 (Feb. 2011), pp. 83–90. issn: 1749-4893. doi: 10.1038/nphoton.2010.237. url: https://www.nature.com/articles/nphoton.2010.237 (visited on 03/05/2018).

[55] Ivan S. Maksymov and Andrew D. Greentree. “Plasmonic Nanoantenna Hydrophones”. In: *Scientific Reports* 6 (Sept. 9, 2016), srep32892. issn: 2045-2322. doi: 10.1038/srep32892. url: https://www.nature.com/articles/srep32892 (visited on 07/25/2017).

[56] Heming Wei and Sridhar Krishnaswamy. “Polymer Micro-Ring Resonator Integrated with a Fiber Ring Laser for Ultrasound Detection”. In: *Optics Letters* 42.13 (July 1, 2017), pp. 2655–2658. issn: 1539-4794. doi: 10.1364/OL.42.002655. url: https://www.osapublishing.org/abstract.cfm?uri=ol-42-13-2655 (visited on 09/26/2017).

[57] Senlin Zhang, Jian Chen, and Sailing He. “Novel Ultrasound Detector Based on Small Slot Micro-Ring Resonator with Ultrahigh Q Factor”. In: *Optics Communications* 382 (Jan. 2017), pp. 113–118. issn: 00304018. doi: 10.1016/j.optcom.2016.07.082. url: http://linkinghub.elsevier.com/retrieve/pii/S003040181630671X (visited on 03/14/2018).

[58] P. C. Beard et al. “Comparison of a Miniature, Ultrasonic, Optical Fibre Hydrophone with PVDF Hydrophone Technology”. In: *1998 IEEE Ultrasonics Symposium. Proceedings (Cat. No. 98CH36102)*. 1998 IEEE Ultrasonics Symposium. Proceedings (Cat. No. 98CH36102). Vol. 2. 1998, 1881–1884 vol.2. doi: 10.1109/ULTSYM.1998.765319.

[59] Edward Z. Zhang and Paul C. Beard. “A Miniature All-Optical Photoacoustic Imaging Probe”. In: ed. by Alexander A. Oraevsky and Lihong V. Wang. Feb. 10, 2011, 78991F. doi: 10.1117/12.874883. url: http://proceedings.spiedigitallibrary.org/proceeding.aspx?doi=10.1117/12.874883 (visited on 07/27/2017).

[60] Sacha Noimark et al. “Carbon-Nanotube-PDMS Composite Coatings on Optical Fibers for All-Optical Ultrasound Imaging”. In: *Advanced Functional Materials* (Sept. 2016). issn: 1616301X. doi: 10.1002/adfm.201601337. url: http://doi.wiley.com/10.1002/adfm.201601337 (visited on 10/27/2016).

[61] R. Ansari et al. “All-Optical Endoscopic Probe for High Resolution 3D Photoacoustic Tomography”. In: *Photons Plus Ultrasound: Imaging and Sensing 2017*. Photons Plus Ultrasound: Imaging and Sensing 2017. Vol. 10064. International Society for Optics and Photonics, Mar. 23, 2017, 100641W. doi: 10.1117/12.2250617. url: https://www.spiedigitallibrary.org/conference-proceedings-of-spie/10064/100641W/All-optical-endoscopic-probe-for-high-resolution-3D-photoacoustic-tomography/10.1117/12.2250617.short (visited on 03/14/2018).

[62] Olumide Ogunlade et al. “In Vivo 3-Dimensional Photoacoustic Imaging of the Renal Vasculature in Preclinical Rodent Models”. In: *American Journal of Physiology-Renal Physiology* (Dec. 20, 2017). issn: 1931-857X. doi: 10.1152/ajprenal.00337.2017. url: https://www.physiology.org/doi/abs/10.1152/ajprenal.00337.2017 (visited on 03/14/2018).

[63] Thomas J. Allen et al. “Large Area Laser Scanning Optical Resolution Photoacoustic Microscopy Using a Fibre Optic Sensor”. In: *Biomedical Optics Express* 9.2 (Feb. 1, 2018), pp. 650–660. issn: 2156-7085. doi: 10.1364/BOE.9.000650. url: https://www.osapublishing.org/boe/abstract.cfm?uri=boe-9-2-650 (visited on 03/14/2018).

[64] Erwin J. Alles et al. “A Reconfigurable All-Optical Ultrasound Transducer Array for 3D Endoscopic Imaging”. In: *Scientific Reports* 7 (Apr. 26, 2017), p. 1208. issn: 2045-2322. doi: 10.1038/s41598-017-01375-2.

[65] M. M. Betcke et al. “Acoustic Wave Field Reconstruction From Compressed Measurements With Application in Photoacoustic Tomography”. In: *IEEE Transactions on Computational Imaging* 3.4 (Dec. 2017), pp. 710–721. doi: 10.1109/TCI.2017.2706029.

[66] Kevin Brenner et al. “Advances in Capacitive Micromachined Ultrasonic Transducers”. In: *Micromachines* 10.2 (Feb. 2019), p. 152. doi: 10.3390/mi10020152. url: https://www.mdpi.com/2072-666X/10/2/152 (visited on 03/12/2019).

[67] Stefon Shelton et al. “CMOS-Compatible AlN Piezoelectric Micromachined Ultrasonic Transducers”. In: *2009 IEEE International Ultrasonics Symposium*. 2009 IEEE International Ultrasonics Symposium. Sept. 2009, pp. 402–405. doi: 10.1109/ULTSYM.2009.5441602.

Chapter 3

The Principle of Microwave Oscillator Ultrasound Receivers

We introduce in this chapter the concept of a microwave oscillator ultrasound receiver (MOUR) and describe the theoretical underpinnings. The basic concept is to create a device which causes a high-frequency carrier wave to be modulated by a lower-frequency sound wave. An example of this is the Fabry-Perot optical cavity seen in the previous section. The concept, however, has its historical roots in carrying human-audible sound over radio-frequency electromagnetic waves. The first audible radio broadcast was 'an impromptu program of Christmas music and readings' in 1906 which used an early CW radio frequency carrier of around 10 kHz and was picked up by fishing boats equipped with radio telegraph equipment [1]. The advance which made it possible to carry audible sound as opposed to just on-off keying was the development of sufficiently low-noise carriers (early RF 'signal' generators used high frequency intermittent sparks).

Early radio broadcast systems would use resistive microphones (such as the carbon microphone) to modulate the carrier amplitude. Once the signal had been broadcast, however, there was no way to modulate the free-space electromagnetic wave without first receiving it with an antenna. In the 1950s, the Soviet Union wanted a way to

Figure 3.1: *The Thing*, a Soviet listening device installed in the US embassy in Moscow. It was hidden behind a carved wooden plaque of the Great Seal of the United States, which was presented as a gift to the US ambassador. Photos by Austin Mills [CC BY-SA 2.0 (https://creativecommons.org/licenses/by-sa/2.0)]

transmit speech from inside the US embassy in Moscow to a listening post across the road without having to install any active circuit, which would need its own power source and could be detected, inside the embassy. The spying device they came up with (invented by Léon Therimin, who also invented the eponymous musical instrument) was a small electromagnetic cavity resonator hidden behind a large wall ornament presented to the US ambassador by a delegation of Soviet schoolchildren. The electomagnetic cavity had a diagphram so that the cavity resonant frequency would be modulated by human speech. By focussing a beam of microwaves at the building (and ensuring to do so only occasionaly so as to reduce the chance of detection), the Soviets could listen in to confidential conversations within the embassy by detecting and amplifying the envelope of the reflected signal [2].

Our devices operate on essentially the same principle: a microwave carrier is passed through a resonator near the resonant frequency. When sound impinges on the resonator, the boundary conditions change, and this results in a carrier modulation. The ultrasound signal is carried on the sidebands of the microwave signal, and can be read out using a variety of techniques, the most basic of which is

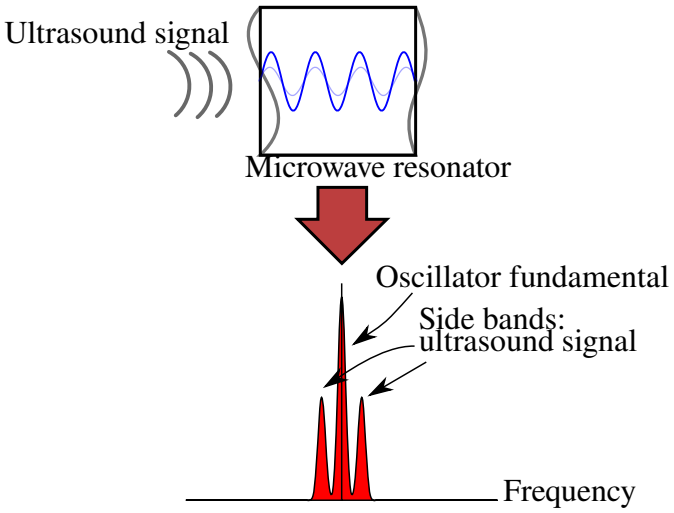

Figure 3.2: Illustration of the principle of MOUR. An incoming sound wave modulates the boundary conditions of a microwave resonator, resulting in the ultrasound signal being carried on the sidebands.

simple envelope detection. In the following sections we go over the concept of this device in detail, starting from some basic observations around the use of electromagnetic waves to carry sound waves whilst preserving spatial information. We then briefly look at the theory of electromagnetic resonators, and how they can be constructed using a planar arrangement of conductors and dielectric. After that we consider the effect of covering a microstrip antenna with thin layers of dielectric, well known to engineers installing outdoor antennae which must be weather-proofed, but only tentatively explored in the context of mechanical sensors. Finally, we look at one of the immediate consequences of using this technique for detecting ultrasound: the ability to multiplex spatial ultrasound information into the frequency domain of the carrier.

3.1 Photons and Phonons

A very basic fact of nature is that light travels faster than sound. A consequence of this is that, in a non-dispersive medium, the wavelength of light compared to the wavelength of sound at the same frequency is

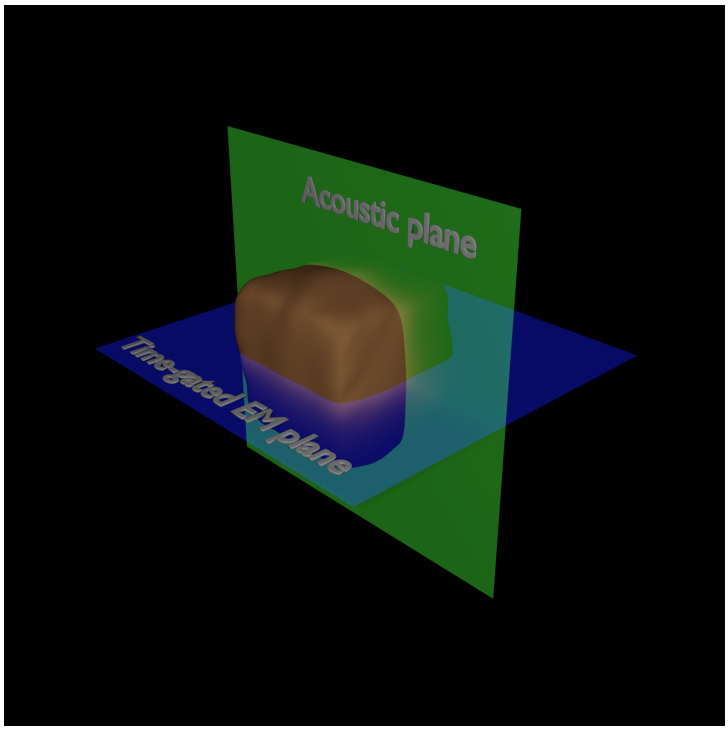

Figure 3.3: The zeugmatographic principle using acoustic and electromagnetic waves. Either the acoustic field is inhomogeneous (ie, focused), which is the subject of the patent [3], or EM RF field is inhomogeneous, which is the subject of this work. The EM plane can be moved vertically by changing the time-gating.

between four and five orders of magnitude higher. If the maximum frequency of vibration for ultrasound travelling in water is 10 MHz, then the corresponding frequency of free-space electromagnetic waves with the same wavelength is around 300 GHz.

We will prove in §3.1.1 that if we were to use free-space microwaves to measure ultrasound in a similar manner to laser vibrometry, the diffraction limit would severely limit the achievable spatial resolution. This limitation is rarely, if ever, considered for optical systems, since the 'effective transducer size' as determined by the laser diffraction pattern, is comfortably below the acoustic Nyquist sampling wavelength [4]. It would be of little use to create a comparable beam scanning system using microwaves to form ultrasound images, as you would be diffraction limited by the microwave beam rather than

the ultrasound. In fact, one of the great advantages of ultrasound is its short wavelength, enabling high resolution imaging.

Free-space RF can, of course, be used for imaging, but it requires a second inhomogeneous field in order to resolve spectral properties of small volumes within the sample. The principle of joining together two fields in order to beat the diffraction limit of either one is known as zeugmatography, and its most famous example is in magnetic resonance imaging (MRI) [5]. But the concept is more general than that: we know that fluctuations in density can modulate the refractive index of a material, which is the principle behind acousto-optic modulators [6]. The vibrations of an object under ultrasound insonification may be detected by a modulation of an RF or microwave signal through it. By spectrally filtering around the sum and difference frequencies of the microwave and ultrasound, the electromagnetic reflectivity or absorption can be read out. Now imagine that an ultrasound pulse is used, instead of a CW wave. The microwave signals can now be time-gated according to the desired z-elevation slice which we wish to image. If the ultrasound source and microwave antenna are placed perpendicularly to one another, and the ultrasound source focuses the ultrasound to a thin plane, then a full cross-sectional image of the microwave absorption properties of the medium can be read out with a resolution determined by the ultrasound wavelength (see Figure 3.3) [3].

In our work, instead of a homogeneous electromagnetic field and an inhomogeneous ultrasound field, we propose a system involving an inhomogeneous microwave field and a quasi-homogeneous ultrasound field. The inhomogeneity of the microwave field allows us to measure the ultrasound field in a region smaller than the Nyquist wavelength of the ultrasound field. This, in effect, allows us to do plane-wave imaging using a single ultrasound source, a single microwave oscillator/detector pair connected to an array of resonators, and no other

active components. How we achieve this inhomogeneous microwave field is the subject of the following section. In fact, it is not simply the inhomogeneity of the microwave field itself which enables this technique, but also the dielectric structure which interacts with the microwave evanescent field.

In practice, it can be simpler (and still quite economical) to use separate oscillator/detector pairs for each ultrasound channel, though we see this as an implementation detail.

3.1.1 Spatial Sampling

A heterogeneous electromagnetic field in free space can be written as a superposition of plane waves with frequency ω. For practical reasons, there must always be a maximum cut-off frequency either in the fields we have generated or that we can detect. We call this frequency ω_c. In free space, the dispersion relation between ω and the wavenumber k is $k = \omega/c$ where c is the wave speed. The cut-off wavenumber is therefore given by ω_c/c, meaning that the spatial distribution of the field is given by

$$E'(x,y,z) = \frac{1}{\sqrt{2\pi}} \iiint_{-\omega_c/c}^{\omega_c/c} \tilde{E}(k_x,k_y,k_z) \exp\left[i(xk_x + yk_y + zk_z)\right] \mathrm{d}k_x \mathrm{d}k_y \mathrm{d}k_z, \tag{3.1}$$

where $\tilde{E}$ is the un-truncated Fourier-transformed field.

Lemma. *Under free-space conditions, zeugmatographic imaging is diffraction-limited by the field with the fastest propagation speed.*

Proof. We can re-write the right-hand-side of (3.1) as a convolution between the original un-truncated field E and a sinc function:

$$E'(x) = \sqrt{\frac{2}{\pi}} \operatorname{sinc}\left(\frac{\omega_c x}{4c}\right) * E(x), \tag{3.2}$$

where for the sake of clarity we have dropped the y and z dimensions.

Now consider two objects which interact with the acoustic field and have point spread functions (PSF) given by

$$\begin{aligned} &\operatorname{sinc}\left(\frac{\bar{\omega}_c x}{4\bar{c}} - \frac{\Delta}{2}\right) \quad \text{Object 1} \\ &\operatorname{sinc}\left(\frac{\bar{\omega}_c x}{4\bar{c}} + \frac{\Delta}{2}\right) \quad \text{Object 2} \end{aligned} \tag{3.3}$$

where the barred symbols $\bar{\omega}_c$ and $\bar{c}$ represent the highest frequency and speed respectively of waves in the acoustic field, and Δ is their separation. The $E(x)$ field is therefore the sum of the two PSFs. From (3.2),

$$\begin{aligned} \sqrt{\frac{\pi}{2}} E'(x) &= \operatorname{sinc}\left(\frac{\omega_c x}{4c}\right) * \left[\operatorname{sinc}\left(\frac{\bar{\omega}_c x}{4\bar{c}} + \frac{\Delta}{2}\right) + \operatorname{sinc}\left(\frac{\bar{\omega}_c x}{4\bar{c}} - \frac{\Delta}{2}\right)\right] \\ &= \operatorname{sinc}\left(\min\left\{\frac{\bar{\omega}_c}{\bar{c}}, \frac{\omega_c}{c}\right\}\frac{x}{4} + \frac{\Delta}{2}\right) + \operatorname{sinc}\left(\min\left\{\frac{\bar{\omega}_c}{\bar{c}}, \frac{\omega_c}{c}\right\}\frac{x}{4} - \frac{\Delta}{2}\right). \end{aligned} \tag{3.4}$$

The diffraction pattern generated by the two objects is therefore entirely determined by the smaller of the two quantities inside the $\min\{...\}$ brackets. In other words, where $\omega_c = \bar{\omega}_c$, we have shown that free-space zeugmatographic imaging is diffraction-limited by the faster field. In order to beat this limit, we must either use higher frequency waves for the fast field (which is what is done in optical detection of ultrasound), or set up the system with highly dispersive boundary conditions, which is what is done in MRI. □

In the following section, we will look at how we can control the boundary conditions of the fast field to 'slow' it down enough to make slow-field-limited imaging practical.

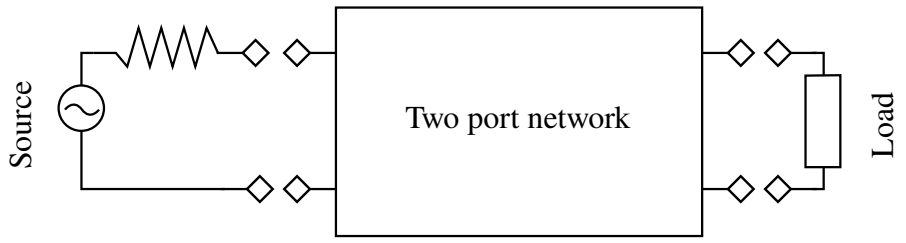

Figure 3.4: Illustration of a two-port network with a source and a load connected to it.

3.2 Electromagnetic Resonators

By modifying the boundary conditions of Maxwell's equations, we can find solutions other than the usual plane-wave solutions. In network theory, the boundary conditions are represented by a topographical arrangement of lumped elements (inductors, capacitors and resistors) in series or parallel with one another. This has been used extensively in the design of electromagnetic filters for wireless communications, sensors, and analogue circuits in general. We showed in §2.3.2 how this conceptual framework can be generalised to work with a linearised form of the acoustic wave equation and combined with the piezoelectric equations (2.40) to build an analytic model of an ultrasound transducer. Here, we discuss a more conventional use of linear circuit theory: in designing electromagnetic resonators.[1]

Consider the general two-port network shown in Figure 3.4. To build a sensor using this scheme, we would want either the voltage or current detected at the load to be as sensitive as possible to some external stimulus. The relationship between the power flowing in and out of port 1 and the power flowing in and out of port 2 is given by

[1] Although most people are familiar with network theory from electronics, it actually has its origins in being used to solve mechanical problems. This is evidenced by the borrowing of terms such as 'load' and 'impedance'.

$$\begin{pmatrix} b_1 \\ b_2 \end{pmatrix} = \begin{pmatrix} S_{11} & S_{12} \\ S_{21} & S_{22} \end{pmatrix} \begin{pmatrix} a_1 \\ a_2 \end{pmatrix}, \tag{3.5}$$

where a_1, a_2 are the power waves travelling into ports 1 and 2 respectively and b_1, b_2 are the power waves travelling out of ports 1 and 2 respectively. If the source and load in Figure 3.4 are correctly impedance matched, ie,

$$\Re(Z_L) = Z_L = R_s, a_2 = 0, \tag{3.6}$$

then the total power delivered to the load is given by

$$P_L = |S_{21} \cdot a_1|^2. \tag{3.7}$$

Our sensors work on the following principle: some external stimulus changes the properties of the two-port network and therefore the values of the S-matrix, and we then detect these changes by measuring P_L. Therefore, the sensitivity of the device M is determined by the partial derivative of (3.7) with respect to some measurable ϕ:[2]

$$M = \frac{\partial P_L}{\partial \phi} = 2\frac{\partial |S_{21}|}{\partial \phi}|S_{21}||a_1|^2. \tag{3.8}$$

Already we can note some interesting features of MOUR: firstly, if the source and load are perfectly matched, the sensitivity M is proportional to the power of the source. Secondly, if the frequency of the source is much higher than the modulation frequency of S_{21}, then the impedance matching will be stable over wide range of modulation frequencies. The reason for this is that the bandwidth of a general radio receiving system matched to the mid-band is given by

[2]This assumes that the readout of our device is proportional to the power delivered to the load.

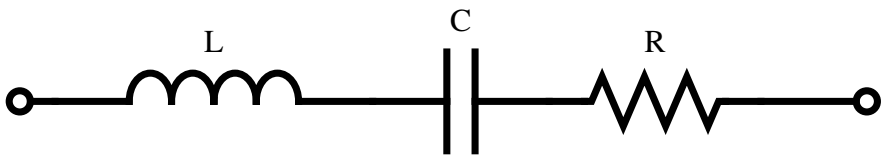

Figure 3.5: Illustration of a simple series LC resonator

$$f_{\text{high}} - f_{\text{low}} = \frac{f_0}{Q} \frac{2\Gamma}{\sqrt{1-\Gamma^2}}, \tag{3.9}$$

where $f_{\text{high}}, f_{\text{low}}, f_0$ are the high, low and centre frequencies of the impedance-matched band, Γ is the maximum voltage standing wave ratio (VSWR), and Q is the Q-factor of the transducer [7]. Therefore, the ultrasound bandwidth with a VSWR below Γ increases with increasing f_0. By having the ultrasound signal converted to a modulation of a higher-frequency electromagnetic carrier rather than simply converting it to a baseband electromagnetic representation of the signal, we can electronically impedance match for a very wide range of ultrasound frequencies.

We want to design the two-port network device to satisfy two requirements: that it should have a high sensitivity M, and that the effect should be confined in space. We will show in the following sections how we satisfied these requirements by designing a device based on a planar resonator (or notch filter). For now, we outline the basic properties of such a resonator.

Figure 3.5 shows a simple series LC resonator comprising an inductor, a capacitor, and a resistor. By Kirchhoff's current law, the currents flowing in and out of each component are balanced, therefore the current at every point in the circuit is the same, which we denote

j. Using Ohm's law to relate current j_R and voltage v_R in the resistor

$$v_R = R j_R, \tag{3.10}$$

where R is the resistance, the fact that current j_I and voltage v_I in an inductor are related by

$$v_I = L\frac{\mathrm{d}j_I}{\mathrm{d}t}, \tag{3.11}$$

where L is the inductance, and that current j_C and voltage v_C in a capacitor are related by

$$\frac{\mathrm{d}v_C}{\mathrm{d}t} = \frac{1}{C} j_C, \tag{3.12}$$

the potential difference between the two nodes, v, is found by using the fact that

$$\begin{aligned} j &= j_I = j_C = j_R, \\ v &= v_I + v_C + v_R. \end{aligned} \tag{3.13}$$

Therefore, by using the first line of (3.13) and differentiating the second line of (3.13) and substituting (3.11) and (3.12), we arrive at a differential equation for v given by

$$\frac{\mathrm{d}v}{\mathrm{d}t} = L\frac{\mathrm{d}^2 j}{\mathrm{d}t^2} + \frac{1}{C} j + R\frac{\mathrm{d}j}{\mathrm{d}t}. \tag{3.14}$$

If we drive the two terminals with a potential difference of

$$v(t) = \frac{v_0}{2}(e^{i\omega t} + e^{-i\omega t}), \tag{3.15}$$

then, without loss of generality, we can expect solutions for j of the form

$$j(t) = \frac{j_0}{2}(e^{i\omega t} - e^{i\omega t}). \tag{3.16}$$

Substituting (3.15) and (3.16) into (3.14) and solving for ω we arrive at

$$\omega_r = \pm\frac{1}{\sqrt{LC}}, \tag{3.17}$$

which gives the resonant frequency of the device. We can also write down the ratio of $Z = v_0/j_0$:

$$Z = \frac{v_0}{j_0} = iL\omega - \frac{i}{C\omega} + R, \tag{3.18}$$

which is termed the impedance of the three elements combined. This can be more clearly written as

$$Z = \frac{i}{\omega_r C}\left(\Delta - \frac{1}{\Delta}\right) + R. \tag{3.19}$$

where $\Delta = \omega/\omega_r$. We see clearly that the reactive (imaginary) part of the impedance goes to zero when $\omega = \omega_r$, whereas the resistive (real) part stays constant.

In microwave circuits, it is not typically possible to directly measure the voltage or current. Instead, what is usually measured is the power flow. In other words, we can more easily measure P_L from (3.7) than we can measure $v(t)$ or $j(t)$. The forward and backward propagating power waves which solve (3.14) can be found by a simple coordinate transformation from $(v, j) \to (a, b)$ [8]. Rather than go into the detail, we will henceforth use standard textbook microwave analysis to demonstrate the properties of the resonator.

The two-port network we will analyse is shown in Figure 3.6. The resonator from Figure 3.5 is represented by the lumped impedance Z as defined in (3.18), and a reference impedance Z' is connected as

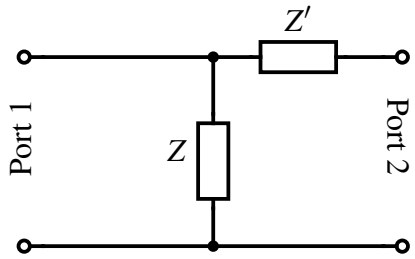

Figure 3.6: Illustration of the two port network which contains the resonator Z

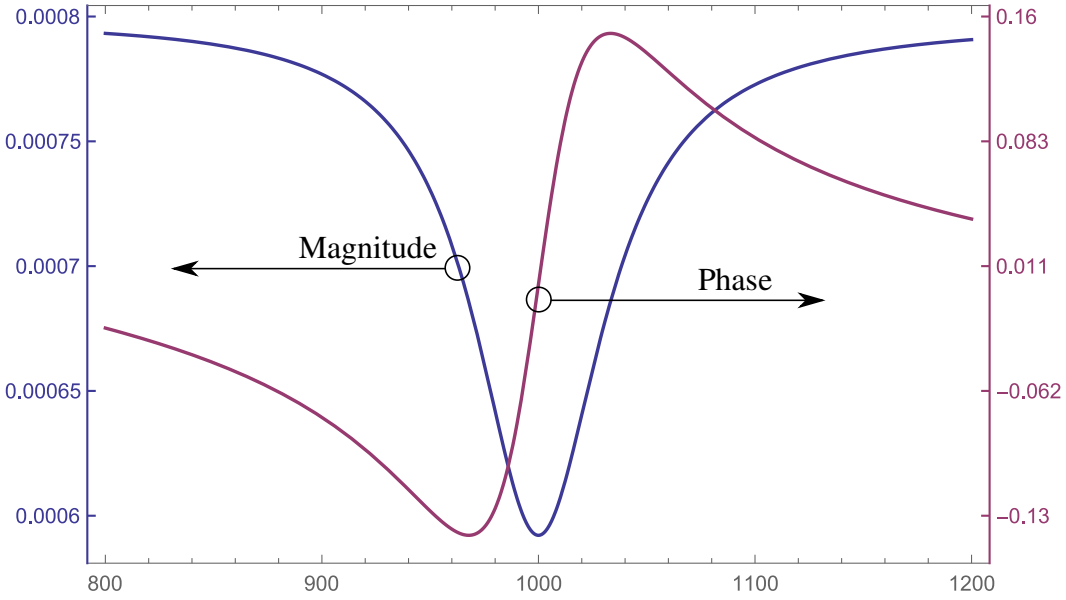

Figure 3.7: Plot of the phase and magnitude of S_{21} as a function of frequency (in arbitrary units)

shown (which we will assume is real-valued, ie, purely resistive). By analysing the network to find the values of Z_{11}, Z_{21}, Z_{12} and Z_{22} according to their standard definitions, and using standard formulae to relate these to the S-parameters, we find that

$$S_{21}(Z) = \frac{2Z'Z_0(Z+Z')}{(Z+2Z')(Z+Z_0+Z')(Z+Z_0)-ZZ'^2}. \tag{3.20}$$

S_{21} is a complex-valued function of the complex variable Z. We

can safely ignore the poles (which are non-physical) as they only occur at negative or complex values of Z and/or Z'. Power transmission $|S_{21}|$ is minimised when $|Z|$ is minimised. Since $\min[|Z(\omega)|] = R$, the minimum power transmission is

$$\min[|S_{21}(\omega)|] = \left| \frac{2Z'Z_0(R+Z')}{(R+2Z')(R+Z_0+Z')(R+Z_0) - RZ'^2} \right|. \quad (3.21)$$

Referring to (3.19), we can look at small changes to Z around the resonance at $\Delta = 1$ to study the device sensitivity. We presume (for now) that the resistances in the device are held constant. Therefore, we expect any changes to S_{21} during operation to result from perturbation of the imaginary part. Using these assumptions, $|S_{21}(\Delta)|$ around $\Delta = 1$ can be written

$$\begin{aligned} |S_{21}(\Delta)|^2 &= \min[|S_{21}|]^2 + [A(\Delta-1)]^2, \\ \text{where } A &= \frac{2}{\omega_r C} \frac{(Z_0^2 - 3Z_0Z' - Z'^2)}{Z_0(Z_0+Z')^2}, \end{aligned} \quad (3.22)$$

for $\Delta \sim 1$.

From this we note that the gradient of the change in $|S_{21}|$ with either C or Δ, either of which may be affected by the local dielectric changes, is inversely proportional to ω_r. This seems to imply that as the device resonant frequency is made higher that the sensitivity will fall in proportion. However, as we will see later, the resonant frequency appears in the opposite sense in equations relating the mechanical deformation to electromagnetic perturbation.

A full evaluation of the phase and magnitude (gain) of (3.20) is shown in Figure 3.7. Finding analytic expressions for the phase and magnitude of (3.20) is generally non-trivial, but using a similar analysis to (3.22), we can see that

$$\tan\left(\theta[S_{21}(\Delta)]\right) = \frac{A}{\min[|S_{21}|]}(\Delta - 1). \tag{3.23}$$

.

As before, this equation only holds in the region of $\Delta \sim 1$. $\tan(x)$ has discontinuities at $x = \pi/2$, which is not present on the right-hand side of the equation. We can extend the validity of (3.23) past the phase discontinuity by introducing a pole at $\Delta = \Delta'$. The phase $\theta[S_{21}(\Delta)]$ now becomes approximately

$$\theta[S_{21}(\Delta)] = \tan^{-1}\left(\frac{A}{\min[|S_{21}|]}\frac{(\Delta - 1)}{(\Delta - \Delta')}\right). \tag{3.24}$$

Now, by using the fact that

$$\frac{\mathrm{d}}{\mathrm{d}x}\tan^{-1}\left(a\frac{x-b}{x-c}\right) = \frac{a(b-c)}{a^2(b-x)^2 + (c-x)^2}, \tag{3.25}$$

we see that the gradient around $\Delta = 1$ tends towards

$$\mathrm{grad}(\theta[S_{21}(\Delta)]) = \frac{A}{\min[|S_{21}|]}\frac{\pi/2}{(\Delta - \Delta')^2}, \tag{3.26}$$

and that the gradient around $\Delta = \Delta'$ tends towards

$$\mathrm{grad}(\theta[S_{21}(\Delta)]) = \frac{\min[|S_{21}|]}{A}\frac{\pi/2}{(\Delta - 1)^2}. \tag{3.27}$$

The consequences of this for the sensitivity of the device can be seen through the relationship between the phase and magnitude of a minimum-phase system [9, 10]. The phase and magnitude of a function such as $S_{21}(\Delta)$ which is derived from a linear, reversible system are related by a Hilbert transform:

$$\log(|S_{21}(\Delta)|) = \mathscr{H}[\theta[S_{21}(\Delta)]]. \tag{3.28}$$

Using the basic properties of the Hilbert transform, we see that

$$\frac{\mathrm{d}}{\mathrm{d}\Delta}\log(|S_{21}(\Delta)|) = \mathscr{H}[\frac{\mathrm{d}}{\mathrm{d}\Delta}\theta[S_{21}(\Delta)]]. \tag{3.29}$$

We resist the temptation to continue our analysis further, instead noting the presence of expressions containing R in the calculation of the gradient of S_{21} around the regions of both $\Delta = 1$ and $\Delta = \Delta'$. From Figure 3.7, we can infer that those regions correspond to the minimum of the magnitude and the maximum of the phase. As R, and therefore $\min[S_{21}]$, increase, we expect the magnitude of the gradient of the phase of S_{21} to decrease around $\Delta = 1$, as implied by (3.26). Similarly, we expect a steeper gradient of the phase around $\Delta = \Delta'$ for an increasing R, as implied by (3.27). These gradients are related to the slope of the magnitude of S_{21} by (3.29). We omit here proof that magnitude of these gradients relate to the sensitivity of the device described by (3.8), but the author has satisfied himself through numerical computation of plots such as Figure 3.7 for various values of R that increasing R does indeed reduce sensitivity (see Figures 3.8 and 3.9, and recall that the sensitivity is related to the maximum phase and magnitude gradients of S_{21}). The point at which $\Delta = \Delta'$, where the phase change between the incoming and outgoing power wave is maximum, is known sometimes in optics as the quadrature point, and we expect this point to have the highest sensitivity.

To relate this to the observation of the previous section (§3.1.1) that zeugmatographic imaging is diffraction limited by the faster field, we note the relation

$$\frac{\mathrm{d}\omega}{\mathrm{d}k} = D\left(\frac{\mathrm{d}\theta[S_{21}]}{\mathrm{d}\omega}\right)^{-1}, \tag{3.30}$$

where D is the physical distance between the two ports. We see that the local group velocity is inversely proportional to the gradient of the phase of S_{21}. Referring once again to Figure 3.7, we see that the

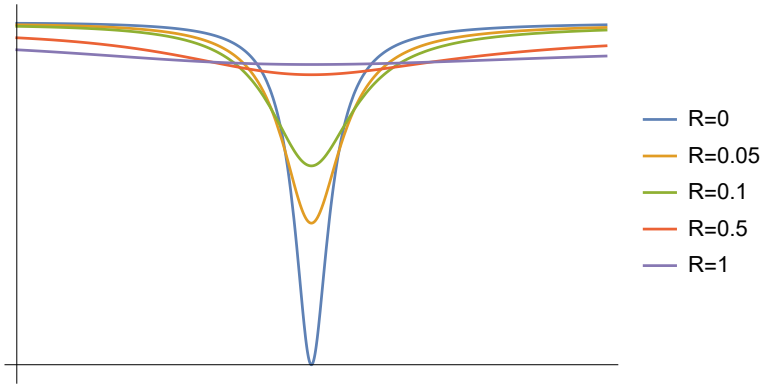

Figure 3.8: Plot demonstrating the change in the magnitude of S_{21} with varying R (arb. units)

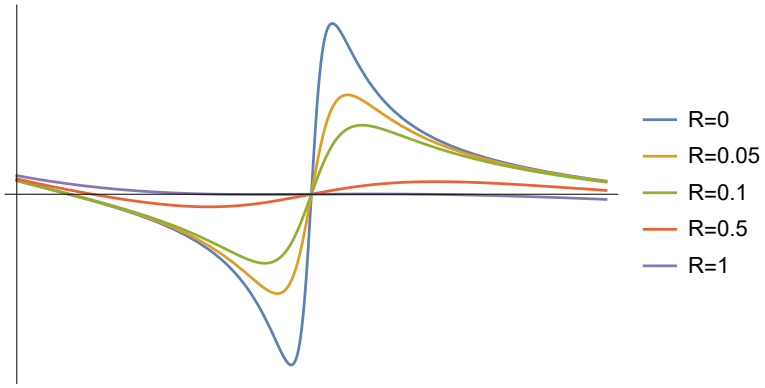

Figure 3.9: Plot demonstrating the change in the phase of S_{21} with varying R (arb. units)

maximum gradient, and therefore minimum group velocity, occurs at $\Delta = 1$. From (3.26), we further note that the 'slowness' of the wave is inversely related to R. On the other hand, the horizontal distance between the maximum and minimum of $\theta[S_{21}]$ in Figure 3.7 determines the range of 'slow' frequencies available in (3.4). Increasing the vertical difference between the maximum and minimum of $\theta[S_{21}]$ in Figure 3.7 would decrease the group velocity without affecting the range of available frequencies, but these can only differ by a maximum of π.

The parameter which links many of these concepts is the Q-factor, which, although impractical to calculate from (3.20), can be understood visually as the ratio between the full-width-half-maximum (FWHM) of $|S_{21}|$ and ω_r. Increasing R increases the ohmic losses of

the resonator and therefore dampens the resonator, reducing Q. This has two effects: first, it reduces the sensitivity M. Secondly, it increases the group velocity across the device, lowering the maximum frequency of the slow field (ie, acoustic field) which can be imaged. The challenge in designing devices which can fully spatially sample acoustic fields using electromagnetic resonators is balancing the requirements of resolution and sensitivity: smaller devices must (generally) have higher-frequency resonance; but, due to the skin effect, higher frequency microwaves increase R, and therefore reduce sensitivity as well as increasing the group velocity.

3.3 The Covered Microstrip Effect

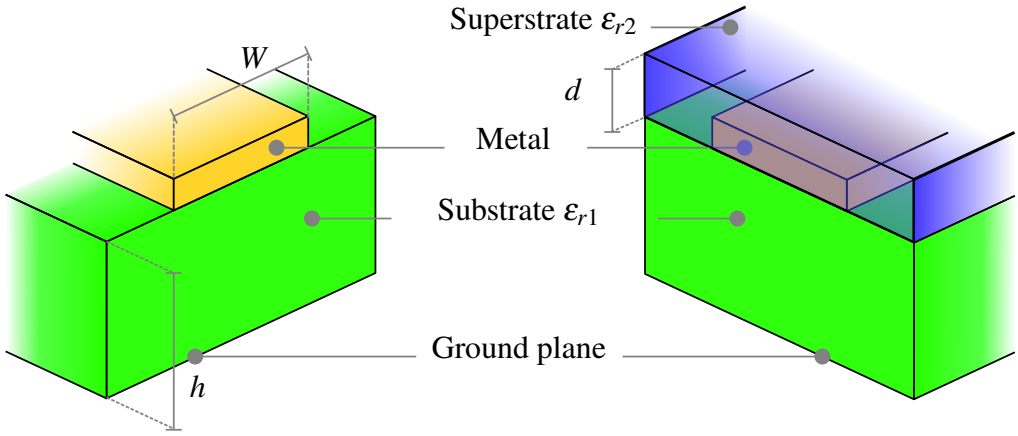

Figure 3.10: Drawings of microstrip waveguides both with (right) and without (left) an extra superstrate layer of thickness d. The device on the left has a capacitance C_0 when setting $\varepsilon_{r1} = 1$, which can be used to calculate the effective permittivity of the waveguide on the right by the variational principle. We assume in what follows that the metal strip is infinitely thin and is a perfect conductor.

We have considered so far how a resonator might be used to detect changes in some physical variable using (3.8). However, we have not yet looked at how those changes might affect the two-port system itself. For this, we take advantage of an effect long known to designers of weather-proofed microstrip antennae, which we describe below.

Consider a simple copper microstrip on a dielectric substrate. The

board may be coated with a dielectric superstrate layer, as shown in Figure 3.10. The equation for the effective dielectric constant ε_{e0} of a microstrip without a dielectric covering (left picture in Figure 3.10) is [11]

$$\varepsilon_{e0} = \frac{\varepsilon_{r1}+1}{2} + \frac{\varepsilon_{r1}+1}{2}\frac{1}{(1+12h/W)^{1/2}}, \tag{3.31}$$

where ε_{r1} and h are the relative permittivity and height of the dielectric substrate, and W is the width of the microstrip, as shown in Figure 3.10. The total phase accumulation, ϕ, over a distance L for a signal with frequency ν in such a microstrip is

$$\phi = i2\pi\nu\sqrt{\varepsilon_e}L/c, \tag{3.32}$$

where c is the speed of light in free space. By applying the variational principle [11, 12] to (3.31), we can approximate ε_e for a microstrip with a dielectric superstrate of thickness d and relative permittivity ε_{r2} by computing the integrals [13]

$$\frac{1}{\varepsilon_e} = \frac{C_0}{\pi\varepsilon_0}\int_0^\infty \frac{[\tilde{f}(\beta)]^2}{\left[\varepsilon_{r2}\frac{\varepsilon_{r2}\tanh\beta d+1}{\varepsilon_{r2}+\tanh\beta d} + \varepsilon_{r1}\coth(\beta h)\right](\beta h)}\mathrm{d}(\beta h), \tag{3.33}$$

where C_0 is the capacitance for a microstrip line in free space and

$$\begin{aligned}\tilde{f}(\beta) = 1.6\,\mathrm{sinc}(\beta W/2) + \frac{2.4}{(\beta W/2)^2}[\cos(\beta W/2) \\ -2\,\mathrm{sinc}(\beta W/2) + \mathrm{sinc}^2(\beta W/4)],\end{aligned} \tag{3.34}$$

is the Fourier transform of a trial function for the charge distribution over the metallic strip.[3]

Calculating C_0 using standard microstrip formulae [11] and plug-

[3]Innacuracies in the trial function will only give us second-order errors in the calculation of ε_e. More details can be found in [13].

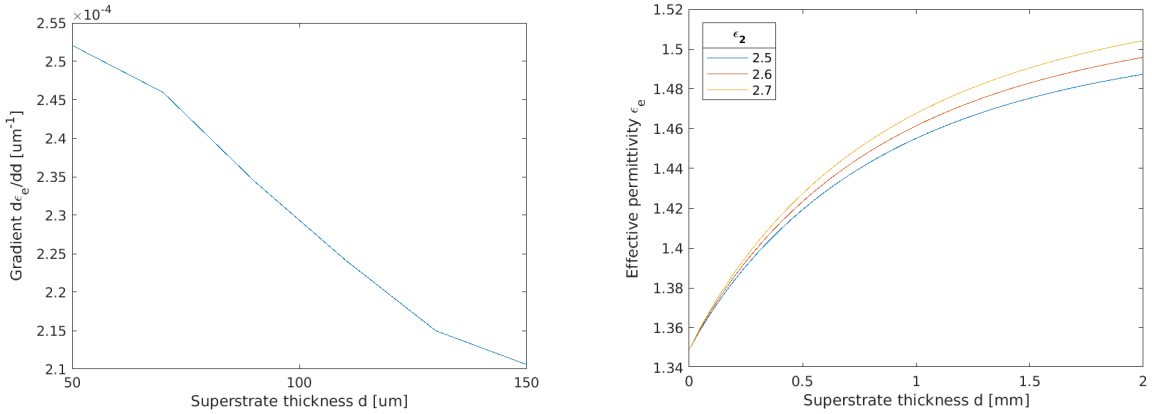

Figure 3.11: Plots of $\mathrm{d}\varepsilon_e/\mathrm{d}d$ (left) and ε_e (right) by numerical computation of the integral in (3.33) using MATLAB. Parameters for all plots are $h = 1\,\mathrm{mm}$, $\varepsilon_{r1} = 4.4$ and $W = 3\,\mathrm{mm}$. For the left figure, $\varepsilon_{r2} = 9$.

ging it into (3.33) gives a value for ε_e, the effective relative permittivity of the covered microstrip. Some plots of ε_e and $\mathrm{d}\varepsilon_e/\mathrm{d}d$ against the superstrate thickness d and ε_{r2} for some example parameters are shown in Figure 3.11. We note that changes in the thickness of the superstrate layer do indeed cause a change in the effective permittivity ε_e. When ultrasound is incident on this layer, and provided it is made of a well impedance-matched material (more on this later), it will experience deformation. This causes a change in d, and hence ε_e: in this way the microstrip device becomes a parametric oscillator. The changes in d can be detected using a local oscillator mixed with the phase-altered signal as per (3.32).

Alternatively, we can note that building the resonator shown in Figure 3.5 as a planar structure on a piece of circuit board will necessarily be sensitive to any local change in the effective permittivity. Although the above analysis is for a general microstrip, we found in experiments outlined in later sections that this effect acts to shift the resonance of compact resonators.

The arrangement of a substrate and superstrate is particularly convenient for two reasons: firstly, it allows us to construct our devices

using basic processes from consumer electronics such as printed circuit board (PCB) manufacture with only a simple coating step afterwards to create the superstrate layer. Secondly, it acts by default as a high-impedance-backed acoustic device described in §2.3.2. Not being restricted to materials which have a strong piezoelectric effect, we have a good deal of freedom in choosing the acoustic impedance of the superstrate and also selecting a material which can trivially be deposited in very thin layers, such as Paralyne. Multilayer superstrate structures can also be easily realised. It also turns out that the materials best electromagnetically suited to become our substrate, namely high ε ceramics, also tend to exhibit high acoustic impedance.

3.4 Channel Multiplexing

In a traditional ultrasound system, each transducer element is connected in parallel to its own RF channel. Older systems tended to have a lower number of amplifier and display or digitisation channels than individual elements. The system would switch between different combinations of elements and also between transmit and receive circuitry. More modern systems will have a dedicated acoustic front end (AFE) for each element, digitising each channel in parallel and transmitting data either serially or in parallel over a digital link. These types of systems are shown schematically in Figure 3.12

Our work on MOURs implies a third option for multiplexing, which can be entirely passive. Instead of connecting each element to a matrix of RF switches, or to its own digitisation pipeline, the entire array can be addressed using a single electrical connection, as shown in Figure 3.13. The way this works is as follows: each element is assigned its own microwave resonant frequency. A chain of two-port networks like the one shown in Figure 3.4 is assembled by connecting the output of each to the input of the next, as shown in Figure 3.14. If we gen-

erate N signals of amplitude $a_1, a_2, ..., a_N$ at the source of frequency $f_1, f_2, ..., f_N$ and the transfer function at each section of the cascade is $S_{21}^{(1)}, S_{21}^{(2)}, ...S_{21}^{(N)}$ corresponding to complex impedances $Z_1, Z_2, ..., Z_N$, then the power wave detected at the detector is given by

$$b = S_{21}^{(1)} S_{21}^{(2)} ... S_{21}^{(N)} (a_1 + a_2 + ... + a_N). \tag{3.35}$$

Since each signal on the right-hand-side is a pure tone, we can use the fact that

$$S_{21}^{(n)}(f) = 1 \text{ for } |f - f_n| \gg \text{FWHM}, \tag{3.36}$$

where FWHM is the full-width-half-maximum of the resonance, to simplify (3.35) to:

$$b = S_{21}^{(1)} a_1 + S_{21}^{(2)} a_2 + ... + S_{21}^{(N)} a_N. \tag{3.37}$$

To extract the signal from each spatial channel, we can either pass b through a signal demultiplexer, or tune to one frequency at a time and read out each element separately. There are some other more elaborate options: we could address the elements by a chirped frequency, which rapidly sweeps across all of the elements. Or we could down-convert b into an intermediate frequency (IF) which can be directly digitised and perform the demultiplexing in software.

There are several advantages to these approaches over the ones outlined in Figure 3.12. The first is that we do not have to integrate any active components into the transducer elements themselves. This saves us from a long-standing challenge in the manufacture of ultrasound imaging devices, whereby active electronic components must be integrated in such a way as to provide the appropriate acoustic impedance environment for efficient transduction. Active CMOS devices for cam-

eras have long been made with pixel sizes well below what is needed for acoustic imaging: photosensitive CMOS devices can be made by stacking doped and un-doped hydrogenated amorphous silicon on top of one another, allowing photosensitive regions to be deposited directly on top of signal acquisition circuitry [14]. In acoustics, there is no direct equivalent: acoustic energy is not transferred into electrical through a direct interaction with electrons in a semiconductor, rather the mechanical energy must first be transferred from the medium into a mechanical vibration of the device, and then finally into electrical energy. As we saw in §2.3.2, designing devices which can do this efficiently is not trivial. Therefore, ultrasound imaging arrays generally rely on one of three techniques for multiplexing: (1) each element is individually connected to its own readout cable (most systems today); (2) a piezoelectric or CMUT layer is bonded to a CMOS substrate containing the active pixel matrix in a difficult two-step process [15–17]; (3) a 'compromise' piezoelectric material which is foundry-compatible, such as scandium aluminium nitride, is used and micro-machined to have the desired acoustic backing properties [18].

What our devices allow is for multiple acoustic elements to be addressed with a single readout pathway. In other words, a 2D metallisation pattern can take the place of an active pixel array and allow each element to be read out by tuning a microwave carrier to that element's electromagnetic resonant frequency. In very simple embodiments, this can be achieved using a simple PCB, but for integrated circuit (IC) packages, a single layer metallisation process can be used. This greatly simplifies the design of 2D matrix transducers and makes it relatively simple to realise a wide variety of designs and configurations with low tooling overhead.

The limitations of frequency multiplexing can be seen by looking at Figure 3.15. In the left-hand plot, R is small enough such that

each resonance can be clearly distinguished from its nearest neighbours, meaning that (3.36) and therefore (3.37) hold. However, in the right-hand figure, we can see clearly that (3.36) no longer applies, and the elements cross-talk with each other. To remedy this, we would need to move the resonances $f_1, ..., f_n$ further apart. This has two consequences: firstly, it means we need more bandwidth for each channel, which makes the design of our source and receiver more difficult and potentially expensive. Secondly, it pushes more channels up into higher frequencies, meaning more ohmic losses and a larger effective R, further exacerbating the channel density problem and worsening the sensitivity.

There is a further consideration to bear in mind when cascading the receiving elements as per Figure 3.14: the passband (ie, the range of frequencies for each device which are outside the resonance FWHM) of each device is, in practice, always somewhat attenuating. This means that there is signal loss at all points along the device.

In practice, we envision that frequency multiplexing will be done in banks of elements: in other words, full-system designs may use a combination of digital multiplexing shown in Figure 3.12 and passive frequency multiplexing shown in Figure 3.13.

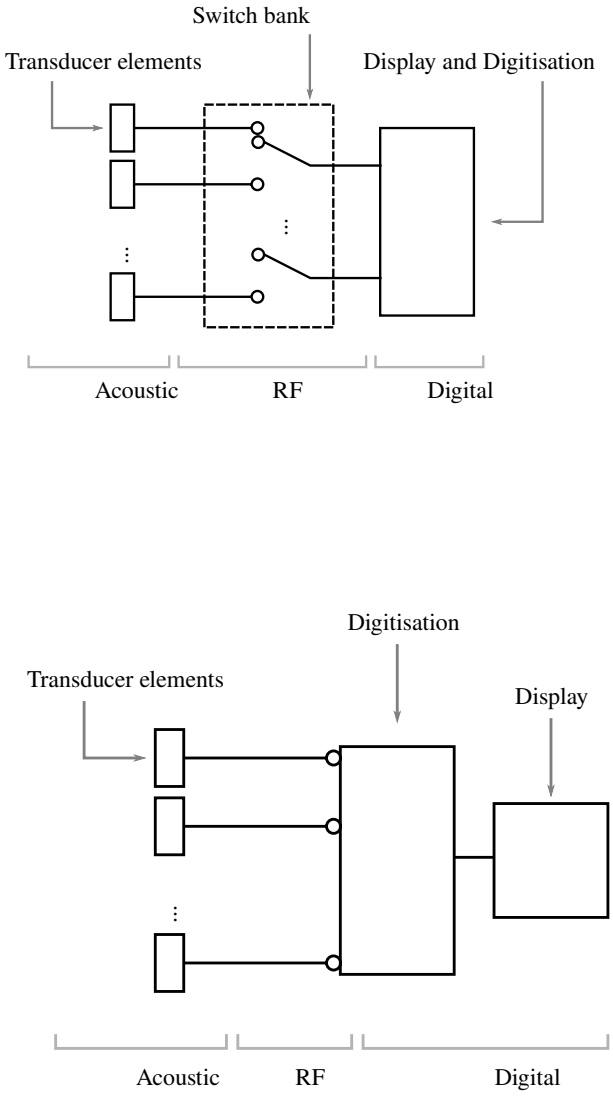

Figure 3.12: Schematics of different types of ultrasound receiving systems. The top image shows a traditional system with switched RF circuits. The bottom image shows a modern digital system whereby each element has its own digitisation pipeline.

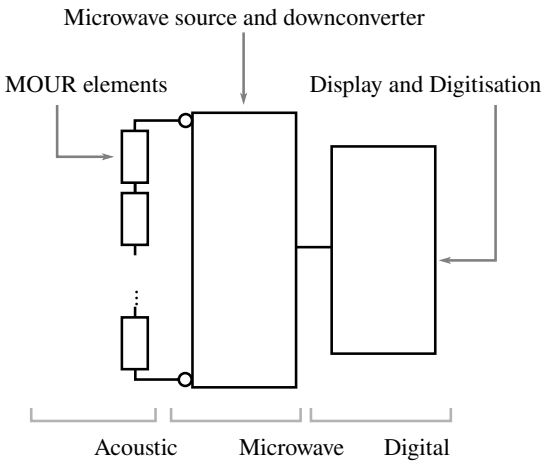

Figure 3.13: Schematics of a MOUR device, wherein elements can be connected in series and frequency multiplexed.

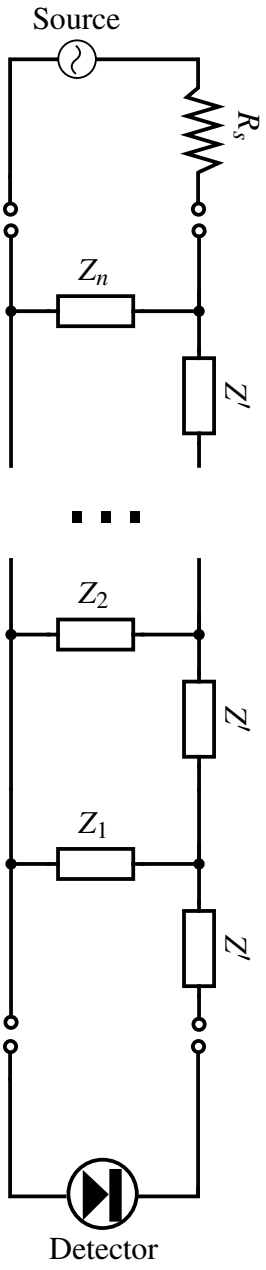

Figure 3.14: Cascaded two-port networks to create a frequency-addressable array of MOUR devices

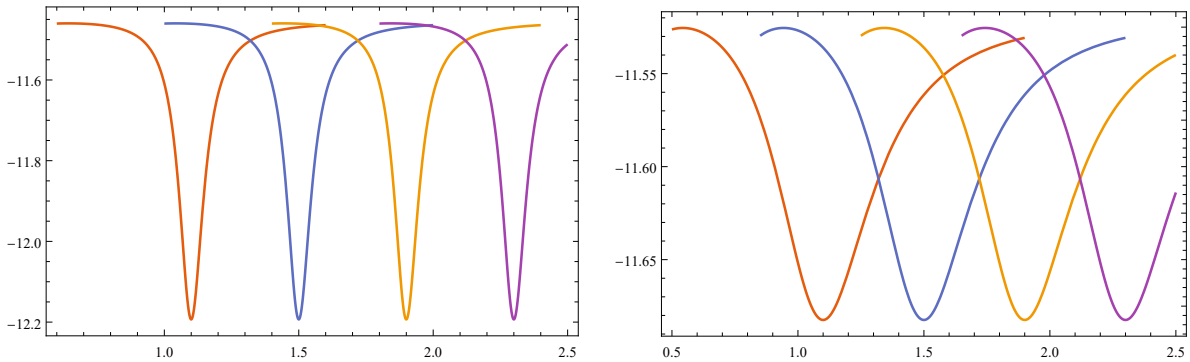

Figure 3.15: Plots of multiple resonances connected in series with arbitrary units of frequency on the x-axis and arbitrary units of gain on the y-axis. The resistance R in the right-hand plot is $8\times$ higher than the left-hand plot

References

[1] Frederick V. Hunt. *Electroacoustics: The Analysis of Transduction, and Its Historical Background*. 5. Acoustical Society of America, 1954.

[2] George Frost Kennan. *Memoirs, 1950-1963*. Pantheon Books, 1983. 372 pp. isbn: 978-0-394-71626-8. Google Books: xiMCAAAACAAJ.

[3] David John Edwards and Pithawat VACHIRIMON. "Acousto- Electromagnetic Investigation of Physical Properties of an Object". Pat. WO2013041856A1 (WO). Isis Innovation Limited. Mar. 28, 2013. url: https://patents.google.com/patent/WO2013041856A1/en?oq=WO2013041856A1 (visited on 12/24/2019).

[4] Edward Zhang, Jan Laufer, and Paul Beard. "Backward-Mode Multiwavelength Photoacoustic Scanner Using a Planar Fabry-Perot Polymer Film Ultrasound Sensor for High-Resolution Three-Dimensional Imaging of Biological Tissues". In: *Applied Optics* 47.4 (Feb. 1, 2008), pp. 561–577. issn: 2155-3165. doi: 10.1364/AO.47.000561. url: https://www.osapublishing.org/abstract.cfm?uri=ao-47-4-561 (visited on 07/27/2017).

[5] P. C. Lauterbur. "Image Formation by Induced Local Interactions: Examples Employing Nuclear Magnetic Resonance". In: *Nature* 242.5394 (Mar. 1973), pp. 190–191. issn: 1476-4687. doi: 10.1038/242190a0. url: https://www.nature.com/articles/242190a0 (visited on 12/24/2019).

[6] G. Konstantinou et al. "Dynamic Wavefront Shaping with an Acousto-Optic Lens for Laser Scanning Microscopy". In: *Optics Express* 24.6 (Mar. 21, 2016), pp. 6283–6299. issn: 1094-4087. url: http://dx.doi.org/10.1364/OE.24.006283 (visited on 01/15/2018).

[7] Alfred R. Lopez. "Double-Tuned Impedance Matching". In: *IEEE Antennas and Propagation Magazine* 54.2 (Apr. 2012), pp. 109–116. issn: 1558-4143. doi: 10.1109/MAP.2012.6230722.

[8] K. Kurokawa. "Power Waves and the Scattering Matrix". In: *IEEE Transactions on Microwave Theory and Techniques* 13.2 (Mar. 1965), pp. 194–202. issn: 1557-9670. doi: 10.1109/TMTT.1965.1125964.

[9] John Bechhoefer. "Kramers–Kronig, Bode, and the Meaning of Zero". In: *American Journal of Physics* 79.10 (Sept. 26, 2011), pp. 1053–1059. issn: 0002-9505. doi: 10.1119/1.3614039. url: https://aapt.scitation.org/doi/10.1119/1.3614039 (visited on 02/05/2020).

[10] Hendrik W. Bode. *Network Analysis & Feedback Amplifier Design*. url: http://archive.org/details/NetworkAnalysisFeedbackAmplifierDesign (visited on 02/05/2020).

[11] Ramesh Garg, Inder Bahl, and Maurizio Bozzi. *Microstrip Lines and Slotlines*. 3rd ed. Artech House, May 1, 2013. 603 pp. isbn: 978-1-60807-535-5. Google Books: 1PQfAgAAQBAJ.

[12] E. Yamashita and R. Mittra. "Variational Method for the Analysis of Microstrip Lines". In: *IEEE Transactions on Microwave Theory and Techniques* 16.4 (Apr. 1968), pp. 251–256. issn: 0018-9480. doi: 10.1109/TMTT.1968.1126658.

[13] I. J. Bahl and S. S. Stuchly. "Analysis of a Microstrip Covered with a Lossy Dielectric". In: *IEEE Transactions on Microwave Theory and Techniques* 28.2 (Feb. 1980), pp. 104–109. issn: 0018-9480. doi: 10.1109/TMTT.1980.1130018.

[14] Tzu-Chiang Hsieh and Calvin Chao. "Camera with MOS or CMOS Sensor Array". U.S. pat. 20040135209A1. P-PHOCUS. July 15, 2004. url: https://patents.google.com/patent/US20040135209A1/en?q=cmos&q=camera&q=sensor&q=H04N5%2f335&before=priority:20050101&page=1 (visited on 02/06/2020).

[15] Neal R. Butler and Marvin E. Lasser. "Two Dimensional Transducer Integrated Circuit". U.S. pat. 5483963A. Lockheed Martin IR Imaging Systems Inc. Jan. 16, 1996. url: https://patents.google.com/patent/US5483963A/en?assignee=Imperium%2c+Inc. (visited on 06/18/2019).

[16] John K. Schneider and Jack C. Kitchens. "Hydrophone Array Module". U.S. pat. 7436736B2. Ultra-Scan Corp. Oct. 14, 2008. url: https://patents.google.com/patent/US7436736B2/en (visited on 07/10/2019).

[17] Jonathan M. Rothberg et al. "Microfabricated Ultrasonic Transducers and Related Apparatus and Methods". U.S. pat. 9067779B1. Butterfly Network Inc. June 30, 2015. url: https://patents.google.com/patent/US9067779B1/en?assignee=butterfly+network&oq=butterfly+network (visited on 03/11/2019).

[18] Qi Wang et al. "Design, Fabrication, and Characterization of Scandium Aluminum Nitride-Based Piezoelectric Micromachined Ultrasonic Transducers". In: *Journal of Microelectromechanical Systems* 26.5 (Oct. 2017), pp. 1132–1139. issn: 1941-0158. doi: 10.1109/JMEMS.2017.2712101.

Chapter 4

The Development of Microwave Oscillator Ultrasound Receivers

In the previous chapter, we outlined the concept of MOURs through its key components: an electromagnetic resonator, a deformable superstrate layer, and a multiplexing scheme. We also discussed the minimum requirements needed to do full resolution ultrasound imaging using MOUR and a plane wave ultrasound source.

In this chapter, we look at how we can meet these requirements through careful electromagnetic design and material choice. This leads us to building a proof-of-concept single element device, which we tested in a carefully designed experiment outlined in Chapter 5.

The key requirement for successful implementation of MOUR is that the resonators can be made sufficiently small (and therefore allow high-resolution ultrasound imaging), whilst still having a resonant frequency within the range of available sources, and whilst being sufficiently sensitive for the application at hand.

4.1 Electromagnetic Design

We investigated designs for electromagnetic resonators based on planar copper structures on conventional circuit board material (such as FR4). The idea of using antenna structures for detecting physical changes such as strain [1] and temperature [2] had already been ex-

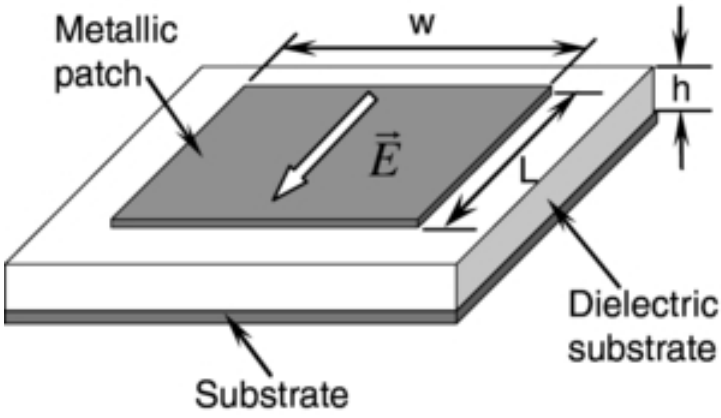

Figure 4.1: The patch antenna considered in [1] for strain measurements.

plored, usually for passive remote structural health monitoring. However, not being interested in having a system which can be read-out wirelessly, we found the simple patch antenna designs were not compact enough for our needs. For instance, in [1], a 20 GHz antenna on a substrate with relative permittivity 3.4 had dimensions of 5 mm $\times$ 4 mm (see Figure 4.1).

To find more compact designs, we considered spoof surface plasmon (SSP) sensors [3]. An SSP mimics the bounded modes present in metal-on-dielectric structures with finite conductivity at optical frequencies by patterning the metal layer. This allows an analogous effect to occur at lower microwave frequencies, enabling bound modes which can enhance the local field intensities by many orders of magnitude. In some studies [4, 5], it has been shown that the transmission or reflectivity properties of a patterned sheet of metal-on-dielectric in the terahertz range can be made highly sensitive to changes to the local dielectric environment. Other work [6] has demonstrated planar waveguiding structures based on these principles.

The work of James Seddon on inductively coupled SSP waveguide resonators [7] was the starting point for the present work on MOUR. In our early investigations, we considered a spiral resonator structure

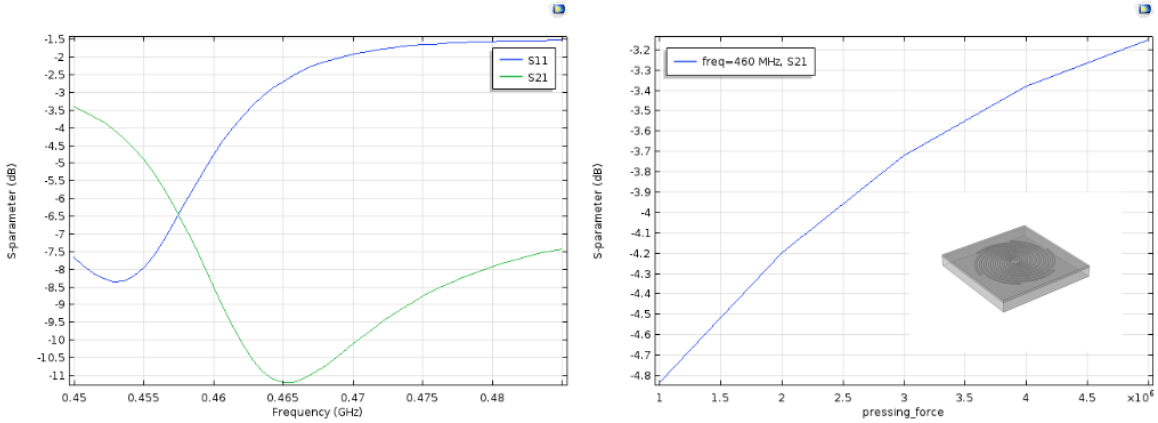

Figure 4.2: COMSOL simulation of spiral SSP structure. Left: Finite difference S_{21} and S_{22} calculations for air-coupled EM waves travelling downwards. Right: S_{21} measured at 0.46 GHz for various static pressures on the PDMS superstrate. Inset: Illustration of the device

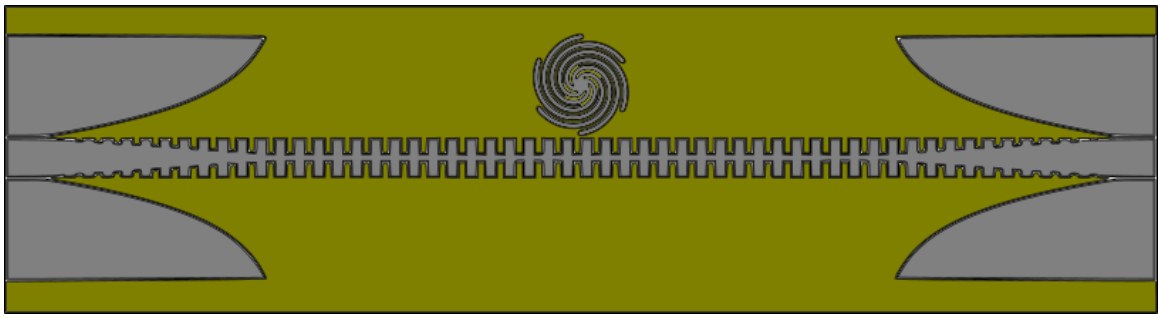

Figure 4.3: Illustration of a spiral resonator coupled to a coplanar waveguide (CPW) via an SSP waveguide

on a piece of FR4 circuit board with a 1 mm PDMS superstrate. This structure was assembled in COMSOL and simulated using a coupled multiphysics solver. After determining the transmission and reflection properties of the structure for air-coupled electromagnetic waves in the sub-GHz range, we ran a frequency-domain simulation coupled to a mechanical deformation simulation for a variety of homogeneous static pressures exerted on the top face of the structure (see Figure 4.2).

We made and tested several designs based on spiral SSP resonators. Figure 4.4 illustrates the layout designed by James Seddon using CST Microwave Studio. The board was manufactured using a wet etch PCB process on FR4 copper laminate circuit board. SMA

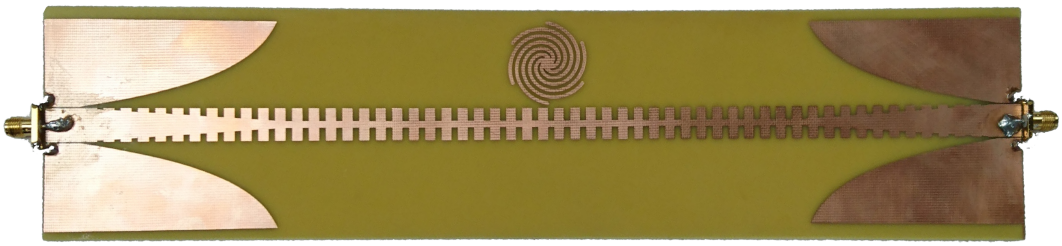

Figure 4.4: Photo of the resonator described above wet etched onto FR4 circuit board and connectorised

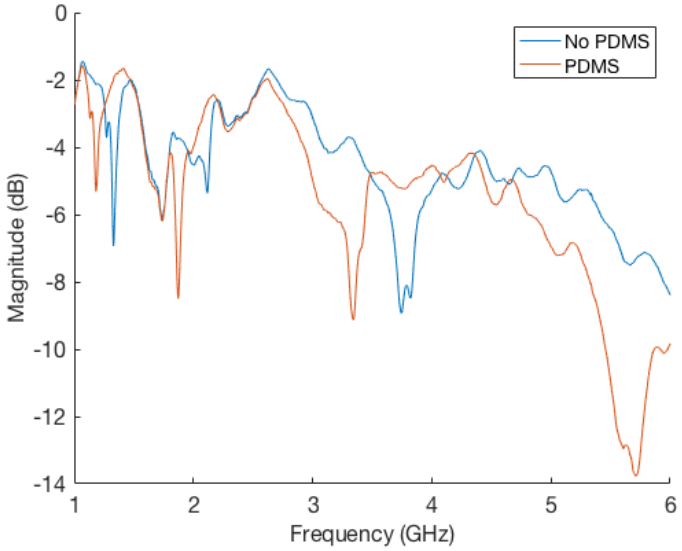

Figure 4.5: Plot of the S_{21} spectrum for the spriral resonator with and without an approximately 1 mm layer of PDMS on top

connectors were soldered onto either end. The grounds of the SMA connectors are connected to the fin-shaped structures either end of the board, and the signal pin is connected to the central strip. The first section of the feed acts as a coplanar waveguide (CPW), which gradu-

ally turns into a SSP waveguide [7, 8]. We measured the S_{21} spectrum using a network analyser (Agilent Technologies E5071C), plotted in Figure 4.5. The spectrum was measured both with and without a piece of 1 mm thick piece of polydimethylsiloxane (PDMS) placed on top. We noted that the resonances at 3.9 GHz and 1.3 GHz are red-shifted when the piece of PDMS was placed on the device, covering the resonator. This demonstrates the generality of the theory outlined in §3.3 to complex structures such as SSP.

There are some drawbacks to this design. Firstly, the feed-in is a coplanar waveguide. This requires a larger pitch between adjacent parallel waveguides, and greater sensitivity to the dielectric environment (recall that we only want the device to be sensitive over a small region). Secondly, the spiral resonator, although itself compact, must be placed adjacent to the SSP transmission line in order to couple to it. This again increases the space needed between parallel sensors, and therefore reduces the maximum ultrasound resolution we would be able to achieve.

To find more compact designs, we turned to the literature on meandered slotline defected microstrip (MS-DMS) structures [9–11]. An ideal slotline or microstrip stub will generally have a resonant frequency f_r determined by the formula [11]

$$f_r = \frac{c}{2l_s\sqrt{\varepsilon_e}}, \tag{4.1}$$

where c is the speed of light, l_s is the length of the stub, and ε_e is the effective permittivity of the stub. A meandered slotline can be embedded within a microstrip, which forms our MS-DMS. At the resonant frequency, the propagating EM wave will couple to the standing wave mode in the slotline [12]. An illustration of the structure is shown in Figure 4.6.

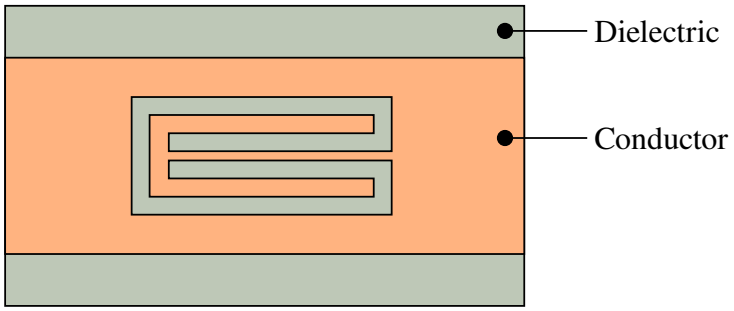

Figure 4.6: Drawing of the MS-DMS structure on a microstrip. l_s corresponds to the total length of the slotline embedded within the conductor

This structure achieves high Q-factor resonances with a compact form factor. Because it is integrated into the transmission line itself, it takes up a very small amount of space. Although even more compact designs—such as the double spiral or 'palmier' shaped MD-DMS of [11]—are possible, we used the design shown in Figure 4.6 as the basis for our designs.

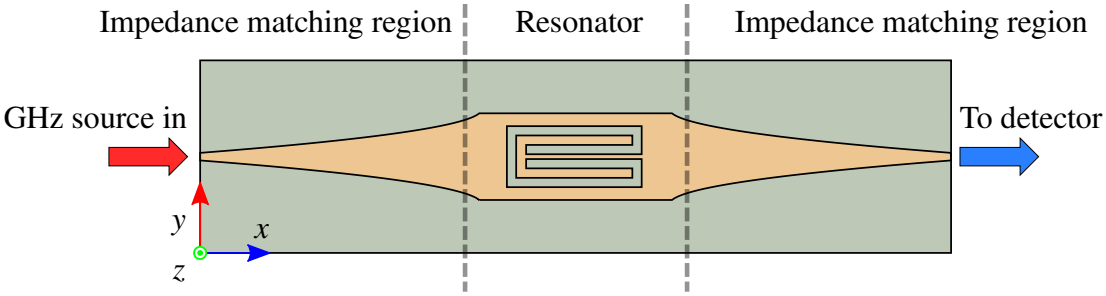

Figure 4.7: Drawing of the MS-DMS with tapered impedance matching regions

Our design choices are highly constrained in that we need the resonator to be compact, yet have a low enough frequency to be reachable by consumer-grade signal generators and not experience high ohmic losses. The choice of substrate is also important, as it should be of a high relative electric permittivity whilst having a low loss tan-

gent. At the same time, the substrate acts as the acoustic backing and should therefore have a high acoustic impedance (see §2.3.2). Given these constraints, it is generally not possible to design the resonator around a microstrip with a 50 Ω impedance, especially since we were bound by the small range of available circuit board thicknesses off-the-shelf. In general, it was necessary to design the microstrip with tapered impedance matching regions either side. In this way, the resonator section of the device could be impedance matched to the 50 Ω feed lines coming in and out. An illustration of this scheme can be seen in Figure 4.7.

4.1.1 Simulation

To develop and optimise our designs, as well as predict the performance as a sensor, we ran finite difference time domain (FDTD) simulations in CST Microwave Studio. The device was built as a 3D model with a pair of discrete edge ports on either end. The simulation domain featured 10 mm of surrounding space along the x-axis either side of the device and 5 mm of space along the z-axis above the device. The planes defined by the y-axis on either side of the device were defined as periodic. The upper z-plane was defined as open, and all the other planes were grounded ($E_\perp = 0$).

To design the impedance matching sections of the device, we defined them as parametric curves defined by a quadratic equation $ax^2 + bx + c$. The four curves have the same parameters, making the device symmetrical (except for the defect structure in the middle). We used the in-built optimiser to tune the values of a, b and c. The optimisation goal was to maximise S_{21} at a frequency well outside the resonance. This is important for the reasons discussed in §3.4, particularly with reference to (3.35), (3.36) and (3.37), where in order to multiplex the MOURs using cascading resonators, it is important to

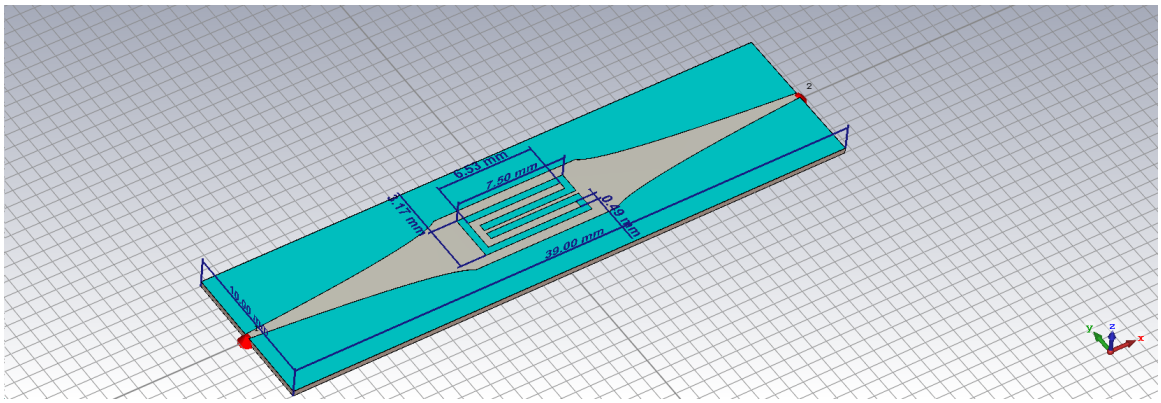

Figure 4.8: 3D render of the resonator device with dimensions in millimetres. The red cones indicate the positions of the ports.

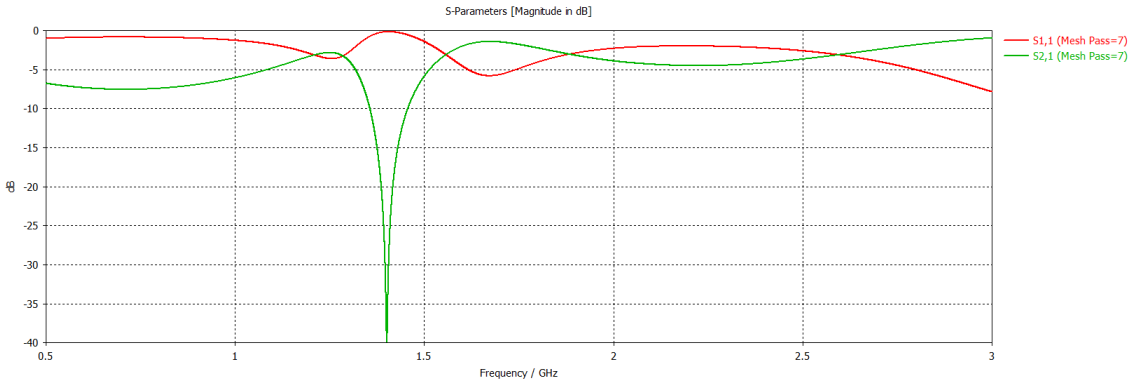

Figure 4.9: Plot of FDTD simulated S-parameters for PEC model

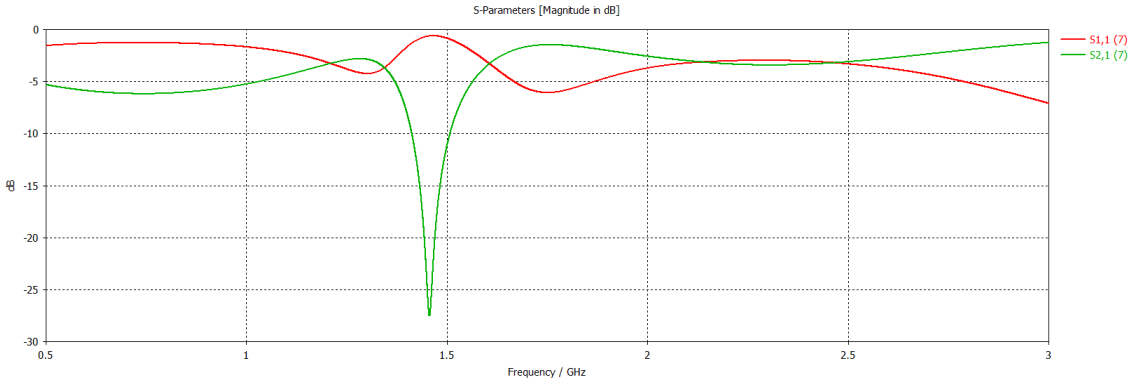

Figure 4.10: Plot of FDTD simulated S-parameters for lossy metal model

have high transmission of the signal outside of the resonance.

Figure 4.8 shows the 3D model implemented in CST, with the ports indicated by red cones. The dimensions of the model are shown in millimetres. We ran simulations using the FDTD solver with a

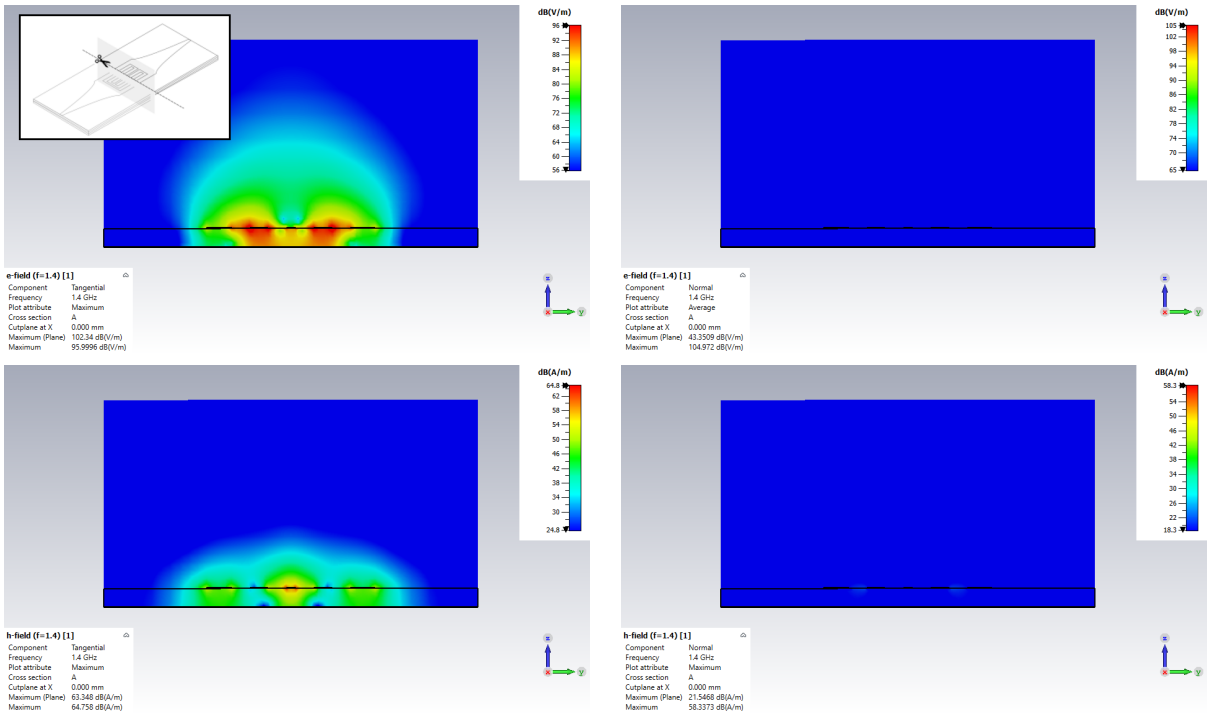

Figure 4.11: Contour plots of the E (top) and H (bottom) field magnitude for the tangential (left) and normal (right) components, taken from a slice indicated by the inset image

hexahedral mesh of 20 cells per wavelength and further refinements near the resonator features, resulting in a total mesh cell count of over 400,000. The dielectric was specified as a 0.49 mm thick piece of lossy Rogers RT6010 circuit board with a relative permittivity of 12.85. We ran the simulation both with metal parts simulated as perfect electric conductors (PEC) and as lossy annealed copper using a built-in semi-empirical loss model. The S-parameters calculated from the results for the PEC and lossy models are shown in Figures 4.9 and 4.10 respectively. The resonance occurs at 1.4 GHz. Away from the resonance, insertion loss S_{21} is between -1 dB and -5 dB for both models, but reflections are generally high in all cases. For this reason, care should be taken to design systems sources with good isolators to avoid damage to components.

Referring to 4.11, we note that the E and H fields in the direction of

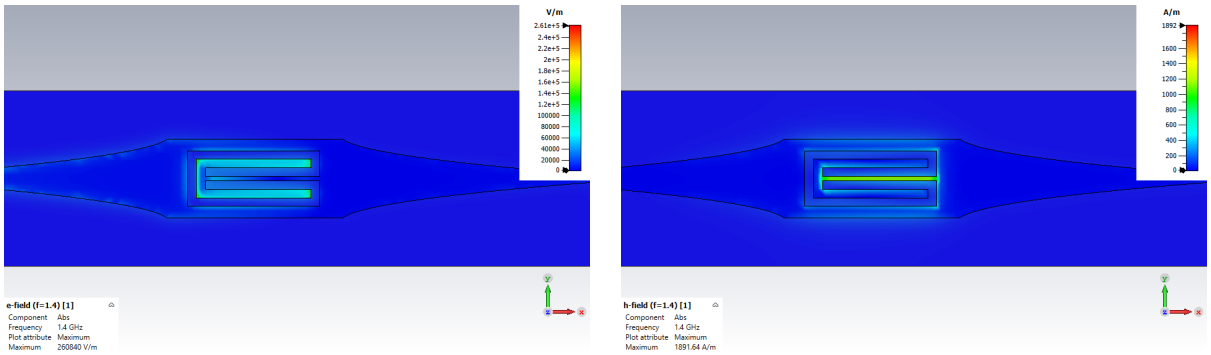

Figure 4.12: Contour plots of the maximum E (left) and H (right) field absolute magnitudes at the surface of the resonator

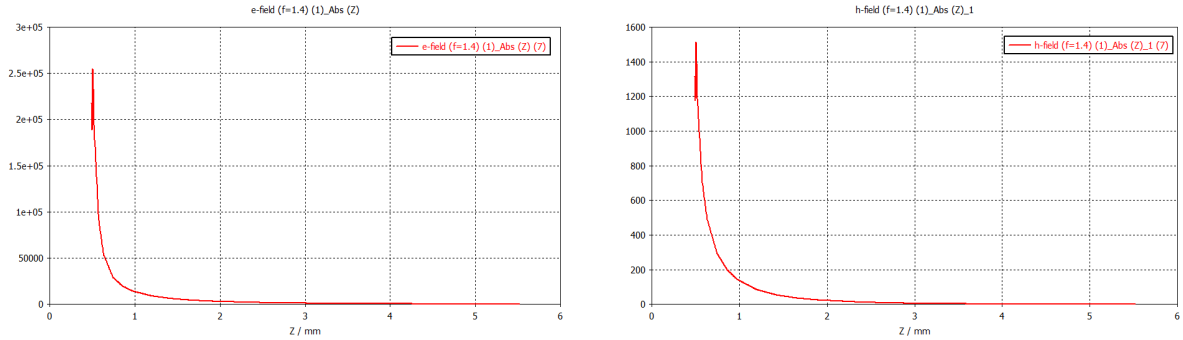

Figure 4.13: Plot of the E (left) and H (right) field intensity with increasing distance from the top face of the device.

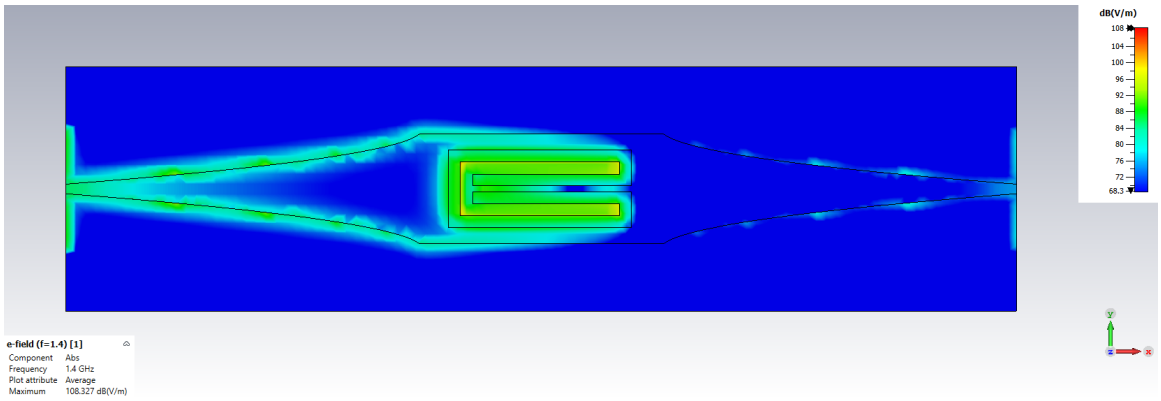

Figure 4.14: Contour plot of the E-field at the surface of the microstrip on-resonance

propagation at the resonator on resonance are nearly zero. Virtually all of the E and H field is confined to the transverse plane of propagation. The resonantor mode is therefore a quasi transverse electromagnetic (TEM) mode, which is what enables the strong coupling between it and

the propagating microstrip mode, which is also a quasi-TEM waveguide. This also tells us something important and unusual about these sensors: that, unlike in optical Fabry-Perot sensors, all of the field lines in the present embodiment are confined to the yz-plane. In the Fabry-Perot sensors, diffraction effects result in beam walk-off, which depolarises the light [13]. In our device, it may be possible to enhance the interaction between the field and the superstrate by using an anisotropic material and polling it along the x-axis (see, for instance, this paper on ferroelectric contributions to the high-frequency electric permittivity of certain materials [14]). We discuss this in §4.4.

We note further, referring to Figure 4.12, that the E-field is concentrated around a section of dielectric forming a horseshoe shape, whilst the H-field is confined to a region surrounding a thin piece of conductor in the middle. This behaviour is reminiscent of the LC resonator of §3.2, whereby the horseshoe shaped outer dielectric acts as the capacitor storing E-field energy, and the wire in the middle acts as an inductor storing the H-field energy. Clearly, having the inductor between the plates of the capacitor is what lends this design its compactness. We also observed from our simulations that the E and H field intensities were not perfectly (ie, 45°) out of phase. The author suggests that this may indicate further scope for optimising the resonator design.

Figure 4.13 shows the evanescent decay of the fields as we increase the distance from the device surface. The decay is extremely sharp, meaning that coupling of the EM waves to the environment can be avoided by including a thin spacer. In practice, these spacers are already used in ultrasound devices (usually made from medical grade PDMS) to protect the piezoelectric elements from water ingress and damage. However, it is important to note that, for these relatively low frequency (1.4 GHz) devices, the superstrate layer (whose thickness

must be lower than the wavelength of the maximum frequency for detection - see §2.3.2) is not sufficient to provide this EM shielding. We noted early on in our experiments that placing the resonator in close proximity (less than 1 mm away) to water causes the resonance to disappear entirely. The reason for this is analogous to frustrated total internal reflection (FTIR), whereby an evanescent field can still allow the out-coupling of energy by bringing a material of matched refractive index close to the waveguiding material. Despite the gap, energy can still couple out of the device. Similarly, water has a higher electric permittivity for microwaves than the effective permittivity of the slotline or microstrip structures. Instead of being confined to the resonator, energy leaks into the water and is dissipated as heat through molecular motion. This critically damps the resonator, and makes the device ineffective. Since one of the main uses for ultrasound receivers is imaging into biological tissue, and the main constituent of biological tissue is water, care must be taken in the design of MOUR devices such that microwave energy does not leak into the medium being imaged, which would both reduce device sensitivity and potentially cause unacceptable microwave exposure. However, with careful design, the total microwave exposure to the subject, user and bystanders can be kept below background levels.

Figure 4.14 shows the absolute E-field values on-resonance over the surface of the device. We note that the field is not entirely concentrated around the resonator even at resonance. This implies that we may notice some sensing in the input-side impedance matching region of the device. This would result in an undesirable contribution to the overall pitch of the device and increase its directionality [15]. We can counteract this effect trivially by simply masking the area outside of the resonator when applying the superstrate layer.

4.1.2 Equivalence with LC model

For the purposes of understanding the effect of the superstrate layer on the device resonance, we will demonstrate the equivalence of the models involving a length of transmission line with an effective permittivity and an LC resonator. We know from our analysis in §3.2 that changes to the thickness or permittivity superstrate layer affect the effective permittivity of the microstrip on the substrate. Though we do not have fully worked-out model for it, it seems reasonable to assume that the effect also occurs for slotlines. We recall from (4.1) that

$$f_r = \frac{c}{2l_s\sqrt{\varepsilon_e}}. \tag{4.2}$$

In our simple LC model worked out in §3.2, the resonant frequency is given by

$$f_r = \frac{1}{2\pi\sqrt{LC}}, \tag{4.3}$$

These two models are essentially equivalent if we take the capacitor in the LC model to be an ideal parallel plate capacitor governed by the equation

$$C = \frac{\varepsilon_e A}{d} \tag{4.4}$$

where A is the capacitor area and d is the distance between the plates. (4.3) and (4.2) become equivalent if

$$\frac{A}{d} = \frac{l_s^2}{c^2 L\pi^2}. \tag{4.5}$$

Therefore, we can treat the LC model and the slotline resonator equivalently. We will refer interchangeably to the device modulating the capacitance of an LC resonator or the effective permitivity of a coupled slotline.

4.2 Q and Sensitivity

The Q-factor and sensitivity of the device are intimately linked. To analyse this relationship further, we can build a simple analytic model of the device resonance using a Lorentzian curve parameterised by Q. Q can then be determined from simulation or directly through measurement using a network analyser. Our 'model' resonator has the equation

$$P_{\text{out}}(f) = \frac{P_{\text{in}}}{1+4Q^2(f/f_r-1)^2}, \tag{4.6}$$

where P_{out} and P_{in} are the output and input powers respectively, Q is the device Q-factor and f_r is the resonance. For an optimal sensor, the device will be tuned to the point of greatest slope, which is at

$$f_{\text{tune}} = \frac{-\sqrt{3}f_r + 6f_rQ}{6Q}. \tag{4.7}$$

Taking the derivative of (4.6) and substituting in f_{tune} for f, we find the maximum slope is

$$\frac{1}{P_{\text{in}}}\left(\frac{\partial P_{\text{out}}}{\partial f}\right)_{\text{max}} = \frac{3\sqrt{3}Q}{4f_r}. \tag{4.8}$$

Recall from §3.2 that the overall sensitivity of the device (if we are directly measuring the microwave power from the system) is given by

$$M = \frac{\mathrm{d}P_{\text{out}}}{\mathrm{d}\phi} = 2\frac{\mathrm{d}|S_{21}|}{\mathrm{d}\phi}|S_{21}|P_{\text{in}}, \tag{4.9}$$

where ϕ is some unspecified real-world variable we are trying to measure. We know from (4.3) and (4.2) that

$$\frac{\mathrm{d}f_r}{\mathrm{d}\phi} = -k\frac{\mathrm{d}\varepsilon_e}{\mathrm{d}\phi}\varepsilon_e^{-3/2} \tag{4.10}$$

where

$$k = \frac{c}{4l_s} = \frac{1}{4\pi}\sqrt{\frac{d}{AL}}. \tag{4.11}$$

Therefore,

$$M = 2\frac{\mathrm{d}|S_{21}|}{\mathrm{d}f_r}\frac{\mathrm{d}f_r}{\mathrm{d}\phi}|S_{21}|P_{\text{in}} \tag{4.12}$$

assuming that

$$\left(\frac{\partial|S_{21}|}{\partial\phi}\right)_{f_r} = 0. \tag{4.13}$$

For large f_r, we can assume that

$$\frac{\mathrm{d}|S_{21}|}{\mathrm{d}f_r} \simeq -\frac{\mathrm{d}|S_{21}|}{\mathrm{d}f}. \tag{4.14}$$

Therefore, for sufficiently large f, the maximum sensitivity M_{max} is approximately

$$M_{\text{max}} = -\frac{3\sqrt{3}Q}{2f_r}\frac{\mathrm{d}f_r}{\mathrm{d}\phi}|S_{21}|P_{\text{in}}. \tag{4.15}$$

Finally, by substituting (4.10) into (4.15), we arrive at

$$M_{\text{max}} = k\frac{3\sqrt{3}Q}{2f_r\varepsilon_e^{3/2}}\frac{\mathrm{d}\varepsilon_e}{\mathrm{d}\phi}|S_{21}|P_{\text{in}}. \tag{4.16}$$

4.2.1 Static Pressure Sensor

If we were only interested in building a static pressure sensor, we would replace ϕ by the static pressure variable p. This setup is shown in Figure 4.15. We recall from (3.33) that

$$\varepsilon_e(p) = \varepsilon(d(p), H(p), \varepsilon_{r1}(p), \varepsilon_{r2}(p), C_0(p)), \tag{4.17}$$

therefore

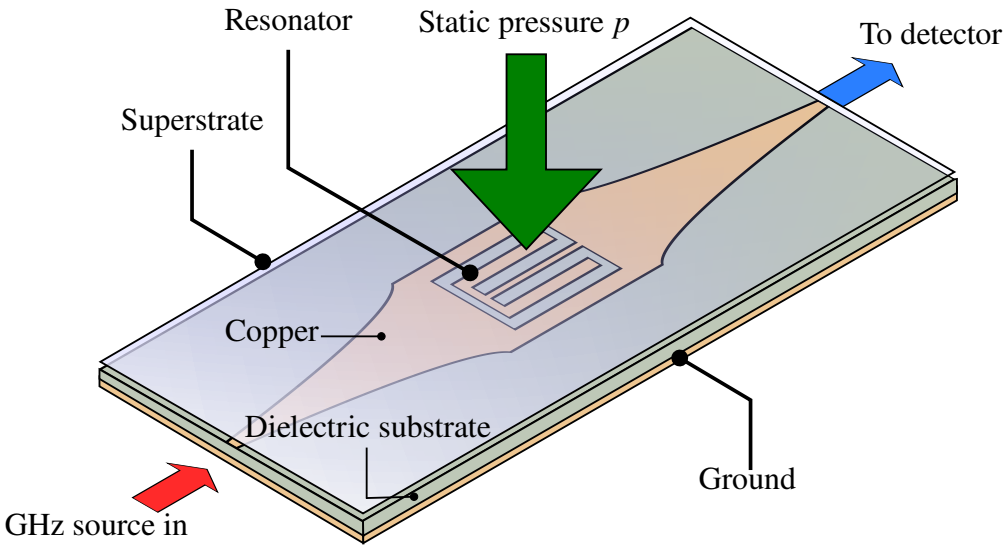

Figure 4.15: Illustration of the static pressure sensor setup

$$\frac{\mathrm{d}\varepsilon_e}{\mathrm{d}p} = \frac{\partial\varepsilon_e}{\partial d}\frac{\partial d}{\partial p} + \frac{\partial\varepsilon_e}{\partial H}\frac{\partial H}{\partial p} + \frac{\partial\varepsilon_e}{\partial\varepsilon_{r1}}\frac{\partial\varepsilon_{r1}}{\partial p} + \frac{\partial\varepsilon_e}{\partial\varepsilon_{r2}}\frac{\partial\varepsilon_{r2}}{\partial p} + \frac{\partial\varepsilon_e}{\partial C_0}\frac{\partial C_0}{\partial p}, \quad (4.18)$$

where the variable definitions are given by Figure 3.10. We will assume that

$$\left(\frac{\partial H}{\partial p}\right) = \left(\frac{\partial\varepsilon_{r1}}{\partial p}\right) = \left(\frac{\partial C_0}{\partial p}\right) = 0, \quad (4.19)$$

ie, we assume the properties of the substrate and the copper remain constant. This is reasonable as long as the substrate is sufficiently rigid and is not allowed to flex. Therefore,

$$\frac{\mathrm{d}\varepsilon_e}{\mathrm{d}p} = \frac{\partial\varepsilon_e}{\partial\varepsilon_{r2}}\frac{\partial\varepsilon_{r2}}{\partial p} + \frac{\partial\varepsilon_e}{\partial d}\frac{\partial d}{\partial p}. \quad (4.20)$$

(4.16) therefore becomes

$$M_{\max} = k\frac{3\sqrt{3}Q}{2f_r\varepsilon_e^{3/2}}\left(\frac{\partial\varepsilon_e}{\partial\varepsilon_{r2}}\frac{\partial\varepsilon_{r2}}{\partial p} + \frac{\partial\varepsilon_e}{\partial d}\frac{\partial d}{\partial p}\right)|S_{21}|P_{\text{in}}. \quad (4.21)$$

4.2.2 Acoustic Sensor

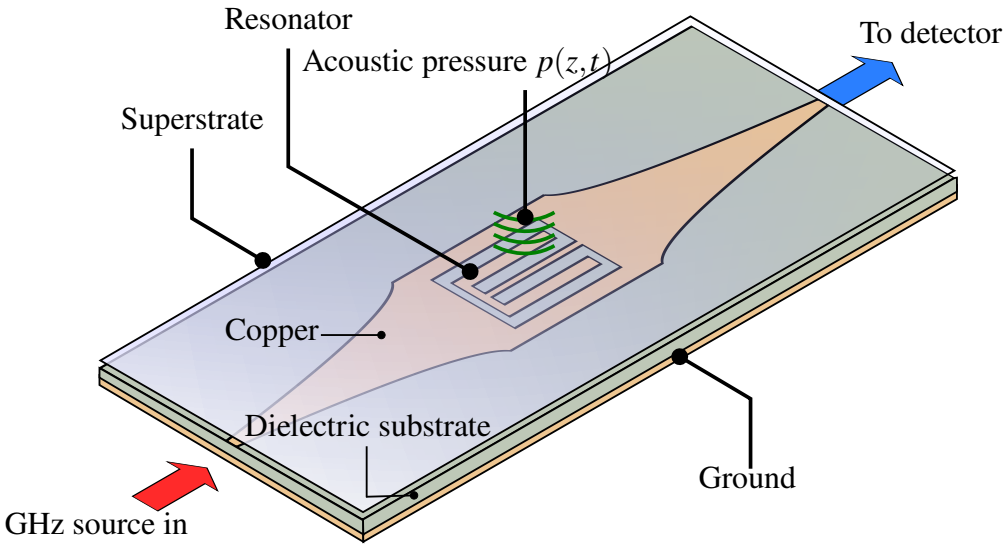

Figure 4.16: Illustration of the acoustic pressure sensor setup

For an acoustic sensor (Figure 4.16), pressure becomes a function of time and space: $p \to p(z,t)$. We know from the linearised acoustic wave equation given in §2.2.1 that its solutions take the form $p(z,t) = p(z)p(t)$. The equation relating d, the thickness of the superstrate, and p, assuming the substrate is effectively incompressible, is given by

$$d = d_0 + p(t)\int_0^{d_0} \frac{p(z)}{E}\mathrm{d}z \tag{4.22}$$

where d_0 is the un-stressed thickness of the superstrate layer and E is the Young's modulus of the superstrate material. Similarly, for ε_{r2} [14],

$$\varepsilon_{r2}^2 = \varepsilon_{r2,0}^2 + \kappa p(t)\int_0^{d_0} \frac{p(z)}{Ed_0}\mathrm{d}z \tag{4.23}$$

where κ is the strain-optic coefficient aligned along the z-axis and $\varepsilon_{r2,0}$ is the un-stressed permittivity of the superstrate material.[1]

[1] This assumes the mean-field approximation holds for the superstrate permittivity.

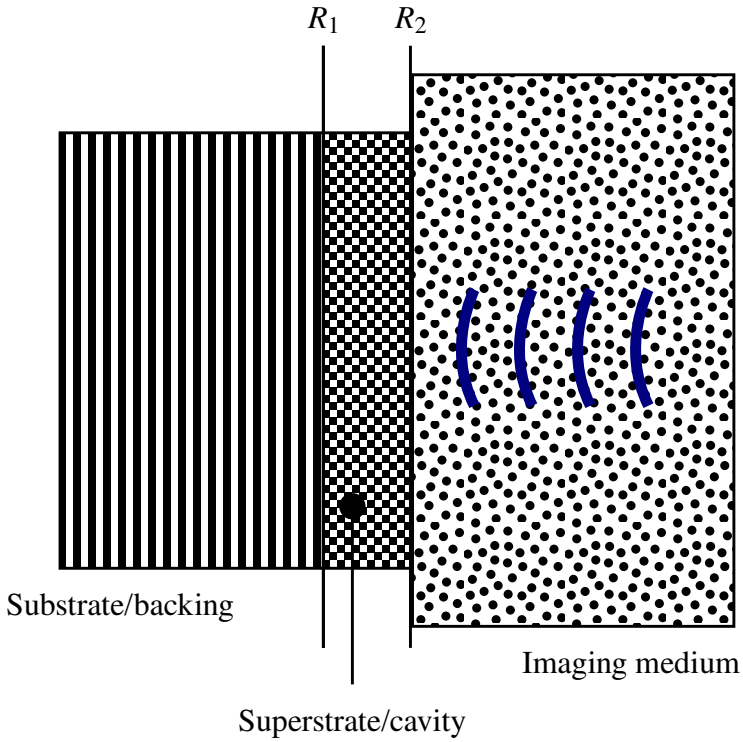

Figure 4.17: Illustration of the acoustic cavity. R_1, R_2 are reflection coefficients

To find $p(z)$, we need to consider the acoustic boundary conditions. Essentially, we are solving the same 1D system as we did in §2.3.2, only without the electrical part—the right-hand side of the transformer in Figure 2.3. We wish to treat the substrate as a perfectly rigid acoustic backing: ie, having an infinite acoustic impedance. The definition of acoustic impedance is

$$Z = F/v, \tag{4.24}$$

where F is the force and v is the particle velocity. An acoustic reflection occurs anywhere that there is a mismatch in acoustic impedance. For our substrate-superstrate-medium structure, the reflection coefficients, shown in Figure 4.17, are given by [16]

$$R_{ij} = \frac{Z_j - Z_i}{Z_j + Z_i}. \tag{4.25}$$

The superstrate layer acts as a resonant cavity. We saw in §2.3.2 how to calculate the behaviour of such cavities using acoustic transmission line theory. However, this theory only approximates the behaviour of a resonant cavity—it does not account for losses. While it is trivial to add continuous losses—those losses which occur along the whole length of the transmission line—it is less obvious how to account for discrete losses, which occur at the reflective boundaries. Although this has been dealt with approximately in the acoustic case in work on optical ultrasound sensors [17] (the contributions of up to 5 reflections are considered for a few limiting cases), the author has not come across an exact derivation. In what follows, we make use of some recent work on optical Fabry-Perot cavities [18] to derive an expression which accounts for an infinite number of reflections with losses at either cavity boundary.

We can treat the acoustic pressure field $p(z;t)$ within the cavity as a damped harmonic oscillator with a characteristic decay time τ. Each reflection reduces the pressure field by $1-R$. The time it takes for a sound wave to do a round trip of the cavity is

$$t_{RT} = \frac{2d_0}{c}, \tag{4.26}$$

where c is the speed of sound inside the cavity and we take the thickness of the cavity to be its time-average d_0. If, after each round-trip, the field is reduced by $1-R$, then the field inside the cavity decays along the curve $p = p_0 e^{-t/\tau}$ where

$$1 - e^{-t_{RT}/\tau} = 1 - R, \tag{4.27}$$

therefore,

$$\tau = -t_{RT} / \ln(R). \tag{4.28}$$

It follows that if there are more than one partially-reflecting surfaces through which sound energy can be coupled out, then

$$\tau = -t_{RT} / \left(\sum_i \ln(R_i) \right). \tag{4.29}$$

Assume the superstrate layer is originally at rest (ie, the pressure field inside it is zero). A pulse of ultrasound energy of frequency ω is then incident at time $t = 0$. The time-varying part of the pressure field inside the superstrate layer is therefore given by

$$p(t) = \begin{cases} 0 & t < 0 \\ p_0 e^{i\omega t} e^{-t/\tau} & t \geq 0. \end{cases} \tag{4.30}$$

The distribution of frequencies inside the superstrate layer is therefore given by the Fourier transform of $p(t)$:

$$\begin{aligned} \tilde{p}(\omega') &= \frac{1}{\sqrt{2\pi}} \int_{-\infty}^{\infty} p(t) e^{-i\omega' t} \\ &= \frac{1}{\sqrt{2\pi}} \int_{0}^{\infty} p_0 e^{[-1/\tau + i(\omega - \omega')]t} \mathrm{d}\omega' \\ &= \frac{1}{\sqrt{2\pi}} \frac{p_0}{1/\tau + i(\omega' - \omega)}. \end{aligned} \tag{4.31}$$

The spatial distribution of pressure waves inside the superstrate layer is given by

$$p_m(z) = \frac{1}{\sqrt{2\pi}} \int_{-\infty}^{\infty} \tilde{p}_m(k') e^{ik'z} \mathrm{d}k' \tag{4.32}$$

where $\tilde{p}_m(k')$ is the k-space representation of the pressure field for a particular vibration mode m. To find the complete 1D pressure field

$p(z)$, we need to consider the superposition of *all* possible vibrational modes, weighted by their density in phase space. Therefore,

$$\begin{aligned} p(z) &= \sum_{\text{modes}} D_m p_m(z) \\ &= \frac{1}{\sqrt{2\pi}} \sum_{\text{modes}} D_m \int_{-\infty}^{\infty} \tilde{p}_m(k') e^{ik'z} \mathrm{d}k', \end{aligned} \tag{4.33}$$

where D_m is the weighting for mode m. In a general multidimensional system, a given mode might have a spectrum of possible k-vectors associated with it. But inside our homogeneous, 1D superstrate, the modes are harmonic 1D vibrations of the form $\exp(ikz)$. The spectra of these modes in k-space are therefore given by

$$p_m(k) = \delta(k - k_m), \tag{4.34}$$

where $\delta(...)$ is the Dirac delta function, and k_m is the wavenumber associated with the mode m. Therefore, we can re-write (4.33) as

$$p(z) = \frac{1}{\sqrt{2\pi}} \sum_{\text{modes}} D_m \int_{-\infty}^{\infty} \delta(k' - k_m) e^{ik'z} \mathrm{d}k'. \tag{4.35}$$

We are now in a position to use $\tilde{p}(\omega')$, the distribution of frequencies inside the superstrate layer, to evaluate $p(z)$. We replace our summation over discrete modes m with weighting D_m with an integral over the contiuum of modes ω' with weighting $\tilde{p}(\omega')\mathrm{d}\omega$, meaning (4.35) becomes

$$\begin{aligned} p(z) &= \frac{1}{\sqrt{2\pi}} \int_{-\infty}^{\infty} \int_{-\infty}^{\infty} \tilde{p}(\omega') \delta[k' - k(\omega')] e^{ik'z} \mathrm{d}k' \mathrm{d}\omega' \\ &= \frac{1}{\sqrt{2\pi}} \int_{-\infty}^{\infty} \int_{-\infty}^{\infty} \tilde{p}(\omega') \delta(k' - \omega'/c) e^{ik'z} \mathrm{d}k' \mathrm{d}\omega' \\ &= \frac{1}{\sqrt{2\pi}} \int_{-\infty}^{\infty} \tilde{p}(\omega') e^{i\omega' z/c} \mathrm{d}\omega', \end{aligned} \tag{4.36}$$

where, from the dispersion relation, we have used the fact that $k' = \omega'/c$ where c is the speed of sound inside the superstrate. Then, by substituting (4.31) into (4.36), we arrive at

$$p(z) = \frac{p_0}{2\pi}\int_{-\infty}^{\infty} \frac{e^{i\omega' z/c}}{1/\tau + i(\omega' - \omega)} \mathrm{d}\omega'. \tag{4.37}$$

Assuming that $\tau \geq 0, c > 0$ and $\omega \geq 0$, this integral evaluates to

$$p(z) = p_0 \exp\left[\frac{z(i\tau\omega - 1)}{c\tau}\right]. \tag{4.38}$$

Finally, we can substitute (4.38) into (4.22) to find d:

$$d = d_0 + p(t)\frac{2d_0 p_0 c}{E}\frac{\exp(id_0\omega/c)\sqrt{R_1 R_2}}{2id_0\omega + c[\ln(R_1) + \ln(R_2)]}, \tag{4.39}$$

where we have substituted in (4.29) for τ using reflectivities $R_i = \{R_1, R_2\}$.

Now we can look at some limiting cases. In each scenario we will implicitly take the real part of d, since the imaginary part has no physical significance.

Case 1: $R_1 = 1, R_2 = 1$

This corresponds to the case where the cavity is surrounded on both sides by a hard boundary. In this scenario, the deflection is given by

$$d = d_0 + p(t)\frac{p_0 c}{E\omega}\sin(d_0\omega/c). \tag{4.40}$$

Case 2: $R_1 = 1, R_2 = 0$

This corresponds to the case where the cavity is bounded on one side by a hard boundary, and has no reflection at the other side. Our model breaks down here: because all of the energy must have dissipated after one round trip, τ is indeterminate. Since in this situation there is no

boundary condition on one of the faces, we can compute d by simply integrating the free-space acoustic wave from perfectly-reflecting substrate face up to d_0. At a perfectly reflecting boundary the pressure exherted is $2p_0$ [16], therefore

$$\begin{aligned} d &= d_0 + p_0 p(t) \frac{2}{E} \int_0^{d_0} \cos(kz) \mathrm{d}z \\ &= d_0 + p_0 p(t) \frac{2}{kE} \sin(d_0 k) \\ &= d_0 + p_0 p(t) \frac{2c}{E\omega} \sin(d_0 \omega / c), \end{aligned} \tag{4.41}$$

which is $2\times$ greater than in Case 1.

Case 3: $R_1 = -1, R_2 = 1$

This corresponds to a free, perfectly reflecting boundary on one side and a hard boundary on the other. The equation is:

$$d = d_0 + p(t) \frac{2p_0 d_0 c}{E(c\pi + 2d_0\omega)} \cos(d_0\omega/c). \tag{4.42}$$

Case 4: $R_1 = -1, R_2 = -1$

This corresponds to two free but perfectly reflecting boundaries. In this scenario:

$$d = d_0 - p(t) \frac{p_0 d_0 c}{E\omega(c\pi + 2d_0\omega)} \sin(d_0\omega/c), \tag{4.43}$$

where we note the sign change compared to the other scenarios.

Plotting all Intermediate Cases

Figure 4.18 shows response curves for 400 different combinations of values of R_1 and R_2 between -1 and 1. The parameters used were $d_0 = 1\,\mathrm{mm}, c = 1000\,\mathrm{m/s}$ and $E = 360\,\mathrm{kPa}$. We note the 'bunching' of curves into three distinct cases depending on the signs of R_1 and R_2: both positive; positive and negative; and both negative, corresponging to cases 1, 2 and 4 respectively. These cases in turn may be seen to

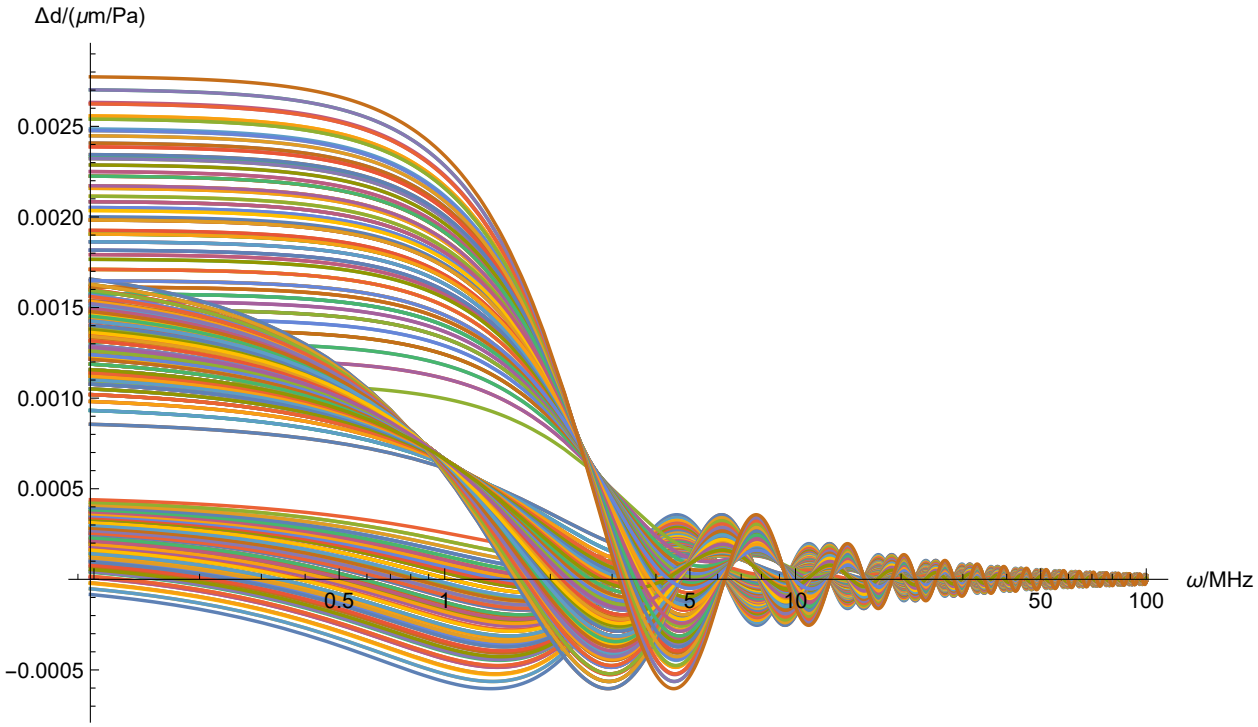

Figure 4.18: Plot showing all values of R_1, R_2 between 1 and -1

correspond to the top, middle and bottom bunches of curves respectively. This 'bunching' property can be seen more clearly in Figure 4.19, where the three cases correspond to three distinct but overlapping regions in the complex plane.

4.3 Signal to Noise

Although the noise characteristics of acoustic receivers have been well considered in previous work [19], our devices operate on a different noise model and therefore require seperate consideration. There are four sources of noise we must consider for MOURS: (1) thermal acoustic noise; (2) Johnson-Nyquist noise; (3) diode shot noise; (4) source phase noise. 1 and 2 are well considered in the hydrophone literature [20], but there is an important difference regarding 1. Whereas in conventional transducers, the real part of the electronic impedance of the transducer depends on the ultrasound frequency [21], in MOURs, the electronic impedance is totally independent of the ultrasound fre-

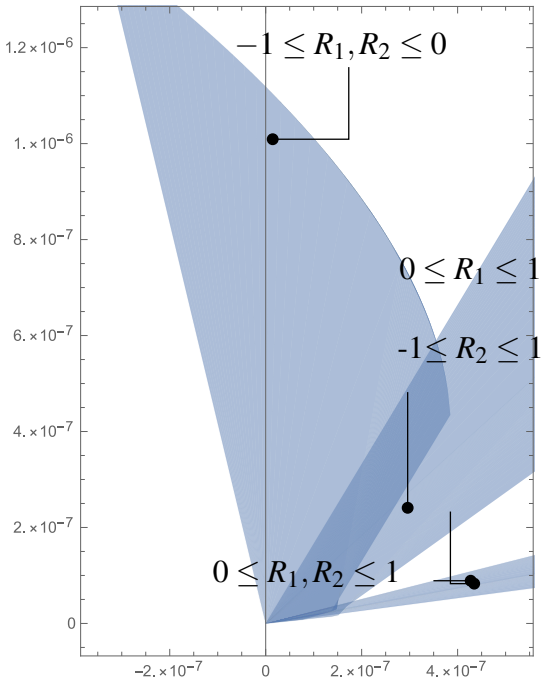

Figure 4.19: Argand diagram of (4.39) with $\omega = 0.5\,\text{MHz}$ showing the three distinct regions corresponding to the three cases and the three bunches of curves in Figure 4.18

quency, as we saw in §3.2. This means that the Thévenin equivalent circuit of [19], which represents both thermal acoustic noise and the Johnson-Nyquist noise as resulting from a single real impedance R_H, is not directly applicable to MOURs.

Our noise model is shown in Figure 4.20. Expressions for our four noise sources as as follows (we take noise to be defined per unit bandwidth of ultrasound):

$$\begin{aligned}
\bar{e}_T^2 &= 2M\rho c\omega_a^2 k_B T && \text{Thermal noise from acoustic medium} \\
\bar{e}_{\text{JN}}^2 &= 4k_B T\Re[\tilde{Z}_{21}] && \text{Johnson-Nyquist noise from the resonator} \\
\bar{e}_{\text{S}}^2 &= 2q_e S_{21}\sqrt{P_{\text{in}}}/Z_L && \text{Shot noise of the envelope detector} \\
\bar{e}_P(\omega_s,\omega_a)^2 & && \text{Phase noise from the source}
\end{aligned} \tag{4.44}$$

where T is the ambient temperature, k_B is Boltzmann's constant, q_e is

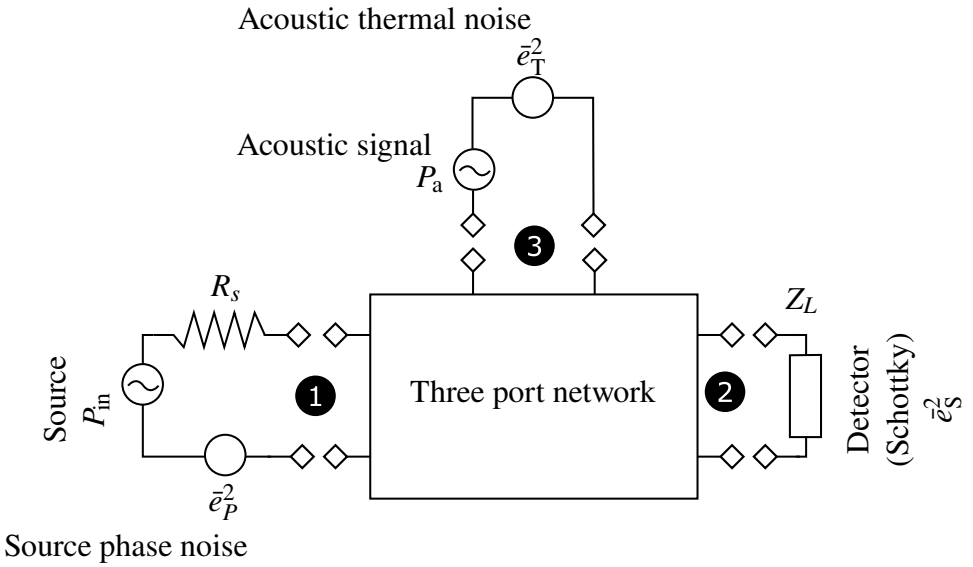

Figure 4.20: Schematic of the MOUR noise model, with port numbers given in black circles

the fundamental electric charge, ω_s and ω_a are the angular frequencies of the source and acoustic signal respectively, and all other quantities are given by their definition in Figure 4.20 (including S and Z-values). We also assume in this simple model that $S_{31} = M$ and $S_{13} = S_{32} = S_{23} = 0$.

Therefore, the SNR of the receiver system per unit bandwidth is given by

$$\mathrm{SNR} = \frac{MP_\mathrm{a}}{2M\rho c\omega_a^2 k_B T + 4k_B T\Re[\tilde{Z}_{21}] + 2q_e S_{21}\sqrt{P_\mathrm{in}}/Z_L + \bar{e}_P(\omega_s,\omega_a)}. \tag{4.45}$$

There are some important things to note from this analysis. Firstly, we see that the shot noise contribution is dominated by the unmodulated microwave source power P_in. This has implications for the

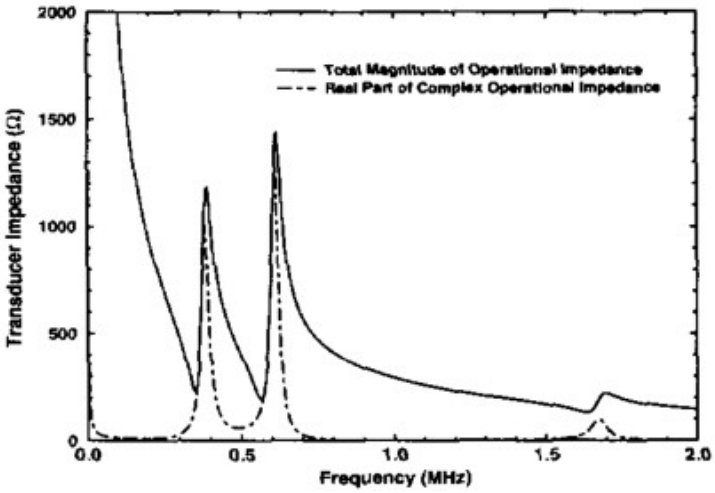

Figure 4.21: Plot showing the measured impedance characteristics of a ceramic-epoxy piezoelectric transducer operating in air (reproduced from [22])

overall SNR: in fact, we found in our experiments that this form of shot noise dominated the signal, but that it could be cancelled out using a homodyne detection system. Secondly, we note that the Johnson-Nyquist noise contributions do not depend on P_{in}, but since M *does* depend on P_{in}, P_{in} may be increased to overcome $\bar{e}_T$ until shot noise dominates. With regards to the source phase noise $\bar{e}_P(\omega_s, \omega_a)^2$, this could limit the ability to detect low-frequency ultrasound signals in direct detection or heterodyne systems, but can be eliminated in phase-matched homodyne systems. Finally, we note that the Johnson-Nyquist noise is dependent on Z_{21}, which is very high at the resonance but low elsewhere. The tilde over $\tilde{Z}_{21}$ in (4.44) indicates that the impedance is an average defined by

$$\tilde{Z}_{21} = \frac{1}{f_{\max}} \int_0^{f_{\max}} Z_{21}(\omega) \mathrm{d}\omega \tag{4.46}$$

where $f_{\max}$ is the maximum frequency of the measurement band. As we saw in §3.2, a resonant system can become purely resistive at the resonant frequency. In a traditional piezoelectric ultrasound receiver, this resonance occurs within the acoustic band of interest, as shown in

Figure 4.21. But in MOURs, the resonance occurs in the microwave band. Therefore, the majority of the Johnson-Nyquist noise is located *outside* the signal band.

Therefore, we tentatively conclude that the system is overall shot-noise limited, since phase noise can be cancelled using a homodyne receiver system, and Johnson-Nyquist noise is primarily out-of-band for the high-frequency components of the circuit (once the signal has been converted to the baseband, Johnson-Nyquist noise comes into play again). Furthermore, we note that M is proportional to P_{in} (see (3.8) and recall that $P_{\text{in}} = |a_1|^2$). If shot noise is the limiting factor, then

$$\begin{aligned} \text{SNR} &= \frac{2\frac{\partial|S_{21}|}{\partial p}P_{\text{in}}P_a}{2q_eS_{21}\sqrt{P_{\text{in}}}/Z_L} \\ &= \frac{2Z_L\frac{\partial|S_{21}|}{\partial p}\sqrt{P_{\text{in}}}P_a}{2q_eS_{21}} \end{aligned} \tag{4.47}$$

where p is the incident pressure variable. Therefore it appears we can increase the SNR indefinitely by simply increasing P_{in}, up to any thermal or power limits which may be determined for the specific application in question.

One final note on noise: in the above we have considered only thermal or intrinsic sources of noise. Noise can also originate from nearby equipment, unwanted acoustic echoes, diffraction effects and cross-talk between elements. We discussed briefly how inter-element cross-talk can be eliminated using MOURs in §3.4. However, MOUR elements are also evidently robust to sources of electromagnetic interference from other sources, since any in-band interference is removed at the final bandpass filtering stage.

4.4 Superstrate Considerations

We have only very briefly discussed the properties we would like for our superstrate layer. We know that we want it to have a good acoustic impedance match with the imaging medium, and that it should be easy to deposit in thin layers. However, recall (4.16) (reproduced below):

$$M_{\max} = k\frac{3\sqrt{3}Q}{2f_r\varepsilon_e^{3/2}}\left(\frac{\partial\varepsilon_e}{\partial\varepsilon_{r2}}\frac{\partial\varepsilon_{r2}}{\partial p}+\frac{\partial\varepsilon_e}{\partial d}\frac{\partial d}{\partial p}\right)P_{\text{in}}.$$

The term $\frac{\partial\varepsilon_{r2}}{\partial p}$ implies that the sensitivity M might be enhanced by the material having a large acousto-optic coefficient. We feel that it is reasonable to assume that such an effect exists for $\varepsilon(\omega)$ where ω is in the microwave range of frequencies (ie, above DC but below optical frequencies), since there exists both the piezoelectric effect, which relates the DC value of ε to strain, and the strain-optic effect, which relates the optical-frequency value of ε to strain.

We have not investigated this area in detail, but a review on tuneable microwave materials [23] indicates that changes in the Curie temperature of materials, which can be induced by strain in ferroelectrics [24], modifies the microwave properties of certain materials. A more general theoretical treatment is found in [14]. One potential candidate material for our device is PVDF, since it automatically satisfies the acoutic requirements of our devices, while also possibly enhancing their sensitivity due to its strong ferroelectric-like behaviour [25]. Due to difficulties in depositing $\beta-$phase PVDF and lack of availability of PVDF-TrFe in our lab [26], we were unable to use this material in our experiments.

References

[1] U. Tata et al. “Exploiting a Patch Antenna for Strain Measurements”. In: *Measurement Science and Technology* 20.1 (2009), p. 015201. issn: 0957-0233. doi: 10.1088/0957-0233/20/1/015201. url: http://stacks.iop.org/0957-0233/20/i=1/a=015201 (visited on 03/21/2018).

[2] J. W. Sanders, J. Yao, and H. Huang. “Microstrip Patch Antenna Temperature Sensor”. In: *IEEE Sensors Journal* 15.9 (Sept. 2015), pp. 5312–5319. issn: 1530-437X. doi: 10.1109/JSEN.2015.2437884.

[3] J. B. Pendry, L. Martín-Moreno, and F. J. Garcia-Vidal. “Mimicking Surface Plasmons with Structured Surfaces”. In: *Science* 305.5685 (Aug. 6, 2004), pp. 847–848. issn: 0036-8075, 1095-9203. doi: 10.1126/science.1098999. pmid: 15247438. url: http://science.sciencemag.org/content/305/5685/847 (visited on 07/24/2017).

[4] Xu Chen and Wenhui Fan. “Ultrasensitive Terahertz Metamaterial Sensor Based on Spoof Surface Plasmon”. In: *Scientific Reports* 7.1 (May 18, 2017), p. 2092. issn: 2045-2322. doi: 10.1038/s41598-017-01781-6. url: https://www.nature.com/articles/s41598-017-01781-6 (visited on 07/24/2017).

[5] Binghao Ng et al. “Spoof Plasmon Surfaces: A Novel Platform for THz Sensing”. In: *Advanced Optical Materials* 1.8 (Aug. 1, 2013), pp. 543–548. issn: 2195-1071. doi: 10.1002/adom.201300146. url: http://onlinelibrary.wiley.com/doi/10.1002/adom.201300146/abstract (visited on 07/28/2017).

[6] Mikhail A. Kats et al. “Spoof Plasmon Analogue of Metal-Insulator-Metal Waveguides”. In: *Optics Express* 19.16 (Aug. 1, 2011), pp. 14860–14870. issn: 1094-4087. doi: 10.1364/OE.19.014860. url: https://www.osapublishing.org/oe/abstract.cfm?uri=oe-19-16-14860 (visited on 02/11/2020).

[7] James Seddon. “Design of a Photonic Enabled Lab-on-Chip for Spectroscopy and Sensing in the Terahertz Domain”. Doctoral. UCL (University College London), June 28, 2019. 189 pp. url: https://discovery.ucl.ac.uk/id/eprint/10076846/ (visited on 02/11/2020).

[8] Yong Jin Zhou, Qian Xun Xiao, and Bao Jia Yang. “Spoof Localized Surface Plasmons on Ultrathin Textured MIM Ring Resonator with Enhanced Resonances”. In: *Scientific Reports* 5 (Sept. 30, 2015), srep14819. issn: 2045-2322. doi: 10.1038/srep14819. url: https://www.nature.com/articles/srep14819 (visited on 07/24/2017).

[9] Dongsheng La et al. “A Novel Compact Bandstop Filter Using Defected Microstrip Structure”. In: *Microwave and Optical Technology Letters* 53.2 (2011), pp. 433–435. issn: 1098-2760. doi: 10.1002/mop.25708. url: https://onlinelibrary.wiley.com/doi/abs/10.1002/mop.25708 (visited on 02/13/2020).

[10] Huansheng Ning et al. “Design of Planar Dual and Triple Narrow-Band Bandstop Filters with Independently Controlled Stopbands and Improved Spurious Response”. In: *Progress In Electromagnetics Research* 131 (2012), pp. 259–274. issn: 1070-4698. doi: 10.2528/PIER12072109. url: http://www.jpier.org/PIER/pier.php?paper=12072109 (visited on 06/26/2018).

[11] Jun Wang et al. “A Compact Narrow-Band Bandstop Filter Using Spiral-Shaped Defected Microstrip Structure”. In: *Radioengineering* 23.1 (2014), pp. 209–213.

[12] Duk-Jae Woo et al. “Novel U-Slot and V-Slot DGSs for Bandstop Filter with Improved Q Factor”. In: *IEEE Transactions on Microwave Theory and Techniques* 54.6 (June 2006), pp. 2840–2847. issn: 1557-9670. doi: 10.1109/TMTT.2006.875450.

[13] James A. Guggenheim et al. “Ultrasensitive Plano-Concave Optical Microresonators for Ultrasound Sensing”. In: *Nature Photonics* 11.11 (Oct. 31, 2017), p. 714. issn: 1749-4893. doi: 10.1038/s41566-017-0027-x. url: https://www.nature.com/articles/s41566-017-0027-x (visited on 11/03/2017).

[14] S. H. Wemple and M. DiDomenico. “Theory of the Elasto-Optic Effect in Nonmetallic Crystals”. In: *Physical Review B* 1.1 (Jan. 1, 1970), pp. 193–202. doi: 10.1103/PhysRevB.1.193. url: https://link.aps.org/doi/10.1103/PhysRevB.1.193 (visited on 07/24/2017).

[15] David G. Shombert, Stephen W. Smith, and Gerald R. Harris. “Angular Response of Miniature Ultrasonic Hydrophones”. In: *Medical Physics* 9.4 (1982), pp. 484–492. issn: 2473-4209. doi: 10.1118/1.595114. url: https:

//aapm.onlinelibrary.wiley.com/doi/abs/10.1118/1.595114 (visited on 08/06/2019).

[16] Richard S. C. Cobbold. *Foundations of Biomedical Ultrasound*. Oxford University Press, Sept. 7, 2006. 844 pp. isbn: 978-0-19-977512-5. Google Books: Hwb5D60vb5IC.

[17] P. C. Beard and T. N. Mills. "Extrinsic Optical-Fiber Ultrasound Sensor Using a Thin Polymer Film as a Low-Finesse Fabry–Perot Interferometer". In: *Applied Optics* 35.4 (Feb. 1, 1996), pp. 663–675. issn: 2155-3165. doi: 10.1364/AO.35.000663. url: https://www.osapublishing.org/abstract.cfm?uri=ao-35-4-663 (visited on 12/15/2017).

[18] Nur Ismail et al. "Fabry-Perot Resonator: Spectral Line Shapes, Generic and Related Airy Distributions, Linewidths, Finesses, and Performance at Low or Frequency-Dependent Reflectivity". In: *Optics Express* 24.15 (July 25, 2016), pp. 16366–16389. issn: 1094-4087. doi: 10.1364/OE.24.016366. url: https://www.osapublishing.org/oe/abstract.cfm?uri=oe-24-15-16366 (visited on 02/25/2020).

[19] J. W. Young. "Optimization of Acoustic Receiver Noise Performance". In: *The Journal of the Acoustical Society of America* 61.6 (June 1, 1977), pp. 1471–1476. issn: 0001-4966. doi: 10.1121/1.381464. url: https://asa.scitation.org/doi/abs/10.1121/1.381464 (visited on 01/08/2020).

[20] C. G. Oakley. "Calculation of Ultrasonic Transducer Signal-to-Noise Ratios Using the KLM Model". In: *IEEE Transactions on Ultrasonics, Ferroelectrics, and Frequency Control* 44.5 (Sept. 1997), pp. 1018–1026. doi: 10.1109/58.655627.

[21] C. S. Desilets, J. D. Fraser, and G. S. Kino. "The Design of Efficient Broad-Band Piezoelectric Transducers". In: *IEEE Transactions on Sonics and Ultrasonics* 25.3 (May 1978), pp. 115–125. issn: 0018-9537. doi: 10.1109/T-SU.1978.31001.

[22] G. Hayward, R.A. Banks, and L.B. Russell. "A Model for Low Noise Design of Ultrasonic Transducers". In: *1995 IEEE Ultrasonics Symposium. Proceedings. An International Symposium*. 1995 IEEE Ultrasonics Symposium. Proceedings. An International Symposium. Vol. 2. Nov. 1995, 971–974 vol.2. doi: 10.1109/ULTSYM.1995.495725.

[23] Aftab Ahmed, Irene A. Goldthorpe, and Amir K. Khandani. “Electrically Tunable Materials for Microwave Applications”. In: *Applied Physics Reviews* 2.1 (Feb. 9, 2015), p. 011302. doi: 10.1063/1.4906255. url: https://aip.scitation.org/doi/full/10.1063/1.4906255 (visited on 06/05/2019).

[24] A.F. Devonshire. “Theory of Ferroelectrics”. In: *Advances in Physics* 3.10 (Apr. 1954), pp. 85–130. issn: 0001-8732, 1460-6976. doi: 10.1080/00018735400101173. url: http://www.tandfonline.com/doi/abs/10.1080/00018735400101173 (visited on 06/19/2019).

[25] B. Lehndorff and D. Schilling. “Microwave Dielectric Behavior of PVDF and VDF-TrFE Copolymer”. In: *Zeitschrift für Physik B Condensed Matter* 91.2 (June 1, 1993), pp. 229–233. issn: 1431-584X. doi: 10.1007/BF01315240. url: https://doi.org/10.1007/BF01315240 (visited on 06/17/2019).

[26] B. Ploss et al. “Pyroelectric Activity of Ferroelectric PT/PVDF-TRFE”. In: *IEEE Transactions on Dielectrics and Electrical Insulation* 7.4 (Aug. 2000), pp. 517–522. issn: 1070-9878. doi: 10.1109/94.868071.

Chapter 5

Proof-of-Concept Experiments

We designed and carried out experiments to test the concept of MOURs. To begin with, we verified and measured the well-established covered-microstrip effect discussed in §3.3. To do this, we manufactured 50 Ω microstrips (width = 600 μm) and the resonator design shown in §4.1 (reproduced in Figure 5.3, manufactured devices can be seen in Figure 5.5, although in this particular experiment the devices were used without the Paralyne coating) on a PCB made from a piece of 0.49 mm Rogers AD1000L Ceramic Laminate connectorised with soldered SMA connectors. We connected the device to a network analyser (EC5071C ENA Series Network Analyser, Agilent Technologies) and successively applied strips of polyimide tape of known thickness. A photo of the experiment is given in Figure 5.1. By monitoring both the phase shift and the change in the resonant frequency, we were able to verify the covered microstrip effect discussed in §3.3. Figure 5.2 shows the results for the microstrip and Figure 5.4 shows the results for the resonator. Each layer of polyimide tape was 60 μm thick and had a width of 12.7 mm. To perform these experiments, the circuit board was screwed into a copper holder to avoid irregularities in the measurments from mechanical bending of the device. The error bars on the plots were calculated from five repeated measurements. In Figure 5.2, we see that the phase change over the length of the microstrip

is greater for higher frequency, as we would expect: the phase change is proportional to the length of microstrip as a multiple of wavelength. In Figure 5.4, the gradient of the phase curves in the left-hand figure are greater than those of the microstrip, demonstrating the large effective transmission line length embodied by the resonator, as our theory suggested in §4.1.2. Furthermore, for the resonator device in Figure 5.4, the phase change per layer of polyimide tape is significantly greater near the resonance (at 1.85 GHz) than it is away from it. This implies that MOUR devices modulate the phase as well as amplitude of the carrier. An ideal receiver system would measure both the in-phase and quadrature components of the carrier modulation and add their powers. The maximum gradient for the change in resonance in Figure 5.4 is $-0.57\,\mathrm{MHz}/\mu\mathrm{m}$.

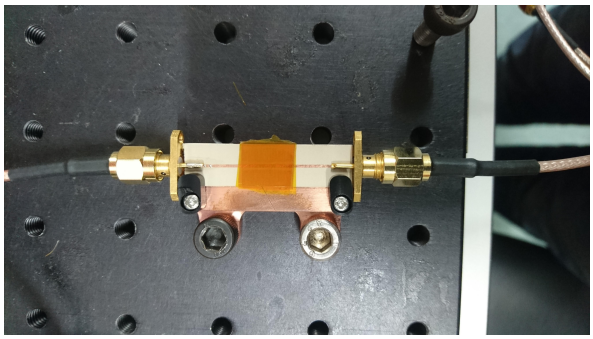

Figure 5.1: Photo of the experimental setup

Following these experiments, we produced a finished MOUR test device by coating one of our PCB resonators with a superstrate layer. For a well-controlled superstrate layer, we coated a small batch of resonator devices with a $20\,\mu$m and $30\,\mu$m layers of Paralyne-C (Figure 5.5). Small regions on either end of the resonators were masked with polyimide tape to allow soldering of connectors. However, we found that the acoustic impedance contrast between Paralyne-C ($Z = 2.75\,\mathrm{MRayl}$ [1]) and the Rogers circuit board (main constituent polytetrafluoroethylene, $Z = 2.97\,\mathrm{MRayl}$, source: nde-ed.org), was not great

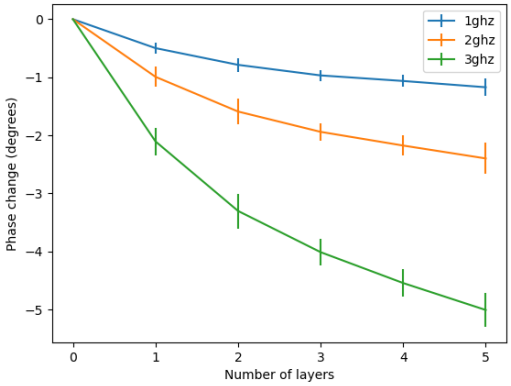

Figure 5.2: Plot of the phase change across a two-port network comprising a microstrip of width 0.6 mm

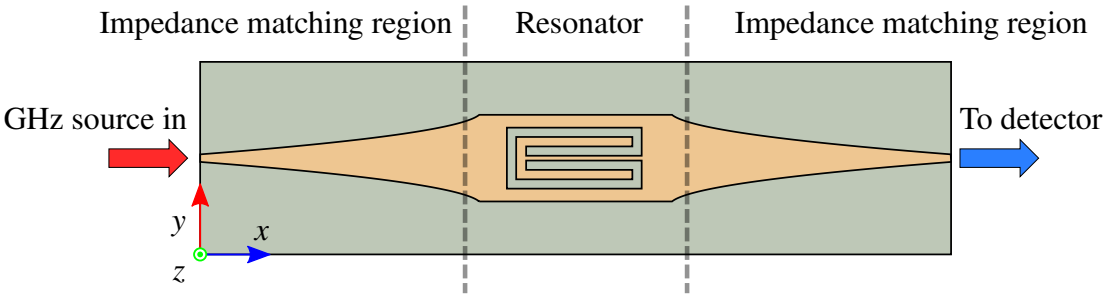

Figure 5.3: Drawing of the MS-DMS with tapered impedance matching regions

enough to enable the cavity response needed for high acoustic sensitivity, as discussed in §4.2.2. Ultimately, we decided to use a latex emulsion ink, either deposited by brush (Liquitex Professional Carbon Black Acrylic Ink) or spray can (Liquitex Professional Spray Paint Carbon Black). We were unable to control precisely the deposition in these cases, however we found qualititively that these devices exhibited better performance than the Paralyne-C equivalents. Qualitatively we did not observe a significant difference between brush and spray paint deposited devices.

To test the MOUR system fully, we devised an experiment which measured the effect of 5 MHz ultrasound pulses on our receiver. In our early experiments, we attempted to visualise the ultrasound sig-

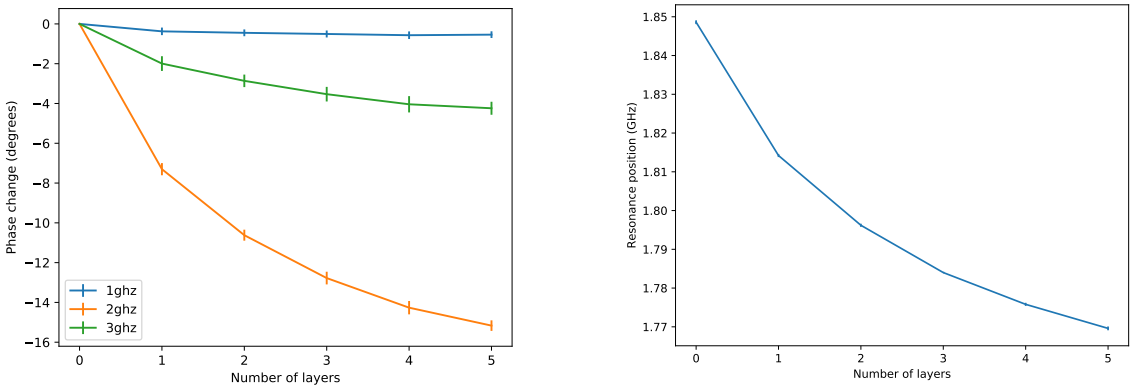

Figure 5.4: Plots of the phase change (left) and resonance shift (right) across two-port networks comprising the resonator

nal on the sidebands of the microwave carrier using a spectrum analyser (E4403B ESA-L Series Spectrum Analyser, Agilent Technologies). To do this, we used a harmonic waveform generator (DG1062 Signal Generator, RIGOL) connected to a 5 MHz single-element PZT ultrasound transducer (13-05040R Ultrasound Transducer, Harsonic), acoustically coupled to the top side of the MOUR resonator.

The resonator is excited near its resonant frequency ω_0. As the superstrate layer is deformed, the amplitude of the signal is modulated

$$E = A\cos(\omega_0 t), \tag{5.1}$$

where E is the electric field component of the microwave signal, ω_0 is its angular frequency, and t is time. The amplitude A is modulated by the ultrasound signal with frequency ω_a and modulation amplitude A_a, giving

$$\begin{aligned} E &= (1 + A_a\cos(\omega_a t))A\cos(\omega_0 t) \\ &= A_a A\cos[(\omega_0 + \omega_a)t]/2 + A_a A\cos[(\omega_0 - \omega_a)t]/2 + A\cos(\omega_0 t). \end{aligned} \tag{5.2}$$

I.e., by looking at the signal E on a spectrum analyser, we should

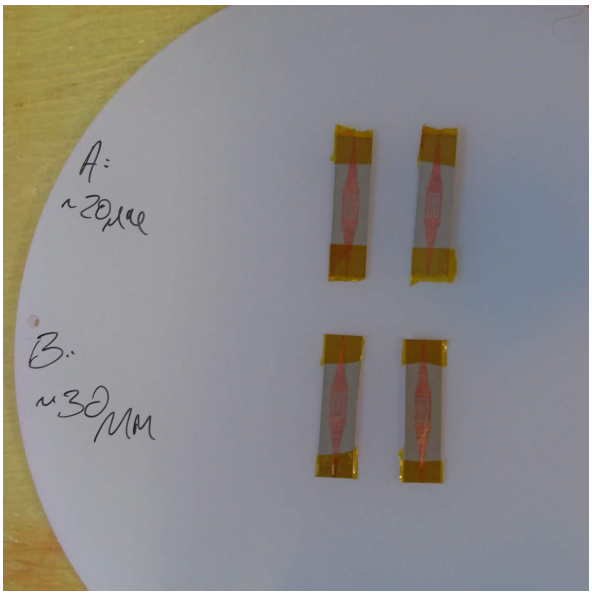

Figure 5.5: Photo of the Paralyne-C-coated devices

be able to detect the carrier at frequency ω_0 with sidebands at $\omega_0 + \omega_a$ and $\omega_0 - \omega_a$. The microwave signal E was generated using a 3 GHz signal generator (N9310A RF Signal Generator, Keysight) and connected to the input of the MOUR device via an SMA connector. This experimental setup can be seen in Figure 5.6. However, despite taking measures to avoid electromagnetic coupling between the low-frequency signal generator and the carrier signal, including high-pass filtering the signal before reaching the spectrum analyser and ensuring the various cables did not cross one another, we were unable to eliminate the interference, and therefore could not claim that the sidebands on the spectrum analyser were caused by an acoustic modulation.

Following this, we redesigned the experiment to work in the time domain rather than frequency domain. This re-design took advantage of the fact that sound waves travel slowly enough to result in a measurable time delay between transmission and reception, even over small distances. This principle is illustrated in Figure 5.7. Since the ultrasound pulse reflects off the sensor back to the transducer, we expect to observe two pulses generated by the pulse transceiver: an initial pulse

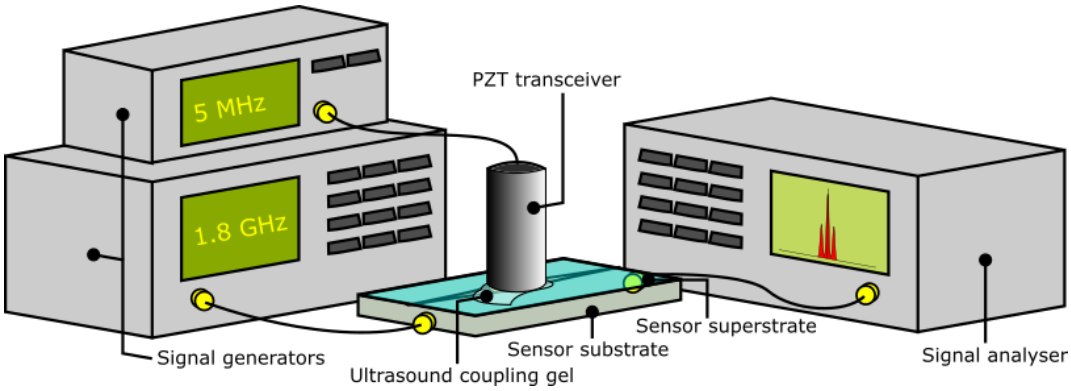

Figure 5.6: Diagram of the sideband measurement experiment

representing the ultrasound being generated at the PZT transducer interface at time $t = 0$; and a second pulse after the time taken to make a round trip, $t = T$. Hence the response of the device should appear as a pulse on the second trace half-way between the two pulses from the PZT transducer, at time $t = T/2$. The signal from the MOUR device should remain at $t = T/2$ even when moving the PZT transducer away from or towards the MOUR device. In this way we could eliminate any doubt regarding the origin of the electrical signal from the receiver.

In collaboration with the department workshop technicians, we designed a holder for our MOUR devices which held the board rigidly in place, provided electromagnetic grounding and allowed a gel-wax spacer of well-defined height to be affixed securely to the top-side of the device. An exploded render of the device holder is shown in Figure 5.8. The base of the holder is made from machined brass and can be screwed down onto an optical bench for stability. The MOUR device is held in place by being sandwiched between the PTFE rings which can be screwed onto the base. Liquid gel-wax, a material commonly used for creating ultrasound phantoms due to its acoustic similarity to biological tissue [2], was melted and poured into the PTFE rings before setting. This provides an acoustic window from the PZT transducer to the MOUR device. Each ring is 5 mm thick, meaning that the total

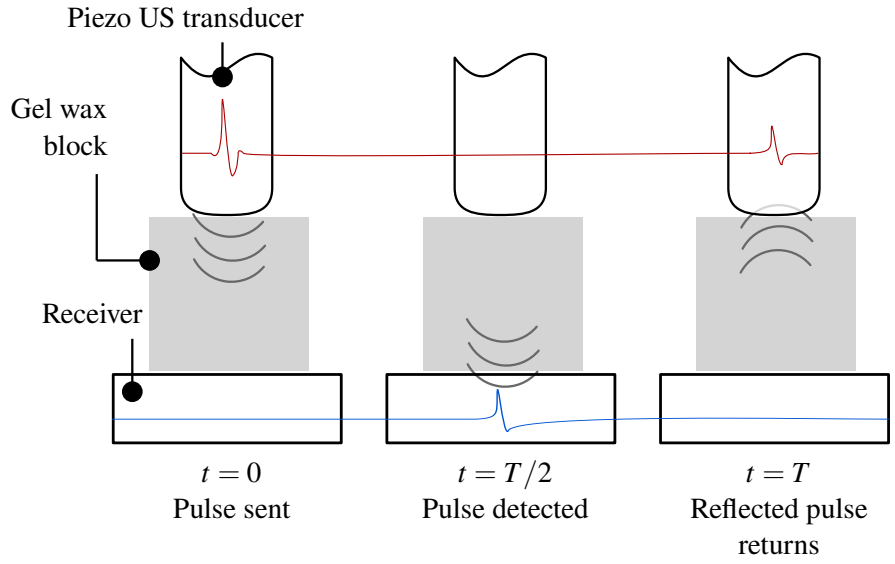

Figure 5.7: Diagram showing the working principle of the time domain experiment. The red trace represents the signal from the transducer, and the blue trace the signal from the receiver

distance between the PZT transducer and the MOUR device is 10 mm.

Before testing with ultrasound sources, the resonance was characterised using the network analyser by measuring the transmission (S_{21}) and reflection (S_{11}) spectra. The position of the resonance was found to be within reasonable error of the FDTD simulation (within 2 %, see Figure 5.9),[1] and the measured Q-factor was about 40. After this initial characterisation, the device was set up in the configuration illustrated by Figure 5.10. Due to the predominance of shot noise and amplifier noise caused by the microwave carrier, we found that it was not possible to detect ultrasound signals using a simple envelope detector setup. Therefore, a homodyne detector was implemented using a power splitter (ANRITSU K241B), phase shifter (ARRA 9426R) and frequency mixer (Mini-Circuits ZX05-C42). Because the same source is used for both the signal and reference oscillators, the phase noise can

[1] The difference in the resonance position here and in the previous polyimide experiments is due to the application of the superstrate layer.

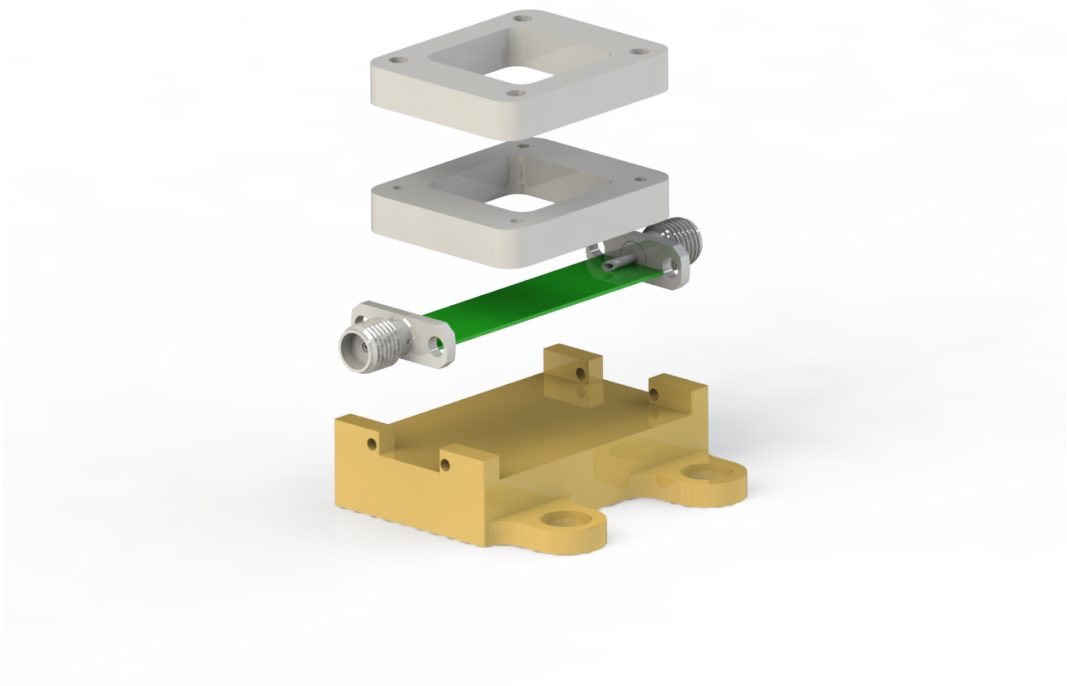

Figure 5.8: Render of the exploded device holder

be entirely cancelled by careful path matching. The output from this was passed through a low-pass filter (passband from DC to 80 MHz) and then an ultrasound receiver with a high gain amplifier (Olympus 5072PR). We then coupled the PZT ultrasound transducer (Harisonic 13-0504-R) to the top side of the gel-wax window using ultrasound coupling gel (Anagel Utrasound Gel, Ana Wiz Ltd.). The piezo transducer was driven by a train of pulses at its resonant frequency (5 MHz) from an ultrasound pulse generator and receiver (Olympus 5077PR).

The microwave source was tuned to near the quadrature (point of greatest slope) of the device's electromagnetic resonance and connected to the system. This tuning was achieved by running the signal from the device through a power detector (Pasternack PE8014) and taking voltage readings whilst changing the frequency of the RF

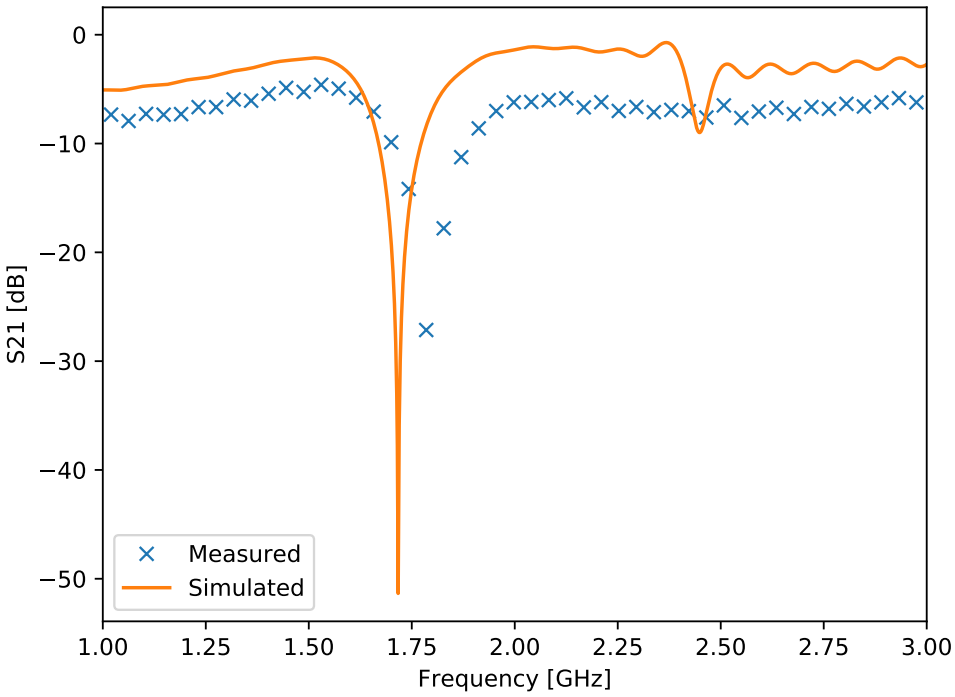

Figure 5.9: Plot of the simulated and measured S_{21} spectra for the MOUR device

source. To detect ultrasound, an oscilloscope (DSO-X 3024A Digital Oscilloscope, Agilent) was externally triggered by the ultrasound pulse generator and traces for both the transducer and receiver were displayed.

5.1 Qualitative Results

The oscilloscope trace from the above experiment is shown in Figure 5.11. There was 1 cm of gel-wax spacer between the PZT transducer and the MOUR device, and the transducer was driven at 400 $V_{pk\text{-}pk}$. We note that, as expected, the pulse appears on the yellow MOUR trace at the midpoint between the pulse being emitted and reflected back to the PZT transducer (green trace). Between the top and bottom acquisitions in Figure 5.11, the transducer was pressed slightly into the gel-wax to reduce the acoustic path length between the PZT trans-

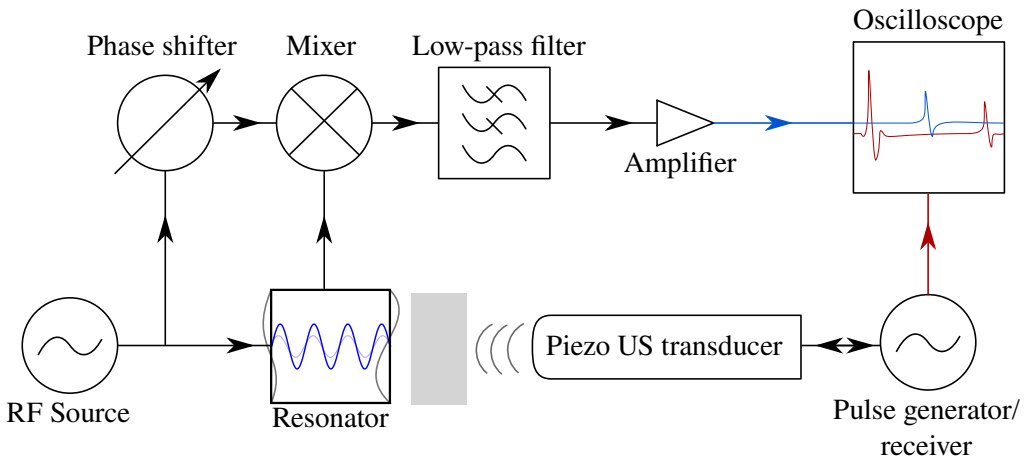

Figure 5.10: Block diagram of the homodyne receiver system used

ducer and the MOUR device. We note that, accordingly, the distance between the two green peeks is reduced, but that the peak on the yellow trace remains halfway between them. In this way we established beyond doubt that the peaks observed on the MOUR trace result from acoustic excitation and not electromagnetic cross-coupling.

There are a few reasons why we are only able to present qualitative, rather than quantitative, results for the full operation of the MOUR devices. Firstly, we did not have access to good quality positioning equipment, which would have allowed the PZT transducer to be held in place with greater stability than we were able to achieve by hand. This is particularly important for our experiments since, because the sensitive area of our prototype MOUR devices is so large, there is a small angle of acceptance for ultrasound [3]. This makes it very difficult to align the PZT transducer to the solid angle of acceptance, and also difficult to consistently repeat measurements. More useful MOUR implementations would have smaller sensitive areas by using higher frequency carriers and therefore smaller resonator footprints. There were two reasons why we were not able to demonstrate such devices in the course of our experiments: firstly, we did not have access

to microwave sources above 3 GHz. Secondly, the smallest features of our resonator design (about 20 μm) were already near the limits of achievable resolution for standard PCB wet etching processes available to us.

A further problem resulted from the use of a gel-wax spacer. Conventionally, the performance of ultrasound receivers is measured in a tank of deionised water, which has very low acoustic attenuation and well-characterised acoustic properties [4–7].[2] However, since this experiment required microwave equipment, it was not feasible to relocate the experiment to a lab which had such a water tank, nor install a tank in the microwave lab. Although the microwave components can in principle be integrated onto a single board, designing such a board is a significant undertaking and would have been difficult to complete within a reasonable time frame.

Yet another problem was that we were not able to precisely control the phase of the reference arm for our homodyne detection system. Small mismatches in phase between the reference and signal arms create large spurious signals which add significant noise in the active components. Although we had access to an analogue phase shifter, it was challenging during the experiment to simultaneously optimise the tune point of the microwave carrier source and the phase offset of the reference arm. Since the resonator introduces a significant phase shift itself, the correct phase offset changes significantly depending on the tune point. There were also significant power imbalances between the reference and signal arms, as the signal arm is significantly attenuated by the resonator. Again, the precise attenuation depends strongly on the tune point. Not having access to a digital variable attenuator, we

[2] Actually, it's unlikely that acoustic attenuation contributed much, if anything, to the small signals we were able to detect. On the other hand, having to hold the transducer so close to the device meant that the MOUR receiver was in the transducer's near-field.

were not able to cancel the spurious carrier signal. Lastly, it is possible that reflected signals from the resonator due to the high S_{11} near the tune point were coupling back into the reference arm due to insufficient isolation at the splitter. This may explain why when tuning the homodyne system to the resonance we saw a large increase in the noise on the oscilloscope. All of these factors could be addressed by designing an integrated system with fixed path lengths between the components, although this would be a significant undertaking.

Finally, we would like to have been able to carefully control the deposition of the superstrate layer, and therefore have a uniform layer of known thickness which we could have quantitatively characterised. Although this was possible with Paralyne-C, the boards we were using were not acoustically compatible with Paralyne-C due to their relatively low acoustic impedance. By way of contrast, previous experiments using Paralyne-C as the deformable layer, as used in optical hydrophone experiments [8], rely on a fused silica backing with a very high acoustic impedance (over 10 MRayl).

5.2 Estimating the Noise-Equivalent Pressure

The noise-equivalent pressure, or NEP, is defined as the minimum detectable ultrasound pressure wave over a certain measurement bandwidth. In this work, we will define it precisely as

$$\mathrm{NEP}_{\text{pk-pk}}(\Delta f) = \frac{\sigma_{\text{pk-pk}}(\Delta f)}{\sqrt{G M_{\max}} Z_0}, \tag{5.3}$$

where $M_{\max}$ is the maximum device sensitivity as defined by (4.16), $\sigma_{\text{pk-pk}}(\Delta f)$ is the measured peak-to-peak standard deviation voltage noise of the system, G is the amplifier power gain, and Z_0 is the input impedance of the amplifier (which for practical purposes is typically 50 Ω).

Using our experimental setup, we are able to directly measure the following quantities: firstly, we can measure $\sigma_{\text{pk-pk}}$ over the bandwidth of 200 MHz using the oscilloscope by setting up the MOUR experiment as described above and measuring the peak-to-peak voltage standard deviation displayed on the oscilloscope. With the amplifier gain set to 60 dB, $\sigma_{\text{pk-pk}}(200\,\text{MHz}) = 390\,\text{mV}$. Secondly, from our polyimide tape experiments, we measured $\mathrm{d}f_{\text{res}}/\mathrm{d}d$ (where d is the superstrate thickness and f_{res} is the device resonance) to be $-0.57\,\text{MHz}/\mu\text{m}$. By tuning the microwave source to the quadrature of the device resonance and varying it slightly, we were able to measure $\mathrm{d}v_{\text{out}}/\mathrm{d}f_{\text{tune}}$ as $0.06\,\text{mV}/\text{MHz}$.

Since we did not have the necessary equipment to measure the acoustic characteristics of the MOUR device, to determine $\mathrm{d}d/\mathrm{d}p$ we instead used models developed in §4.2.2. For an acoustically ideal sensor where the ultrasound frequency is well below the first acoustic minimum, the superstrate layer is perfectly matched to the medium, and the backing is perfectly rigid and reflective, we can see from (4.41) that

$$\frac{\mathrm{d}d}{\mathrm{d}p} = \frac{2d_0}{E}, \tag{5.4}$$

where E is the Young's modulus of the superstrate layer and d_0 is its thickness.

The value of $\sqrt{GM_{\text{max}}}Z_0$ from (5.3) is therefore given by

$$\begin{aligned}\sqrt{GM_{\max}}Z_0 &= \frac{\mathrm{d}f_{\mathrm{res}}}{\mathrm{d}d}\frac{\mathrm{d}v_{\mathrm{out}}}{\mathrm{d}f_{\mathrm{tune}}}\frac{\mathrm{d}d}{\mathrm{d}p} \\ &= 0.57\,\mathrm{MHz}/\mu\mathrm{m} \times 0.6\,\mathrm{mV}/\mathrm{MHz} \times \frac{2d_0}{E} \\ &= 0.57\,\mathrm{MHz}/\mu\mathrm{m} \times 0.6\,\mathrm{mV}/\mathrm{MHz} \times \frac{2 \times 0.1\,\mathrm{mm}}{0.5\,\mathrm{MPa}} \\ &= 136.8\,\mathrm{mV}/\mathrm{MPa}\end{aligned} \tag{5.5}$$

where E has been given as the Young's modulus for a typical elastomer (ie, PDMS) and $d_0 = 0.1\,\mathrm{mm}$. Therefore,

$$\begin{aligned}\mathrm{NEP}_{\text{pk-pk}}(200\,\mathrm{MHz}) &= 390\,\mathrm{mV}/(136.8\,\mathrm{mV}/\mathrm{MPa}) \\ &= 2.85\,\mathrm{MPa}.\end{aligned} \tag{5.6}$$

The NEP performance for this device is poor compared to PVDF and optical hydrophone devices [7, 9], but agrees with the results shown in Figure 5.11, where we are just barely able to recover a few MPa of signal. For the reasons mentioned above, the calculation in (5.5) overestimates $\mathrm{d}d/\mathrm{d}p$ because of the imperfect acoustic properties of our device—the incident sound waves are not perfectly reflected off the backing—but this is a smaller contributing factor than the noise of the receiver system.

A well-designed receiver system, possibly implementing a balanced amplifier to fully cancel the carrier and reduce the resulting shot-noise, would result in the largest reduction of the NEP. Further improvements could be made by using a ceramic substrate for better acoustic backing, a matching layer deposited on top of the superstrate and better isolation between the reference and signal arms of the receiver system. We also think that a study of ferroelectric-like superstrate materials could lead to the discovery of a highly pressure-sensitive microwave material which would further enhance the sensi-

tivity.

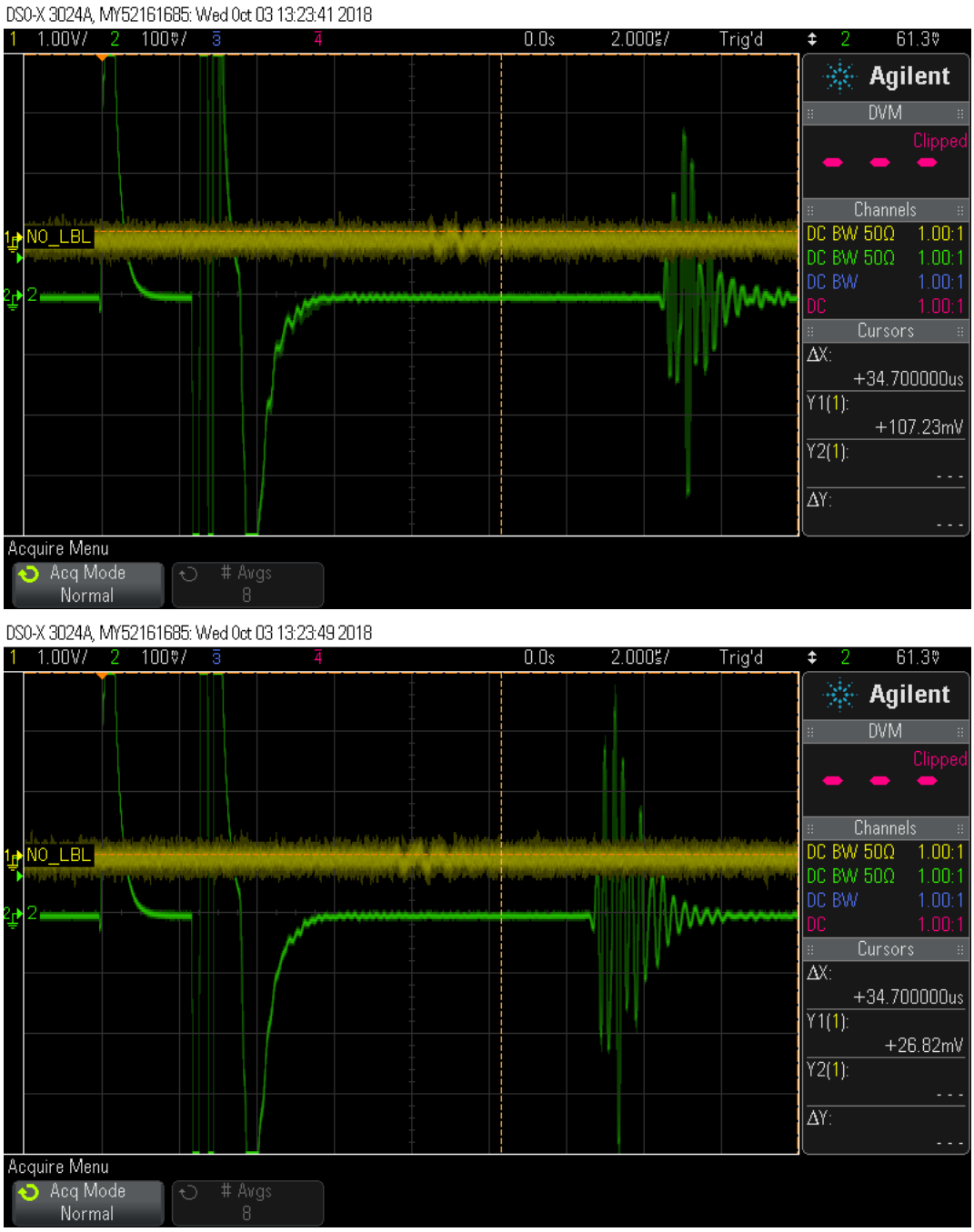

Figure 5.11: Oscilloscope traces showing the PZT transducer (green) and MOUR device (yellow) responses

References

[1] Franck Levassort et al. “Characterisation of Thin Layers of Parylene at High Frequency Using PZT Thick Film Resonators”. In: *Journal of the European Ceramic Society* 25 (Dec. 31, 2005), pp. 2985–2989. doi: 10.1016/j.jeurceramsoc.2005.03.208.

[2] Efthymios Maneas et al. “Gel Wax-Based Tissue-Mimicking Phantoms for Multispectral Photoacoustic Imaging”. In: *Biomedical Optics Express* 9.3 (Mar. 1, 2018), pp. 1151–1163. issn: 2156-7085. doi: 10.1364/BOE.9.001151. url: https://www.osapublishing.org/boe/abstract.cfm?uri=boe-9-3-1151 (visited on 10/04/2018).

[3] B. T. Cox and P. C. Beard. “The Frequency-Dependent Directivity of a Planar Fabry-Perot Polymer Film Ultrasound Sensor”. In: *IEEE Transactions on Ultrasonics, Ferroelectrics, and Frequency Control* 54.2 (Feb. 2007), pp. 394–404. issn: 0885-3010. doi: 10.1109/TUFFC.2007.253.

[4] D. R. Bacon. “Characteristics of a PVDF Membrane Hydrophone for Use in the Range 1-100 MHz”. In: *IEEE Transactions on Sonics and Ultrasonics* 29.1 (Jan. 1982), pp. 18–25. issn: 0018-9537. doi: 10.1109/T-SU.1982.31298.

[5] P. C. Beard et al. “Comparison of a Miniature, Ultrasonic, Optical Fibre Hydrophone with PVDF Hydrophone Technology”. In: *1998 IEEE Ultrasonics Symposium. Proceedings (Cat. No. 98CH36102)*. 1998 IEEE Ultrasonics Symposium. Proceedings (Cat. No. 98CH36102). Vol. 2. 1998, 1881–1884 vol.2. doi: 10.1109/ULTSYM.1998.765319.

[6] J. A. Guggenheim, E. Z. Zhang, and P. C. Beard. “A Method for Measuring the Directional Response of Ultrasound Receivers in the Range 0.3–80 MHz Using a Laser-Generated Ultrasound Source”. In: *IEEE Transactions on Ultrasonics, Ferroelectrics, and Frequency Control* 64.12 (Dec. 2017), pp. 1857–1863. issn: 0885-3010. doi: 10.1109/TUFFC.2017.2758173.

[7] James A. Guggenheim et al. “Ultrasensitive Plano-Concave Optical Microresonators for Ultrasound Sensing”. In: *Nature Photonics* 11.11 (Oct. 31, 2017), p. 714. issn: 1749-4893. doi: 10.1038/s41566-017-0027-x. url: https://www.nature.com/articles/s41566-017-0027-x (visited on 11/03/2017).

[8] P. C. Beard and T. N. Mills. “Extrinsic Optical-Fiber Ultrasound Sensor Using a Thin Polymer Film as a Low-Finesse Fabry–Perot Interferometer”. In: *Applied Optics* 35.4 (Feb. 1, 1996), pp. 663–675. issn: 2155-3165. doi: 10.1364/AO.35.000663. url: https://www.osapublishing.org/abstract.cfm?uri=ao-35-4-663 (visited on 12/15/2017).

[9] P. C. Beard et al. “Comparison of a Miniature, Ultrasonic, Optical Fibre Hydrophone with PVDF Hydrophone Technology”. In: *1998 IEEE Ultrasonics Symposium. Proceedings (Cat. No. 98CH36102)*. 1998 IEEE Ultrasonics Symposium. Proceedings (Cat. No. 98CH36102). Vol. 2. Oct. 1998, 1881–1884 vol.2. doi: 10.1109/ULTSYM.1998.765319.

Chapter 6

Conclusion

The work in this thesis was inspired by the use of optical interferometry to detect ultrasound. Although optical detection has many advantages, including wideband responsivity, MRI compatibility and high sensitivity, it is difficult to multiplex without resorting to integrated optics. The problem with integrated optics is the same as the problem with building CMOS-compatable piezoelectric arrays: it's hard to simultaneously satisfy foundry and acoustic material requirements. This is why the predominant technology for the next-generation of high channel count integrated ultrasound transducers is MEMS, which allows cavities to be incorporated into CMOS processing. Two versions of this idea, PMUT and CMUT, were discussed in the Introduction.

Rather than give up on interferometry altogether, the purpose of this thesis was to examine whether it might be possible to use the same techniques with electronics rather than optics. At first sight this looks like a bad idea: what we usually consider the microwave frequency band is generally under 5 GHz, meaning a free-space wavelength of 6 cm. Ultrasound, on the other hand, deals with wavelengths of the order of microns. Although EM waves at ultrasound frequencies can also penetrate tissue, their long wavelength makes imaging impractical unless combined with a second gradient field—this was addressed in our section on zeugmatographic imaging where we looked at the fun-

damental limits of capturing spatial information encoded in one type of field with another type.

Two recent developments make interferometric sensing of ultrasound using purely electronic devices feasible: firstly, the availability of milimetre-wave sources, and secondly, the availability of high permittivity ceramics. Both of these combine to make it possible to create resonators with dimensions below the Nyquist wavelength of commonly used ultrasound frequencies.

MOURs are appealing because they can be constructed very simply. In our designs, the mechanical field interacts with the evanescent part of the EM field. This means that the EM part of the design can be on the plane orthogonal to the direction ultrasound propagation. Being able to build these devices 'bottom-up' and only have to apply the acoustically active part as a final fabrication step makes MOURs unique among all types of transducer, except perhaps optical hydrophones where the light beam travels towards the imaging plane.

Sensitivity issues aside, MOURs have a couple of fundamental drawbacks. One is that they can only receive and not transmit ultrasound. However, we believe that there are situations in which duplexed imaging systems, which transmit and receive using the same device, may not be optimal or necessary. These situations include passive acoustic mapping (PAM) of non-linear ultrasound events, photoacoustics, elastography, and fast plane-wave imaging. Furthermore, in some pulse-echo imaging scenarios, we can no longer treat the imaging domain as being part of a linear system: the optimal receiver is not necessarily the complex conjugate of the transfer function of the transmitter when reflected waves have a different spectral density to the incident waves. We see MOURs as having the potential to provide a useful bridge between optical hydrophones, which excel in highly non-linear imaging contexts, and multiplexed PZT transducer arrays, which offer

many independently addressable channels for versatile imaging. When studying the literature, we found that much of the discussion around beamforming made the assumption of duplexing. To that end, we invented our own formalism for beamforming which has a pleasing symmetry between purely passive systems which focus 'holographically', and duplexed systems which focus during transmission.

With regards to sensitivity, we carefully studied the electromagnetic and acoustic factors which affect performance. We examined a basic LC resonator model to understand the effect of resistive losses in the Q of the resonator, and looked at how that ultimately affected sensitivity. We also extended the model for the behaviour of the superstrate layer in the acoustic field beyond previous work done for optical ultrasound sensors: our model can account for the contributions of an infinite number of reflections and predict the performance over a variety of acoustic impedance contrasts. We also looked at the unique noise properties of MOURs, and gave some theoretical justification that shot noise was the limiting factor preventing us from obtaining clean traces of ultrasound pulses.

MOURs turned out to have some features which we did not consider at the start of this work. One feature is the possibility of multiplexing many elements onto a single electrical connection using frequency-division multiplexing (FDM). This could be useful in challenging environments such as interventional ultrasound, where it is necessary to keep electrical connections to a minimum. Another feature is the robustness MOURs have to in-band interference from either other ultrasound transmitting devices or EM noise in the ultrasound frequency range. The reason for this robustness is that, similarly to optical ultrasound sensors, the ultrasound signal is not directly encoded into a baseband electronic representation. To make this system truly robust, the modulated microwave signal could be heterodyned into an

intermediate signal and directly fed into an ADC.

6.1 Future Work

In the present work, we were not able to fully characterise the performance of our proof-of-concept MOUR device for several reasons. Firstly, we lacked the equipment to deposit thin superstrate layers of appropriate materials in a controllable way. Secondly, we lacked the proper microwave equipment, such as digital phase shifters, digital attenuators, or alternatively a second phase-locked microwave source, to properly suppress the microwave carrier which created the majority of the noise in our system, thereby limiting the measurable SNR. Thirdly, the logistics of incorporating microwave equipment into industry-standard ultrasound device characterisation equipment (ultrasound systems are almost always characterised whilst submerged in deionised water) proved insurmountable given the time and cost constraints of the project. The first step in continuing the research would be to address these three issues and measure the SNR, and therefore the noise-equivalent pressure (NEP), of a MOUR device under ideal conditions.

Once these measurements have been made, and provided they demonstrate an at least 60 dB improvement on the current sensitivity, there would be three avenues for future work: product development, material research, and new sensors. Additionally, the acoustically non-resonant nature of MOURs, and the fact that they would have to be incorporated into a non-duplexed platform for imaging applications, prompted us to consider ways of combining digital signal processing (DSP) and non-resonant acoustic devices to emulate a variety of different conventional pulse-echo imaging systems. This technique would have to be combined with significant improvements in the performance of MOUR in order to be useful.

6.1.1 Product Development

To develop the concept of MOUR into a product which can be integrated into ultrasound imaging probes and other devices, we need to implement the system as either a PCB or an integrated circuit (IC). Through conversations with industry, the author has developed a tentative design for a 64-channel ultrasound receiver system which can be made sensitive to an almost arbitrary range of ultrasound frequencies using off-the-shelf components and standard PCB pick-and-place assembly. The bill of materials (BOM) for this device was under $200, competitive with conventional PZT ultrasound systems. However, to fully take advantage of this new platform, we would want to develop a mixed-signal integrated circuit. Much of the difficulty in designing and manufacturing such ICs has already been addressed by the development of IP blocks for generating and processing GHz analogue signals, primarily for the 5G and automotive radar industries. In a future project, we would look to leverage these IP blocks and construct the systems discussed in the previous chapters on a single IC.

6.1.2 Material Research

In the process of building analytical models to predict the performance of MOUR, we noticed a lack of published material data regarding the microwave characteristics of common materials, such as polyimide and PDMS, and a lack of acoustic characterisation data for materials common in consumer electronics, such as circuit board substrates. This made it impossible to verify our models. For instance, in the simple experiment where we measured the phase shift due to thin strips of polyimide tape on top of a waveguide, we could not verify these results against our theoretical prediction, since we were unable to find any data on the microwave permittivity of polyimide.

A further question was whether there might be an effect similar

to the strain-optic effect in the microwave frequency band for certain materials. It seems reasonable to assume that there might be, given the existence of the piezoelectric effect, which relates strain to DC EM fields, and the strain-optic effect, which relates strain to changes in optical refractive index. Another area of interest is the interaction between microwave polarisation and material anisotropy: the evanescent EM field of our devices is polarised, as can be seen from our FDTD simulations, and there may be ways to exploit this in the study of materials.

6.1.3 Future Sensors

The ideas in this thesis are broadly applicable to other types of sensor. Although resonant EM sensing is not new, there are ideas in this work, such as spatially mapping different parts of the sensor onto different microwave frequencies, or using off-the-shelf components to generate and receive the signals, which could benefit a wider range of sensors. Development of new composite materials for the superstrate layer—sensitive to chemical changes, particular molecules, or other fields—could help realise these ideas.

6.1.4 Software Defined Transducers: a Signal Processing Concept for MOUR

Conventional piezoelectric transducer designs must trade-off between cost, sensitivity and bandwidth [1]. How those factors are balanced generally depends on the given application. For instance, in calibrating ultrasound sources, polyvinylidene difluoride (PVDF) transducers are used since they offer a flat frequency response at relatively low cost. However, for B-mode imaging applications, the sensitivity requirements generally rule out PVDF in favour of hard ceramic or single-crystal transducers. These have higher sensitivity, but also high acoustic impedance compared to the imaging medium, meaning

they optimally accept signals in a narrow band around their resonant frequency. For pulse-echo systems, this introduces two problems: (1) Due to the non-linear nature of acoustic attenuation (higher frequencies are more attenuated) and scattering from moving targets (due to the Doppler effect), the received echoes are generally shifted in frequency, away from the transducer resonance, reducing the detected signal. (2) Narrow-band pulses introduce an uncertainty in measuring time-of-arrival, reducing axial resolution.

To mitigate these problems, modern transducers incorporate acoustic matching layers and damped backings to increase acoustic coupling to the medium and reduce ringing. Widening the bandwidth increases the overall pulse-echo insertion loss of the transducers, so the appropriate trade-off must be decided between sensitivity, bandwidth and cost. These decisions are made during the transducer design process according to the application requirements, meaning they are fixed at the time of manufacture [2]. However, if such trade-offs could be made in the software, rather than hardware, layer, end-users could be given access to a suite of 'virtual' transducers operating with various frequencies, bandwidths and sensitivities. We term this approach 'software-defined transducer' (SDT).

Due to the wide variety of materials which can be used to construct MOUR devices (any combination of dielectrics will work), MOURs can be designed to be impedance matched to the imaging medium over a wide bandwidth. In this context, SDT-MOURs can be combined with single plane-wave emitters to perform high-speed volumetric imaging, as well as enabling wideband acoustic imaging—important for non-linear techniques such as photoacoustics [3], elastography [4], and focused ultrasound therapy [5]. Digital filtering and software-driven imaging are not new to ultrasound: digital filtering has been used to create matched filters for coded transmission systems—a

technique to increase the time-bandwidth product of ultrasound pulses and hence increase the signal-to-noise ratio (SNR) for high-resolution systems. But unlike in SDTs, those filters are used to compensate for the bandpass characteristics of the transducer, which is operated near resonance [6, 7]. To create an SDT, we would instead use a transducer with a flat frequency response, such as MOURs, and re-implement the useful filtering transducers usually provide in software. Another similar concept, software-defined ultrasound (the use of digital beamforming and, in particular, moving digital signal processing (DSP) hardware into the probe itself and sending images to the monitor digitally) is widely known [8]. We take this idea one step further, by proposing to subject the raw digitised radio frequency (RF) signal from each transducer to sophisticated DSP *before* the beamforming stage.

Other workers in the field have looked at using DSP for multiresolution analysis of ultrasound data [9], part of a broader trend of extracting clinically relevant information from raw RF ultrasound data. Traditionally, ultrasound images are formed using only the baseband (I/Q) representation of the signal, with the baseband defined as the resonant frequency of the transducer. As we have already mentioned, even the most basic treatments of ultrasound imaging recognise the presence of significant acoustic 'linewidth broadening' due to nonlinear interactions [10], meaning the baseband representation must necessarily omit some information which is present in the fully-sampled RF representation. This has been the impetus behind a growing interest in analysing raw ultrasound RF data, either by frequency decomposition [9] or more advanced machine learning techniques. In this section, we demonstrate how this new approach to ultrasound signal processing can be coupled with hardware design which emphasises bandwidth over sensitivity, and demonstrate that this does not necessarily result in a fundamental trade-off in imaging quality.

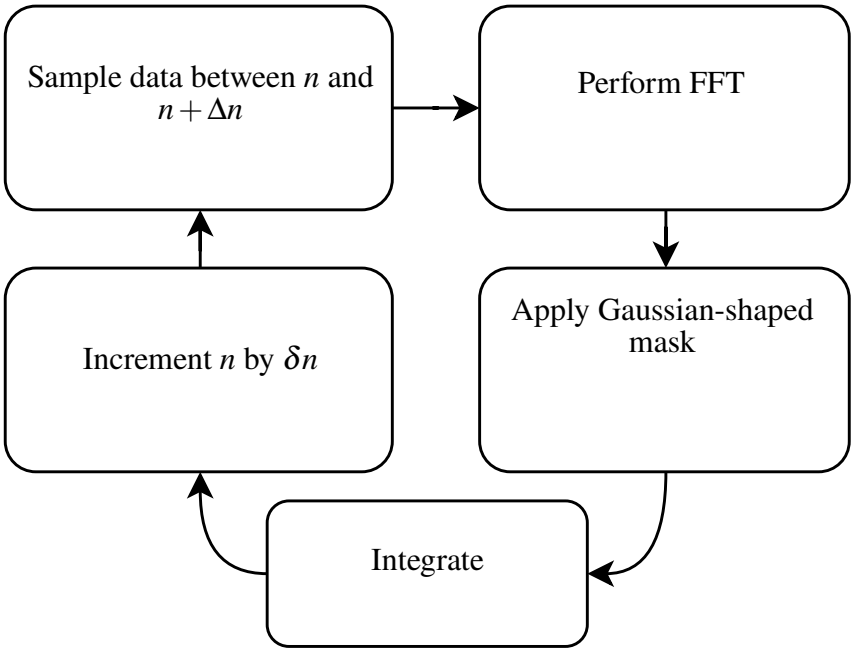

Figure 6.1: Flowchart of procedure to find peaks in noise. Δn and δn can be tweaked to optimise the pulse recovery.

6.1.4.1 Using DSP to Emulate Tunable Mechanical Resonance in Ultrasound Receivers

In this section, we illustrate how combining DSP with broadband MOURs exhibiting low sensitivity can recover the pulse-echo performance of less versatile but highly sensitive transducers, such as the air-backed PZT device shown in Figure 2.4. To test our ideas, we generated a train of Gaussian pulses on a 1 MHz carrier frequency with unit amplitude and randomised arrival times with a repetition rate of approximately 50 kHz. We then added Gaussian white noise to the digital signal over a sampling bandwidth of 200 MHz (see inset of plot A, Figure 6.2). A rolling fast Fourier transform (FFT) was performed over the pulse trains to generate a spectrogram of the simulated A-scan (procedure shown in Figure 6.1). From this, a representation of the estimated arrival times and amplitudes could be calculated, shown in plot A of Figure 6.2.

To evaluate the performance of this technique for various pulse

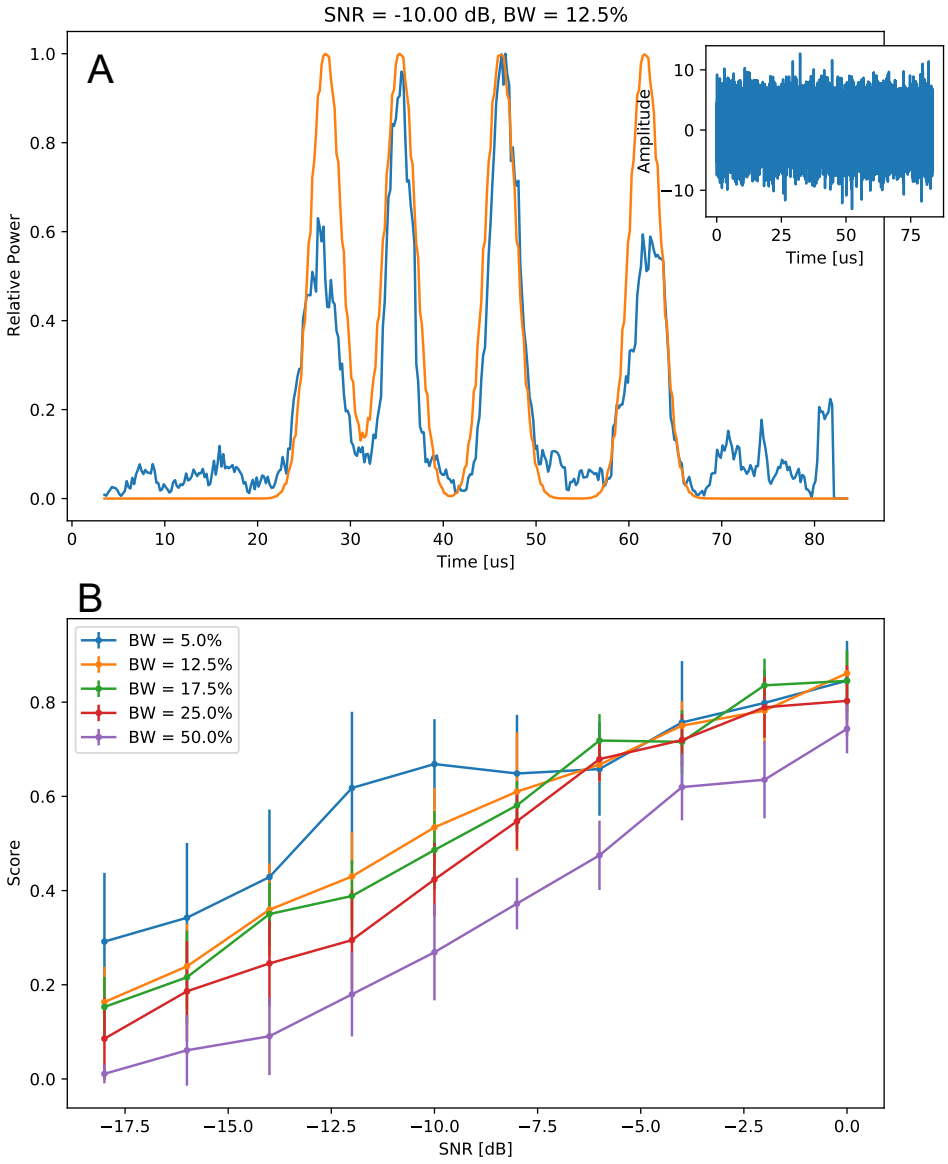

Figure 6.2: *Top:* Plot showing estimated positions and amplitudes calculated from a noisy train of pulses (inset) with SNR $= -10$ dB and a bandwidth (BW) of 12.5%. Actual pulse positions shown in orange. *Bottom:* Plot showing calculated scores for different bandwidth pulses at various SNRs.

bandwidths, we devised a scoring function calculated as follows: first, the pulse estimate data (plot A, Figure 6.2) is clipped and normalised such that any signals below 2σ (where σ is the standard deviation of the pulse estimate data) are zeroed and all detected pulses have heights on the interval $(0, 1]$. Any remaining points above zero should now represent an actual detected pulse with a maximum false positive rate

of 2.3% (assuming the noise is Gaussian). The score is given by:

$$\text{score} = \int \text{PED}_{\text{noisy}}(t) \times \text{PED}_{\text{clean}}(t)\mathrm{d}t, \tag{6.1}$$

where $\text{PED}_{\text{noisy}}$ is the clipped and normalised pulse estimate data described above, $\text{PED}_{\text{clean}}$ is the pulse estimate data calculated from the ground-truth (ie, the pulse train without any added noise), and t is time.

Plot B in Figure 6.2 shows the scores calculated from random A-scans of Gaussian pulses generated for various bandwidths. Each point represents a score averaged from a set of five A-scans, each comprising ten pulses. The hockey-stick shape of the curve illustrates that, using the procedure described in Figure 6.1, it is possible to extract signals which lie between 5 and 10 dB below the noise floor, in effect lowering the minimum detectable signal. Larger noise floor reductions are possible for narrowband pulses, and smaller reductions are possible for broadband pulses. Referring to Figure 2.4, this means that the matched PZT transducer can attain the sensitivity of the air-backed PZT for sufficiently narrowband pulses, despite being nominally several dB less sensitive, even at its resonant frequency. An imaging system comprising the matched PZT transducer with a controllable transmitted pulse bandwidth (which could be implemented by driving the transducer with an arbitrary waveform generator) would allow image contrast (sensitivity) to be dynamically traded off with axial resolution (bandwidth). Similarly, in this example the hard-backed PVDF transducer can attain the sensitivity of the matched PZT transducer, at the expense of some uncertainty in received pulse amplitude, for 12.5 % bandwidth pulses. Furthermore, by tuning the digital bandpass filter, the PVDF transducer can acquire a tunable 'virtual resonance', making it adaptable to various applications—for instance, allowing real-time

switching between low frequencies for deep, low-resolution imaging and high frequencies for shallow, high-resolution imaging. More sophisticated techniques, such as discrete wavelet transforms (DWT) [11], could enhance this further, and even allow simultaneous emulation of different transducers [9].

6.1.4.2 Discussion and Conclusion

Transducer design has traditionally required careful analysis of the imaging application being developed for to make appropriate tradeoffs between cost, bandwidth and sensitivity. We hope to have shown in this chapter that digital signal processing, combined with high analogue-to-digital converter (ADC) sampling rates, can allow broadband transducers such as MOURs to emulate sensitive, narrow-band transducers. This work draws its inspiration from software-defined radio, which uses low-gain broadband antennas and advanced DSP to create low-cost, versatile systems [12]. Just as in communications there is a tradeoff between bandwidth (which increases the bitrate) and SNR (which reduces the bit error rate), in pulse-echo ultrasound there is a tradeoff between axial resolution (bandwidth) and SNR (transducer gain) [10].

Implementation of the procedure outlined in the preceding section will require each receive channel to perform its own real-time DSP, which will likely need to be implemented on FPGAs due to the high latency associated with microprocessors. This relies on digitisation pipelines moving further up the signal processing chain, a trend which is already well underway in many systems [8]. Full SDT systems will need an equal number of digital channels and elements, though this is not necessary for partial implementations.

Although the noise floor reduction in our numerical experiments is modest, the use of non-Gaussian pulses such as chirps and Golay

codes—which have higher time-bandwidth products—could yield improvements [10]. Nonetheless, we think that the groundwork laid by software-defined ultrasound means that SDT concepts could be incorporated into new imaging systems with relative ease. In particular, building images by combining acquisitions obtained by switching transducers between operating in narrowband (high contrast) and broadband (high resolution) modes could result in image quality improvements without needing new hardware.

Finally, alternative transducer technologies, such as CMOS-integrated PVDF [13], capacitive and piezo micro-machined ultrasound transducers (CMUTs/PMUTs) [14] and MOURs [15], all of which can be made using lithographic techniques, promise low-cost high-volume transducer production. This will likely come at the expense of customisability: economies of scale will push designers of low-cost systems to choose from a relatively small a pool of transducer designs. SDT concepts can help alleviate this, by allowing for greater versatility on top of a fixed hardware layer.

***

To summarise, we developed a new type of ultrasound receiver concept, called MOUR. We examined in some detail the working principle of this device, as well as how it is affected by various design choices and its fundamental limitations. We noted some interesting unique features, such as their simplicity of construction, inherent wideband sensitivity, and low susceptibility to in-band interference. We developed a proof-of-concept experiment which demonstrated that MOURs work at least in principle. Future work could establish its real-world performance compared to existing devices such as PZT transducers and optical hydrophones.

References

[1] J. W. Hunt, M. Arditi, and F. S. Foster. "Ultrasound Transducers for Pulse-Echo Medical Imaging". In: *IEEE Transactions on Biomedical Engineering* BME-30.8 (Aug. 1983), pp. 453–481. issn: 0018-9294. doi: 10.1109/TBME.1983.325150.

[2] C. S. Desilets, J. D. Fraser, and G. S. Kino. "The Design of Efficient Broad-Band Piezoelectric Transducers". In: *IEEE Transactions on Sonics and Ultrasonics* 25.3 (May 1978), pp. 115–125. issn: 0018-9537. doi: 10.1109/T-SU.1978.31001.

[3] Paul Beard. "Biomedical Photoacoustic Imaging". In: *Interface Focus* 1.4 (Aug. 6, 2011), pp. 602–631. issn: 2042-8898, 2042-8901. doi: 10.1098/rsfs.2011.0028. pmid: 22866233. url: http://rsfs.royalsocietypublishing.org/content/1/4/602 (visited on 12/16/2015).

[4] Rosa M.S. Sigrist et al. "Ultrasound Elastography: Review of Techniques and Clinical Applications". In: *Theranostics* 7.5 (Mar. 7, 2017), pp. 1303–1329. issn: 1838-7640. doi: 10.7150/thno.18650. pmid: 28435467. url: https://www.ncbi.nlm.nih.gov/pmc/articles/PMC5399595/ (visited on 07/05/2019).

[5] Carl R. Jensen et al. "Spatiotemporal Monitoring of High-Intensity Focused Ultrasound Therapy with Passive Acoustic Mapping". In: *Radiology* 262.1 (Jan. 1, 2012), pp. 252–261. issn: 0033-8419. doi: 10.1148/radiol.11110670. url: https://pubs.rsna.org/doi/full/10.1148/radiol.11110670 (visited on 07/05/2019).

[6] R. Y. Chiao and Xiaohui Hao. "Coded Excitation for Diagnostic Ultrasound: A System Developer's Perspective". In: *IEEE Transactions on Ultrasonics, Ferroelectrics, and Frequency Control* 52.2 (Feb. 2005), pp. 160–170. issn: 0885-3010. doi: 10.1109/TUFFC.2005.1406543.

[7] T. X. Misaridis and J. A. Jensen. "An Effective Coded Excitation Scheme Based on a Predistorted FM Signal and an Optimized Digital Filter". In: *1999 IEEE Ultrasonics Symposium. Proceedings. International Symposium (Cat. No.99CH37027)*. 1999 IEEE Ultrasonics Symposium. Proceedings. International Symposium (Cat. No.99CH37027). Vol. 2. Oct. 1999, 1589–1593 vol.2. doi: 10.1109/ULTSYM.1999.849299.

[8] P. A. Hager, P. ArminJud, and L. Bertini. “A Low-Cost Software-Defined Ultrasound System Capable of High-Speed Ultrasound Bubble Tracking”. In: *2018 IEEE International Ultrasonics Symposium (IUS)*. 2018 IEEE International Ultrasonics Symposium (IUS). Oct. 2018, pp. 1–4. doi: 10.1109/ULTSYM.2018.8579823.

[9] G. Cincotti, G. Loi, and M. Pappalardo. “Frequency Decomposition and Compounding of Ultrasound Medical Images with Wavelet Packets”. In: *IEEE Transactions on Medical Imaging* 20.8 (Aug. 2001), pp. 764–771. issn: 1558-254X. doi: 10.1109/42.938244.

[10] Richard S. C. Cobbold. *Foundations of Biomedical Ultrasound*. Oxford University Press, Sept. 7, 2006. 844 pp. isbn: 978-0-19-977512-5. Google Books: Hwb5D60vb5IC.

[11] A. Abbate et al. “Application of Wavelet Transform Signal Processor to Ultrasound”. In: *1994 Proceedings of IEEE Ultrasonics Symposium*. 1994 Proceedings of IEEE Ultrasonics Symposium. Vol. 2. Oct. 1994, 1147–1152 vol.2. doi: 10.1109/ULTSYM.1994.401791.

[12] Asad A. Abidi. “The Path to the Software-Defined Radio Receiver”. In: *IEEE Journal of Solid-State Circuits* 42.5 (May 2007), pp. 954–966. issn: 0018-9200. doi: 10.1109/JSSC.2007.894307. url: http://ieeexplore.ieee.org/document/4160058/ (visited on 08/07/2019).

[13] John K. Schneider and Jack C. Kitchens. “Hydrophone Array Module”. U.S. pat. 7436736B2. Ultra-Scan Corp. Oct. 14, 2008. url: https://patents.google.com/patent/US7436736B2/en?q=tft&assignee=Ultra-Scan+Corporation&oq=assignee:(Ultra-Scan+Corporation)+tft (visited on 07/10/2019).

[14] Kevin Brenner et al. “Advances in Capacitive Micromachined Ultrasonic Transducers”. In: *Micromachines* 10.2 (Feb. 2019), p. 152. doi: 10.3390/mi10020152. url: https://www.mdpi.com/2072-666X/10/2/152 (visited on 03/12/2019).

[15] T. S. Robbins et al. “Microwave Oscillator Ultrasound Receivers”. In: *2018 IEEE International Ultrasonics Symposium (IUS)*. 2018 IEEE International Ultrasonics Symposium (IUS). Oct. 2018, pp. 1–4. doi: 10.1109/ULTSYM.2018.8580205.